SELF-ASSEMBLY OF COBALT, COPPER AND MOLYBDENUM BASED HYBRID SOLIDS: TUNING METAL-LIGAND INTERACTIONS TOWARDS PROPERTIES

Submitted to the University of Calicut

in partial fulfillment of the requirements

for the Degree of

Doctor of Philosophy in

Chemistry

By

MEMSY C K

Under the guidance of

Dr. JENCY THOMAS

RESEARCH AND POST GRADUATE DEPARTMENT OF CHEMISTRY

ST. THOMAS COLLEGE (AUTONOMOUS)

THRISSUR, KERALA-680001

MARCH 2023

Estd. 1889

Research & PG Department of Chemistry
ST.THOMAS COLLEGE
(Autonomous)
THRISSUR - 680 001, KERALA, INDIA
Affiliated to the University of Calicut & NAAC Accredited with CGPA 3.70/4 at 'A++' Grade-4th Cycle
Web:- http://stthomas.ac.in Email:- stcthrissur@gmail.comPhone:- +91 487 2420435 Fax:- +91 487 2421510

24-03-2023

CERTIFICATE

This is to certify that the thesis entitled "**Self-Assembly of Cobalt, Copper and Molybdenum Based Hybrid Solids: Tuning Metal-Ligand Interactions Towards Properties**" is an authentic record of research work carried out by **Memsy C K** under my supervision in partial fulfillment of the requirements for the degree of Doctor of Philosophy, in Chemistry of University of Calicut and further that no part thereof has been presented before for any other degree.

Dr. Jency Thomas
(Research Supervisor)

DECLARATION

I hereby declare that the thesis entitled “**Self-Assembly of Cobalt, Copper and Molybdenum Based Hybrid Solids: Tuning Metal-Ligand Interactions Towards Properties**”, submitted to the University of Calicut in partial fulfillment of the requirements for the award of the Degree of Doctor of Philosophy in Chemistry is a bonafide research work done by me under the supervision and guidance of Dr. Jency Thomas, Assistant Professor, Research & PG Department of Chemistry, St. Thomas College (Autonomous), Thrissur, Kerala.

I further declare that this thesis has not previously formed the basis of any degree, diploma or any other similar title.

Memsy C K

ACKNOWLEDGEMENT

“*When you want something, all the universe conspires in helping you to achieve it.*”

– Paulo Coelho

Praises and thanks to the Almighty God, the ultimate source of all knowledge and wisdom, for guiding me through this research journey and for granting me the strength and ability to complete it.

This work would not have been possible without the support, guidance, and encouragement of many individuals and organizations, and I am deeply grateful for their contributions.

I would like to express my heartfelt gratitude to my research guide, Dr. Jency Thomas, Assistant Professor, Research & PG Department of Chemistry, St.Thomas College (Autonomous), Thrissur, for her guidance, support and mentorship throughout my research endeavor. Her expertise, creative thinking, insightful feedback, constructive criticism and patience have been critical to the successful completion of this work. I could not have accomplished this without her help and guidance, and I am forever grateful for her contributions to my research work.

I would like to thank our principal Rev. Dr. Martin Kolambrath, Head of the Department, Dr.Paulson Mathew and all the former HOD’s who were instrumental in providing the working atmosphere and all basic instrumentation facilities for pursuing Ph.D. My heartfelt thanks to all other faculty members of the department. I also extend my sincere thanks to all the non teaching staffs of chemistry department.

With great appreciation, I would like to acknowledge the support and help extended by the Research Scholars of the Department. Many thanks and gratitude to my research group members, Dr. Sr. Jisha Joseph and Ms. Raji C R, for always being a helping hand in times of need.

I would like to extend my heartfelt gratitude to my alma mater, Mercy College, Palakkad for the support provided to me in pursuing my research goals. I greatly acknowledge Dr.

Sr. Gisala George, Principal, Mercy College, Palakkad, for her unwavering support and encouragement to accomplish my goal. I would also like to thank all our former Principals and the Management for their immense support. I am especially grateful to my colleagues and friends, for their assistance and encouragement. The knowledge and experience gained from this research will undoubtedly benefit me and contribute to the institution's research and development efforts.

I extend my profound thanks to STIC, Cochin and CSIF, Calicut University, for providing necessary instrumentation facilities. I also thank Mercy College, Palakkad for providing FTIR and UV-visible spectrometer facilities sponsored by DST-FIST and UGC. Special thanks to Dr. Sr. Sarupya, H.O.D, Department of Biotechnology, Mercy College, for helping me with the biological studies.

My warmest thanks to my husband Joseph, for his immense love and support. His willingness to lend a listening ear and words of encouragement when I needed them most has made it possible for me to achieve my goals. I also greatly adore the love and support shown by my in-laws and my dearest sister, Semsy.

Last but not the least, I express my sincere gratitude and love to my parents for their incredible support, prayers, love and understanding. Dear Pappa and Mummy, I cannot thank you enough for looking after my children while I was working on my research. Thank you from the bottom of my heart for always being there for me.

To all those who have supported me in this endeavor, I offer my deepest thanks.

Memsy C K

Dedicated to

My Family

TABLE OF CONTENTS

Chapter I. Introduction & Literature Review

Chapter II. Self-Assembly of Anderson Cluster Based Hybrid Solids: Synthesis, Structure and Application

Chapter III. Crystallization of Cobalt Based Hybrid Solids

Chapter IV. Tetrachlorocuprate(II) hybrid solids templated by aminopyridines

Chapter V. Surfactant templated nanostructured phosphomolybdates

Chapter VI: Synthesis and characterization of phosphomolybdate-polypyrrole composites

LIST OF FIGURES

Chapter IV: Tetrachlorocuprate(II) hybrid solids templated by aminopyridines

Chapter V: Surfactant templated nanostructured phosphomolybdates

LIST OF TABLES

LIST OF SCHEMES

List of Abbreviations

APM	Ammonium phosphomolybdate
APS	Ammonium persulphate
ATR	Attenuated total reflection
CP	Coordination polymers
CTAB	Cetyltrimethylammonium bromide
de	Distance from a point on the surface to the nearest nucleus outside the surface
di	Distance from a point on the surface to the nearest nucleus inside the surface
d_{norm}	Normalized contact distance
DMF	Dimethyl formamide
DMSO	Dimethyl sulfoxide
DTA	Differential Thermal Analysis
E_{dis}	Dispersion energy
E_{ele}	Classical electrostatic energy
E_{pol}	Polarization energy
E_{rep}	Repulsion energy
E.Coli	Escherichia coli
EDAX	Energy dispersive X-ray spectroscopy
EY	Eosin Y
FP	Finger print

FESEM	Field emission scanning electron microscope
FTIR	Fourier Transform Infrared
HS	Hirshfeld surface
LMCT	Ligand to metal charge transfer
LBL	Layer by layer
MB	Methylene blue
MC	Metal complex
MEP	Molecular electrostatic potentials
MG	Malachite green
MO	Methyl orange
ORTEP	Oak ridge thermal ellipsoid plot
PMO	Phosphomolybdates
POM	Polyoxometalates
PXRD	Powder X-ray diffraction
r_i^{vdw}	Van der Waals radii of atoms present inside the 3-D Hirshfeld surface
r_e^{vdw}	Van der Waals radii of atoms present outside the 3-D Hirshfeld surface
SCXRD	Single crystal X-ray diffraction
TGA	Thermogravimetric analysis
TMC	Transition metal complex
UV-Vis	Ultraviolet-visible
UV-DRS	Ultraviolet-Diffuse reflectance spectroscopy
ZOI	Zone of inhibition
2-*ampz*	2-aminopyrazine

2-*ampy*	2-aminopyridine
3- *ampy*	3-aminopyridine
4-*ampy*	4-aminopyridine
ampy	aminopyridine
Ppy	Polypyrrole
pz	Pyrazole
1-D	One dimensional
2-D	Two dimensional
3-D	Three dimensional

ABSTRACT

Self-assembly of organic-inorganic hybrid solids is primarily dictated by metal-ligand interactions. The nature of metal ions and ligands involved in the self-assembly directs the formation of a myriad of hybrid solids ranging from discrete metal complexes to extended three dimensional metal organic frameworks. The present thesis explores the nature of reaction conditions such as temperature, pH, nature of reacting molecular units and effect of solvent to investigate the formation of various hybrid solids. The reaction parameters as stated above affect the nature of molecular units participating in the self-assembly leading to different solids.

This thesis explores the formation of different types of hybrid solids based on cobalt, copper and molybdenum by varying the organic moieties and other reaction conditions, which in turn affect the properties of the hybrid solids.

Chapter I provides a detailed review of various types of hybrid solids reported in literature, their classification and application of these hybrid solids in fields such as magnetism, catalysis, antimicrobial activity and luminescence.

Chapter II primarily discusses the interaction of transition metal ions namely cobalt and chromium with molybdenum precursors in the presence of organic ligands such as pyrazole and 2-aminopyrazine. The interaction of the moieties results in the formation of organically templated Anderson cluster based solids.

Subtle changes in the reaction conditions resulted in the formation of a new pseudopolymorph of cobalt namely $[Co(2\text{-H}\mathit{ampz})_2Cl_4]$ and therefore, the properties of this new pseudopolymorph with the reported one has been discussed in Chapter III. The nature of supramolecular interactions, magnetic moments and antibacterial activities of the two pseudopolymorphs has been extensively studied in Chapter III.

In Chapter III it was observed that the direct reaction of cobalt chloride with the ligand resulted in the formation of discrete complex of cobalt. Therefore, in Chapter IV, instead of cobalt chloride, copper chloride was reacted with isomeric aminopyridines which resulted in isomeric solids. The solids were found to exhibit chromotropism. A detailed investigation of intermolecular interactions has also been carried out using Hirshfeld surface analyses and associated 2-D finger print plots.

The use of long chain amines particularly surfactants has been explored in literature for the synthesis of organically templated hybrid solids. Therefore, in Chapter V, the molybdenum precursors were treated in the presence of cationic surfactants in acidic medium to form organically templated phosphomolybdates. The solids synthesized were found to be highly effective in removal of methylene blue, a cationic dye, from aqueous medium.

Long chain amines when replaced with heterocyclic compound pyrrole in the presence of ammonium persulphate resulted in the formation of composite material based on phosphomolybdates which has been discussed in Chapter VI.

Chapter I

Introduction and Literature Review

Summary

Organic-inorganic hybrid solids form an interesting class of solids owing to their intriguing properties and applications. It is certain that hybrid solids can revolutionize current technological and scientific world. Therefore, in this chapter, a general introduction to organic-inorganic hybrid solids has been provided, along with an overview on different types of hybrid solids based on polyoxometalates and transition metals. In addition, the applications of these solids in diverse fields have also been included. The chapter also provides an insight on the various synthetic methods employed for preparing hybrid solids. Finally, the motivation and objectives of the present research work have been highlighted towards the end of the chapter.

I. Introduction

Man’s quest for survival and his inherent curiosity enkindles many to delve into the mysteries of matter. Right from the Alchemists, it has resulted in continuing human attempts to explore, create and make use of materials that possess unique and novel properties. However, it often takes a lot of endeavours to gain in-depth knowledge and understanding of the hidden characteristics and potentials of such materials.

The field of *Hybrid Solids* is one such area where the scientific community still strive hard to fully understand the chemistry of formation, to create innovative combinations and to explore the possible applications.

I.1 Hybrid solids

Hybrid solids, constituting both organic and inorganic components, represent an interesting class of materials due to its structural versatility and diverse applications [1-3]. According to the International Union of Pure and Applied Chemistry (IUPAC), a hybrid solid is defined as “Material composed of an intimate mixture of “inorganic” components, “organic” components, or both types of components. Note: The components usually interpenetrate on scales of less than 1μm” [4]. Hybrid solids are not just a physical mixture; rather it’s a creative blend of organics and inorganics, incorporating the properties of both components [5,6]. The organic part provides the structural diversity, tunability and flexibility whereas rigidity and thermal stability is given by the inorganic components [7]. Such tailored solids not only combines the characteristics of the building blocks but can also present unusual and/or improved properties acquired from the interaction of both [8].

I.1.1 Hybrid Solids: Historical Perspective

The concept of hybridisation in developing hybrid solids is not just man’s merit; rather it is the basis of evolution. Materials like mollusc shells or crustacean carapaces, bone or tooth tissues in vertebrates, are all naturally occurring integrated hybrid systems [9]

The mixing of organic and inorganic components was carried out in ancient world. Novel mixtures of dyes or inorganic pigments were used in mural paintings thousands of years ago. The colourful pigment Maya Blue is a very good example for a hybrid material used by the Mayan people around 6th century AD, which was prepared by mixing of natural dye “indigo” and “palygorskite” , a natural fibrous and microporous clay[10]. This hybrid showed improved colour fastness, thermal and chemical stability compared to the pure components [11]. Chinese rice – lime mortars developed by mixing sticky rice soup with lime and other standard mortar ingredients were used in ancient China around 1500 years ago [12]. Amylopectin from the sticky rice organic component bound with the inorganic components such as clay minerals, calcium carbonate, and sand (silica) resulted in mechanically stable hybrids used for construction of tombs and sections of the Great Wall during the Ming dynasty [13]. Many other clay – organics were used worldwide in various fields like cosmetics and medicine [14].

However, the field of research on hybrid solids was more developed by the end of the 20th and the beginning of the 21st century, because of the availability of modern physico–chemical characterization methods, which gives a deep insight into the hybrid architectures [15]. Since then, ‘hybrid solids’ has become a mushrooming multidisciplinary research area driven by the curiosity of scientists from all fields of science.

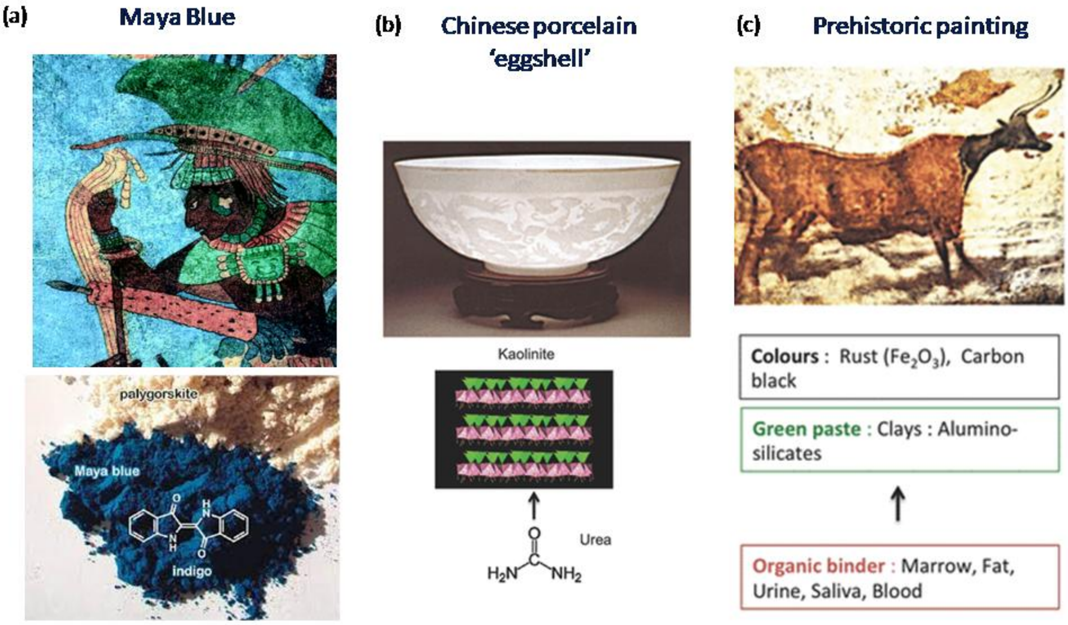

Figure I.1 A few examples of hybrid materials used in ancient world; (a) Maya blue [10], (b) Chinese porcelain [2] and (c) pre-historic paintings [2].

I.2 Classification of Hybrid Solids

The term 'hybrid solid' spans over a wide variety of materials ranging from simple metal complexes to crystalline highly ordered coordination polymers and metal organic frameworks, metal-oxo clusters, amorphous sol – gel compounds, nanocomposites and several other solids with and without interactions between the inorganic and organic units. Different authors categorise hybrid solids in various ways, making it a very subjective process. The nature of interaction between the organic and inorganic components plays a significant role in controlling the physical and chemical properties. Sanchez *et.al.* has classified hybrid solids into two main classes depending on the strength of interaction between the components [16];

Class I - Hybrid solids which are formed through weak interactions like Vander Waals interaction, hydrogen bonding or weak electrostatic interactions, between the organic and inorganic components.

Class II- Hybrid solids that are formed through strong chemical interactions in which the components are linked by covalent or ionic-covalent chemical bonds.

In this thesis, we have classified hybrid solids into two main classes based on the nature of the inorganic building blocks. Class A belongs to hybrid solids based on polyoxometalates (POMs) whereas Class B consists of hybrid solids based on transition metals. Scheme I.1 shows the various types of class A and class B hybrid solids.

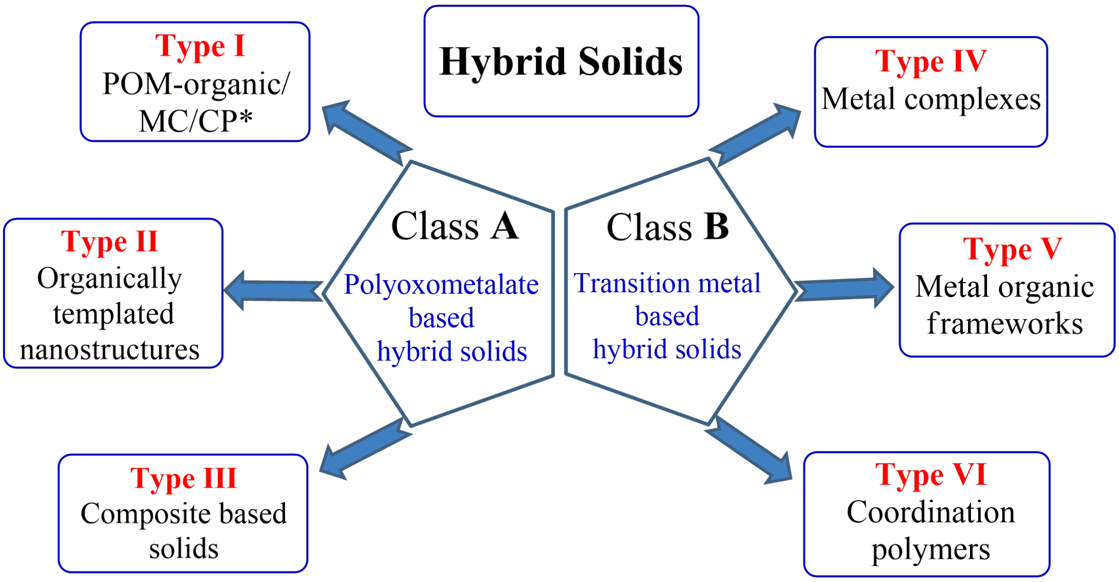

MC- Metal Complex, CP- Coordination Polymer

Scheme I.1 Different types of class A and class B hybrid solids

The work presented in this thesis is mainly focused on type I- type IV hybrid solids. Therefore, a brief explanation on POM hybrids with organic ligands/metal complexes or coordination polymers (type I), organically templated nanostructured POM hybrids (type II), composite-POM hybrids (type III) and transition metal complexes (type IV), are provided in the following sections.

I.3 Polyoxometalate based hybrid solids (Class A)

Polyoxometalates (POMs) are a significant class of polynuclear anionic clusters, made up of transition metals in high oxidation state (usually of Mo, V, W, Ta, Nb, etc.) and oxygen atoms [17]. These POMs are well known for their rich topology and intriguing physical and chemical properties and hence have received immense attention [18]. The unique properties of POMs have made them promising candidates in the fields of catalysis [19-21], magnetism [22], medicine [23-27], sensors [28] and material science [29].

POMs are broadly classified into two types; isopolyanions with the general formula ($[H_xM_yO_z]^{n-}$) which lack heteroatoms and heteropolyanions ($[X_xM_mO_y]^{q-}$, X = heteroatom, usually a first row transition metal) that contains one or more heteroatoms in the metal-oxide framework [30]. The presence of heteroatoms can bring about a great structural variety of POM solids which includes Keggin $[XM_{12}O_{40}]^{n-}$ [31], Wells-Dawson $[XM_{18}O_{62}]^{n-}$[32], Strandberg $[XM_5O_{23}]^{n-}$[33] and Anderson-Evans archetypes $[XM_6O_{24}]^{n-}$ [34,35].

In this work, hybrid solids based on Keggin type and Anderson-Evans type POMs have been synthesized and therefore, a brief structural description of these two types are discussed below.

I.3.1 Keggin type cluster, $[XM_{12}O_{40}]^{n-}$

Keggin type POM cluster, $[XM_{12}O_{40}]^{n-}$ was first structurally determined by Keggin in 1933 [31]. It consists of a central XO_4 tetrahedra surrounded by $12MO_6$ (M = Mo or V) octahedra arranged in four groups of three edge– shared octahedral, M_3O_{13}. The common site of M_3O_{13} is also linked to the central heteroatom X. Baker and Figgis have reported five geometrical isomers of Keggin ion, of which the α isomer being the more predominant and thermodynamically stable [36]. The structure of $PW_{12}O_{40}^{3-}$ studied by Keggin corresponds to α form [31]. Rotation of one, two, three or all the four M_3O_{13} units by 60° give rise to β, γ, δ and ε isomers respectively. Keggin type cluster anions when treated with alkaline solutions result in the loss of one or more metal centres thereby forming lacunary Keggin POMs [37]. The vacant sites can then be filled by suitable transition metal ions forming substituted Keggin clusters [38,39].

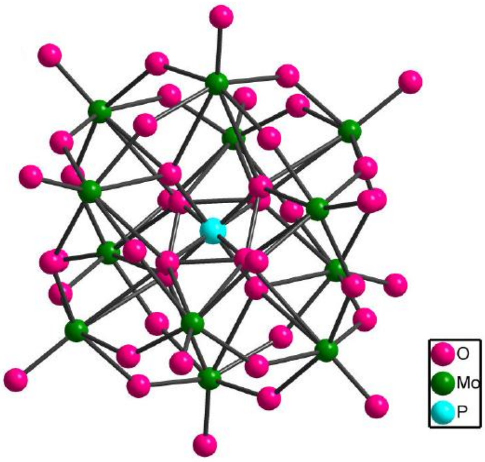

Figure I.2 Structure of Keggin type POM.

I.3.2 Anderson-Evans type cluster, $[XM_6O_{24}]^{n-}$

Anderson-Evans type is one of the most common POM clusters having the general formula $[H_x(XO_6)M_6O_{18}]^{(9-x)-}$, where x = 6-7, M = addenda atoms (Mo^{VI}) and X = a central heteroatom [40]. The structure of Anderson-type POMs was first suggested by J. S. Anderson [34] in 1937 and later confirmed by H. T. Evans [35]. It consists of six edge sharing $[MoO_6]$ or $[WO_6]$ octahedra arranged in a hexagonal manner around the central $[XO_6]$ octahedron resulting in a planar structure of D_{3d} symmetry [35]. The oxygen atoms present in the Anderson cluster exhibits three different types of coordination modes; six triple-bridged oxygen atoms (μ_3-O) connecting the two adjacent addenda atoms and the central heteroatom, six double-bridged oxygen atoms (μ_2-O) connecting two addenda atoms and two terminal oxygen atoms (O_t) linking to each of the six addenda atoms

(Figure I.3). The Anderson POM can be generally classified into two types; A-type Anderson in which all six µ3-O atoms are unprotonated with the general formula $[X^{n+}M_6O_{24}]^{(12-n)-}$ (the central heteroatom is usually in a high oxidation state, for example, X = Te^{VI}, I^{VII}) [41,42] and B-type Anderson in which the µ3-O atoms are protonated with the general formula $[X^{n+}(OH)_6M_6O_{18}]^{(6-n)-}$(heteroatoms usually in low oxidation state, for example, X = Cr^{III}, Fe^{III}) [43,44].

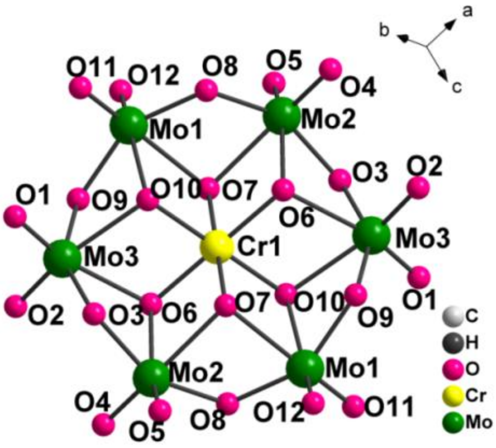

Figure I.3 Structural unit of Anderson-Evans cluster anion

Designing POM cluster hybrids

I.3.3 POM-organic ligands/MC/CP hybrids (Type I)

POM anionic clusters possess counter cations other than inorganic ions as well. POMs can frequently interact with transition metal complexes, coordination polymers, or organic ligands via self-assembly approach thereby increasing its structural diversity and thus resulting in novel POM cluster based hybrid solids [45,46]. Hence, the design and synthesis of such hybrids, which result from the incorporation of organic moieties into the metal oxide framework, have received a lot of interest. Several well-defined POM-based hybrid solids, including the Keggin [47,48], Wells-Dawson [49,50] and Lindquist kinds [51,52], have been reported. Anderson type POMs with its planar geometry are ideal inorganic building blocks and have been explored by many groups to synthesize Anderson cluster based hybrid solids with metal-organic complex or coordination polymers [53-57]. It can form hybrids in which Anderson-Evans cluster occurs as discrete anion and metal-organic complex or coordination polymer occurs as counter cation as in $[\{M_2(2\text{-pzc})_2(H_2O)_4\}\{CrMo_6(OH)_7O_{17}\}]_3.17H_2O$ (M = Co or Cu, 2-pzc = Pyrazine-2-carboxylate) and assembled through non-covalent interactions [58]. On the other hand, in some cases, Anderson cluster is coordinated to metal-organic complex or coordination polymers which are further extended to form 1-D chains, 2-D sheets, or 3-D frameworks. For example, Shivaiah *et.al.* reported a novel POM hybrid comprised of Anderson cluster anion and a coordination polymer $\{[Cu^{II}(2,2'\text{-bipy})(H_2O)_2Cl][Cu^{II}(2,2'\text{-bipy})(H_2O)_2Al(OH)_6Mo_6O_{18}].4H_2O\}$, which was the first example of an extended spiral chain hybrid structure [59]. Pavani *et. al.* has synthesized three new extended Anderson hybrids viz; $[\{Cu_2(ox)(pz)_4\}\{H_7CrMo_6O_{24}\}].11H_2O$, $[\{Cu(pz)_2(H_2O)_2\}\{Cu_2(ox)(pz)_4\}\{H_5CrMo_6O_{24}\}].8H_2O$ and $[\{Cu(pz)_3Cl\}\{Cu_2(ox)(pz)_4\}\{H_6CrMo_6O_{24}\}].8H_2O$ in which the Anderson cluster is covalently linked into 1-D chain and 2-D sheets via oxalate(*ox*) bridged copper pyrazole (*pz*) units [60]. Organic ligands also can serve as counter cations to POM anionic clusters which can assemble through supramolecular interactions as in $(H_2pip)_5[AlMo_6(OH)_6O_{18}]_2(SO_4)_2.16H_2O$ [61]. Anderson type chromium molybdates with organic cations reported in literature has been summarized in Table II.1 of chapter II.

Applications:

POM cluster hybrids not only exhibit diverse architectures but also interesting properties and hence, a wide range of promising applications especially in the field of catalysis, photochromism, material science and medicine [62,63].

The presence of termninal oxygen atoms in POMs contributes to high reactivity and therefore, POM clusters with varying counter ions are studied for their catalytic properties in a variety of reactions. For instance, Peng *et.al.* isolated a new Anderson hybrid $(H_3O)[(3\text{-}C_5H_7N_2)_2(Cr(OH)_6Mo_6O_{18})].3H_2O$ ($3\text{-}C_5H_6N_2$ = 3-aminopyridine), and found to possess good catalytic oxidation activity for eliminating acetone at lower temperature [64]. Wang's group has reported a Keggin type POM hybrid templated by a coordination polymer, $[Cu_2(H_2O)_2(bpp)_2Cl][PM_{12}O_{40}]\cdot{\sim}20H_2O$ (M = Mo; bpp = 1,3-bis(4-pyridyl)propane) which exhibited significant electrocatalytic activity towards the reduction of nitrite [65].

POMs combined with organic amines, π-conjugated molecules or polymers can form hybrid solids with enhanced photochromic properties. For instance, $(H_2DABCO)_2(NH_4)_2[Mo_7O_{24}]$ was found to exhibit photochromic behavior upon UV excitation together with trimolybdate and octamolybdate derivatives as reported by Coué *et. al*. [66]. Recently, Liu *et.al.* prepared a polyoxomolybdate-naphthalenediimide hybrid, $[Ce_2(BINDI)(DMF)_8]\cdot[Mo_6O_{19}]$, (BINDI = *N*, *N′*-bis(5-isophthalic acid)-1,4,5,8-naphthalene diimide), which showed reversible photochromic behavior under uv–visible light irradiation. It also showed good photocatalytic activity for degradation of methylene blue under visible light [67].

POMs can also form biologically active hybrid materials and hence show potential applications in medicine. Anderson type solid, $[NH_3Pr^i]_6[Mo_7O_{24}].3H_2O$ was tested *in vivo* against various tumor cell lines and exhibited potential antitumor activity [68]. A series of novel pyridinium polyoxometalates synthesized by Wang and co-workers are reported to have good anti-HIV-1 activities [69].

Apart from above fields, POM hybrids are also explored for their potential applications in macromolecular crystallography studies and magnetism [70]. The synthesis of POM cluster based hybrids continues to fascinate the researchers owing to its interesting properties and versatile applications.

I.3.4 Organically templated nanostructured POM hybrids (Type II)

Nanostructured POMs templated by organic moieties such as organic amines, proteins, surfactants, etc. constitute another prominent type of hybrid solids [71-73]. These nanostructures are self-assembled via supramolecular interactions and are much less ordered. The type of organic template used has a significant impact on the morphology and properties of the hybrid formed, in addition to other synthetic variables like pH, reactant quantity, temperature, etc. Long chain amines have been used for synthesizing nanostructured vanadium and molybdenum oxides by using soft chemistry routes [74-77]. Spahr *et. al*. isolated a lamellar type vanadium oxide hybrid templated by hexadecylamine having nanotubular morphology. The tunnel apertures were between 5 and 50 nm, and the tube diameters varied from 15 to 100 nm [74]. Molybdenum oxide nanofibres were synthesized by intercalation of primary amines into layers of MoO_3 with diameters ranging from 50-150 nm, as reported by Niederberger *et. al*. [75]. The introduction of surfactants as unique counter cations offers a feasible way of creating nanostructured POM hybrids. Surfactant encapsulated clusters are formed from a solution containing reduced POM species [78]. On the other hand, surfactants intercalated into POM framework tend to form chains and sheets, if the solution contains only the oxidized POM species [76,79]. Thomas *et.al* have investigated the growth of phosphomolybdate solids templated by dodecylpyridinium cations (DPC) under acidic conditions, and resulted in nano rods of high aspect ratio [80]. Keggin type polyoxometalate nanorods were prepared using polyethylene glycol (PEG) surfactant as a template by Yang *et. al*.[81].

Applications:

Nanostructured POM hybrids show promising applications as catalysts, pH probes, photochromic/electrochromic materials and as adsorbents for dye removal [82-85].

Peroxo polytungstophosphates (P:W = 1:4) prepared using Aliquat 336 as a surfactant showed good catalytic activity towards epoxidation of propylene [82]. Wang and co-workers have fabricated multibilayer films consisting of $Na_9[EuW_{10}O_{36}]$ (EuW_{10}) templated by dimethyldioctadecylammonium chloride (DODA) which exhibited photoluminescence [84]. Surfactant encapsulated nanospherical polyoxometalate, ($H_5[PV_2Mo_{10}O_{40}]$) was found to exhibit remarkable anionic dye removal activity [85]. Organic functionalities are particularly intriguing for bioactive POMs because they improve the POMs' association with biologically significant targets as well as their stability in specific media. Nanorods of amino acid – phosphomolybdates synthesized using reverse micelles as a template showed potential antibacterial activity against *Escherichia coli* than the individual components [86]. Such a remarkable activity could be primarily attributed to the nano-size effect.

The use of organic templates in forming nanostructured POMs has led to the expression of synergistic functionality and diverse applications in POM hybrid materials.

I.3.5 Composite based POM hybrids (Type III)

Composite based POM hybrids have gained increased attention in recent years because of their multifaceted architectures, superb redox activities, and exceptional proton and electron transport capabilities. POMs can form composites with conducting polymers, graphene, carbon nanotubes (CNTs), and metal nanoparticles (NPs) resulting in hybrid materials of improved stability and interesting properties [87-90]. Several studies have shown that embedding POMs into polymers can be used to control the nanoscale aggregation behaviour of the hybrids which in turn can affect the final properties [91,92]. Among the various polyoxometalates, Keggin and Dawson type POMs are widely used for preparing composite based hybrid solids. Cuentas-Gallegos *et al*. prepared a novel composite using Keggin type POMs and functionalized CNTs [93]. Dawson type phosphotungstate-graphene oxide composites were synthesized by Wang *et.al.*[94]. A Keggin-type POM, $H_3PMo_{12}O_{40}.nH_2O$, that can be used as a potent oxidising agent to polymerize pyrrole and form composite material has been reported by Gomez-Romero and Lira-Cantu [95].

Applications:

Composite based POM hybrids find promising applications in various fields such as photocatalysis [94], as sensors [96], supercapacitors [93] and energy storage devices [97]. A few of such applications are discussed below.

Keggin-type POM modified Ag/Graphene composite materials synthesized by Li.*et.al.* displayed excellent activity and stability for electrocatalytic oxidation of water under neutral conditions [98]. Ammam and Easton prepared a Dawson type POM-Polypyrrole composite which exhibited remarkable sensing activity towards NO_x gases [96]. Polyaniline (PANI), a conducting polymer, has been combined with Keggin POMs to form composites for supercapacitor applications [99,100]. A novel POM hybrid, $[(C_4H_9)_4N]_3[PMo_{12}O_{40}]$ and graphene composite, was reported to be an advanced cathode material for high performance lithium ion batteries (LIBs) [101]. Another Keggin type SiW12/rGO nanocomposite as a cathode material for LIBs has been reported by Wang *et. al.*[102]. POMs have also been combined with naturally occurring polymers such as chitosan, which showed enhanced thermal stability and mechanical properties [103] and were also found to possess good antimicrobial activity [104]. A review of phosphomolybdate-polymer composites and its applications, reported in the last decade, has been summarized in Table VI.1 in chapter VI.

I.4 Transition metal based hybrids (Class B)

I.4.1 Metal complexes (Type IV)

Metal complexes, comprising of transition metal atoms/ions and organic ligands linked via coordination bonds, are an intriguing class of organic-inorganic hybrid solids. The topology and properties of these hybrid solids can be tailored through judicious choice of their molecular building blocks. There are two main building blocks used for forming metal complex viz; metal ions and organic ligands.

Among the various metal ions, transition metal ions are widely used for the construction of metal complexes since they can exhibit variable oxidation state and diverse coordination geometries. For example, Cu(II) exhibits Jahn-Teller distortion and usually form distorted octahedral or distorted tetrahedral or square planar geometries. Co(II) usually prefers octahedral geometry, however, in strong acidic solutions it adopts tetrahedral form. Ni(II) and Pt(II) generally tends to form square planar geometry. Various metal ions also form other geometries like linear, trigonal planar, square pyramidal, etc.

Organic ligands are coordinated to the metal centre via the donor atoms, usually, N, S and O atoms. It can be either monodentate or multidentate for effective coordination to the metal centre. Ligand molecules also differ in their charges, being neutral or anionic. The shape of the ligand and other functionalities such as presence of aromatic rings, heteroatoms, chirality, etc. also plays crucial role in tuning the properties of the metal-complex hybrid. Heterocyclic compounds, especially N-containing heterocyclic ligands such as pyridines, pyrazines, pyrazoles, etc. are ideal moieties for coordinating with the metal ions as they possess interesting properties [105, 106]. Besides the metal ions and organic ligands, solvent molecules also play a role in the formation of metal complex, either by coordinating with the metal centre or as co-crystals.

Applications:

Transition metal complexes (TMCs) are well-known for their potential applications in various fields including medicine [107], catalysis [108], solar energy conversion [109], magnetism [110], etc. A vast number of studies of TMCs are based on their potential to be used as antimicrobial, antitumor, antiviral, antioxidant and antidiabetic agents. A novel triazene based Ni(II), Co(II), Cu(II) and Zn(II) complexes were reported to exhibit promising antidiabetic and antioxidant activity [111]. Saha *et.al.* synthesized a Cobalt complex with histidine that displayed significant antibacterial and antifungal activity against various multidrug resistant bacterial and fungal strains in comparison to commercial antibiotics [112]. A series of Cu, Zn and Cd complexes based on 2-acetylpyridine and L-tryptophan were tested for anti-cancer activity on MDA-MB-231 breast cancer cells and the Cd complex showed the highest anti-proliferative activity among the three complexes as reported by Zhang *et. al.*[113].

TMCs are studied for their catalytic properties in various reactions such as polymerization, oxidation of organic compounds, reduction of thionyl chloride, etc.[108]. For example, Iron(III) and cobalt(II) complexes based on pyridine bis(imine) ligand showed significant catalytic activity for polymerization of ethylene [114]. A new Ru(II) carbonyl complex containing ‘pincer like’ ONS donor Schiff base and triphenylphosphine was prepared by Tamizh *et. al.* for selective oxidation of alcohols at room temperature [115].

TMCs have also been explored for efficient energy storage/conversion devices including dye sensitized solar cells [116], organic light emitting diodes [117] and in drug delivery systems [118]. Several TMCs are also promising candidates as chromotropic materials [119-120]. A detailed review of chromotropism shown by complexes of Cu(II) tetrahalides with various organic ligands have been summarized in Table IV.1 in chapter IV.

I.5 Synthetic strategies

Various synthetic methods generally employed for the synthesis of type I to type IV hybrid solids mentioned above are briefly discussed in this section.

I.5.1 Solvent evaporation method

Solvent evaporation is one of the most commonly used methods for preparing POM hybrid solids and metal complexes. Reactants are dissolved in a suitable solvent and left undisturbed for crystallization, usually at room temperature. As the solution becomes saturated, either by cooling the solution or by evaporating extra solvent, crystals gradually develop. The obtained crystals are filtered, washed with water or other solvents and dried at room temperature.

I.5.2 Hydrothermal method

Hydrothermal synthesis is another technique employed in the synthesis of a wide range of hybrid solids, especially if the organic moieties have poor solubility. The reactants along with water are added into a sealed Teflon container. The reaction is carried out under autogenous pressure at temperatures ranging from 100-250°C. The apparatus is allowed to undergo slow cooling and the product obtained is filtered, washed with water or other solvents and dried. This method is especially suitable for the growth of good-quality crystals required for single crystal analysis and offers more control over the composition of the hybrid formed.

I.5.3 Sol-gel method

Sol- gel method is another technique particularly useful for the synthesis of organically templated nanoclusters and nanocomposites. The basis of this method is preparing a homogeneous sol from the molecular precursors and converting into a gel. The gel obtained is dried after removing the solvent by suitable methods. The sol-gel method is very useful for the preparation of highly homogeneous composites with very high purity.

Various other methods such as co-precipitation, layer diffusion, sonication, etc are also occasionally used for the synthesis of different types of hybrid solids.

I.6 Motivation

Polyoxometalate hybrids and transition metal complex hybrid solids holds a prominent position among the wide range of organic-inorganic hybrid materials. They exhibit interesting properties and diverse applications as evident from the literature. POM clusters can form structurally diverse hybrid solids with organic ligands, metal complexes or coordination polymers. POMs can also form interesting nanostructures templated by organic moieties such as long chain amines, surfactants, etc. When POMs are combined with polymers or carbon nanotubes, it can result in the formation of nanocomposites. This structural versatility contributes to its potential applications in the area of catalysis, sensors, material science and medicine. Transition metal ions on interaction with organic ligands form metal complexes driven by metal-ligand coordination, which shows promising applications in various fields. In addition, hybrid solids of POMs and TMCs are also capable of exhibiting supramolecular interactions such as H-bonding, C-H··π, π··π interactions, etc. that can provide extra stability to the crystal structure. However, varying the reaction parameters such as pH, temperature, nature of the metal ions, nature of the organic ligands, solvents, etc. exert a strong influence on the self-assembly process of hybrid solids.

In this context, synthesis of structurally diverse hybrid solids and investigating its properties, by varying the synthetic parameters, seems to be an interesting area of research. The study of various supramolecular interactions that dictate the self-assembly process can also throw light on the properties of hybrid solids.

I.7 Objectives

Based on the above observations, the major objectives of this thesis are,

- Synthesize Polyoxometalate (POM) hybrid solids based on Mo; to exploit its linking propensity with transition metal ions and heterocyclic organic ligands like Pyrazole and 2- aminopyrazine.
- Explore the role of supramolecular interactions such as hydrogen bonding, C-H··π, π··π interactions, etc. in the crystal packing of the hybrid solids.
- Investigate the phenomenon of 'chromotropism' in aminopyridine based copper tetrahalides.
- Explore the biological activities of selected synthesized solids.
- Investigate the effect of long chain surfactants on the composition and morphology of phosphomolybdate solids and its application in dye removal.
- Synthesize ammonium phosphomolybdate-polypyrrole composite and investigate the effect of synthetic parameters and properties.

References

1. Mir SH, Nagahara LA, Thundat T, Tabar PM, Furukawa H, Khosla A (2018) J Electrochem Soc 165(8):B3137-B3156
2. Faustini M, Nicole L, Ruiz-Hitzky E, Sanchez C (2018) Adv Funct Mater 28(27):1704158
3. Ananikov VP (2019) Nanomaterials 9(9):1197
4. Alemán JV, Chadwick AV, He J, Hess M, Horie K, Jones RG, Kratochvíl P, Meisel I, Mita I, Moad G, Penczek S, Stepto RFT (2007) Pure Appl Chem 79(10):1801-1829
5. Mobin R, Rangreez TA, Chisti HT, Inamuddin, Rezakazemi M (2019) In: Mazumder JM, Sheardown H, Al-Ahmed A (eds) Functional Polymers. Polymers and Polymeric Composites: A Reference Series, Springer, Cham
6. Gallegos AKC: Organic / Inorganic Hybrid Materials based on Conducting Organic Polymers as Electrodes for Energy Storage Devices. Institute of Materials Science of Barcelona (2003)
7. Luberda-Durnaś K: Hybrid organic-inorganic layered materials precursors of semiconducting nanostructures. Jezry Haber Institute of catalysis and surface chemistry, Cracow (2013)
8. Carraro M, Gross S (2014) Materials 7(5):3956-3989
9. Sanchez C, Arribart H, Giraud Guille MM (2005) Nature Mater 4:277-288
10. Gómez-Romero P, Sanchez C (2005) New J Chem 29:57-58
11. Olphen VH (1966) Science 154:645-646
12. Zhang K, Zhang H, Fang S, Li J, Zheng Y, Zhang B (2014) Archaeometry 56:100-115
13. Yang F, Zhang B, Ma Q (2010) Acc Chem Res 43(6):936-944

14. Carretero MI (2002) Appl Clay Sci 21:155-163
15. Kickelbick G (2006) In: Hybrid Materials. John Wiley & Sons Ltd, New York
16. Judeinstein P, Sanchez C (1996) J Mater Chem 6:511-525
17. Pope MT, Muller A (1991) Angew Chem Ind Ed Engl 30:34-48
18. Zheng ST, Yang GY (2012) Chem Soc Rev 41:7623-7646
19. Hiskia A, Troupis A, Antonaraki S, Gkika E, Papaconstantinou PKE (2006) Int J Environ Anal Chem 86:233-242
20. Rudnitskaya A, Gamelas JAF, Evtuguin DV, Legin A, (2012) New J Chem 36:1036-1042
21. Lv HJ, Geletii YV, Zhao CC, Vickers JW, Zhu GB, Luo Z, Song J, Lian TQ, Musaev DG, Hill CL (2012) Chem Soc Rev 41:7572-7589
22. Clemente-Juan JM, Coronado E, Gaita-Arino A (2012) Chem Soc Rev 41:7464-7478
23. Rhule JT, Hill CL, Judd DA (1998) Chem Rev 98:327-357
24. Geisberger G, Paulus S, Carraro M, Bonchio M, Patzke GR (2011) Chem Eur J 17:4619-4625
25. Yamase T (2013) In: Müller WEG, Wang X, Schröder HC (eds.) Biomedical Inorganic Polymers, Springer, Berlin Heidelberg
26. Ilyas Z, Shah HS, Al-Oweini R, Kortz U, Iqbal J (2014) Metallomics 6:1521-1526
27. Bijelic A, Aureliano M , Rompel A (2018) Chem Commun (Camb) 54(10):1153-1169
28. Ammam M (2013) J Mat Chem A 1:6291-6312
29. Proust A, Thouvenot R, Gouzerh P (2008) Chem Comm 16:1837-1852
30. Pope MT (1983) Heteropoly and Isopoly Oxometalates, Springer-Verlag, Berlin
31. Keggin JF (1933) Nature 132:351-351
32. Dawson B (1953) Acta Crystallogr 6:113-126
33. Strandberg R (1973) Acta Chem Scand 27:1004-1018

34. Anderson JS (1937) Nature 140:850

35. Evans HT (1948) J Am Chem Soc 70:1291-1292

36. Baker LCW, Figgis JS (1970) J Am Chem Soc 92:3794-3797

37. Baker LCW, Baker VS, Eriks K, Pope MT, Orville MS, Rollins W, Fang JH, Koh LL (1966) J Am Chem Soc 88:2329-2331

38. Kortz U, Matta S (2001) Inorg Chem 40:815-817

39. Weakley TJR, Malik SA (1967) J Inorg Nucl Chem 29:2935-2944

40. Wu P, Wang Y, Huang B, Xiao Z (2021) Nanoscale 13:7119-7133

41. Schmidt KJ, Schrobilgen GJ, Sawyer JF (1986) Acta Crystallogr Sect C: Cryst Struct Commun 42:1115-1118

42. Kondo H, Kobayashi A, Sasaki Y (1980) Acta Crystallogr Sect B:Struct Sci 36:661-664

43. Perloff A (1970) Inorg Chem 9:2228-2239

44. Wu C, Lin X, Yu R, Yang W, Lu C, Zhuang H (2001) Sci China Ser B:44:49-54

45. Gouzerh P, Proust A (1998) Chem ReV 98:77-112

46. Li XM, Guo Y, Shi T, Chen YG (2016) J Clust Sci 27:1913-1922

47. Zheng PQ, Ren YP, Long LS, Huang RB, Zheng LS (2005) Inorg Chem 44(95):1190-1192

48. Ren YP, Kong XJ, Long LS, Huang RB, Zheng LS (2006) Cryst Growth Des 6(2):572-576

49. Bareyt S, Piligkos S, Hasenknopf B, Gouzerh P, Leco^ te E, Thorimbert S, Malacria M (2005) J Am Chem Soc 127(18):6788-6794

50. Niu JY, Guo DJ, Wang JP, Zhao JW (2004) Cryst Growth Des 4(2):241-247

51. Du Y, Rheingold AL, Maatta EA (1992) J Am Chem Soc 114(1):345-346

52. Wei Y, Lu M, Cheung CFC, Barnes CL, Peng Z (2001) Inorg Chem 40(22):5489-5490

53. Wang Y, Liu XT, Xu W, Yue Y, Li B, Wu LX (2017) Inorg Chem 56:7019-7028

54. Wang Y, Kong XP, Xu W, Jiang FR, Li B, Wu LX (2018) Inorg Chem 57:3731-3741

55. Cao RG, Liu SX, Qun YL, Wang TL, Xie LH, Su ZM (2009) J Solid State Chem 182:49-54

56. Hu Y, An HY, Liu X, Yin JQ, Wang HL, Zhang H, Wang L (2014) Dalton Trans 43: 2488-2498

57. Bai X, Lin HY, Sun JJ, Liu GC, Wang X, Wang XL (2018) Inorg Chem Commun 92:151-156

58. Singh M, Ramanan A (2011) Cryst Growth Des 11:3381-3394

59. Shivaiah V, Nagaraju M, Das SK (2003) Inorg Chem 42:6604-6606

60. Pavani K, Singh M, Ramanan A (2011) Aus J Chem 64:68-76

61.Yang XD, Chen YG, Mirzaei M, Salimi AR, Yao F (2009) Inorg Chem Commun12:195-197

62. Dolbecq A, Dumas E, Mayer CR, Mialane P (2010) Chem Rev110:6009-6048

63. Rathee B, Wati M, Sindhu R, Sindhu S (2022) Orient J Chem 38(2):327-335

64. Peng ZS, Zhang CL, Shen XM, Deng Q, Cai TJ (2011) J Coord Chem 64(16):2848-2858

65. Wang X, Bi Y, Chen B, Lin H, Liu G (2008) Inorg Chem 47(7):2442-2448

66. Coué V, Dessapt R, Bujoli-Doeuff M, Evain M, Jobic S (2007) Inorg Chem 46:2824-2835

67. Liu JJ, Fu JJ, Liu T, Cheng FX (2022) J Solid State Chem 312:123236

68. Yamase T (1993) Mol Eng 3:241-262

69. Wang S, Sun W, Hu Q, Yan H, Zeng Y (2017) Bioorganic Med Chem Lett 27(11):2357-2359

70. Blazevic A, Rompel A (2016) Coord Chem Rev 307:42-64

71. Long DL, Burkholder E, Cronin L (2007) Chem Soc Rev 36:105-121

72. Boulay AG, Cooper GJT, Cronin L (2013) In: Secheresse F (ed.) Polyoxometalate Chemistry: Some recent Trends, World Scientific Pub, Singapore

73. Long DL, Tsunashima R, Cronin L (2010) Angew Chem Int Ed 49:1736-1758

74. Spahr ME, Bitterli P, Nesper R, Müller M, Krumeich Fand Nissen HU (1998) Angew Chem Int Ed 37:1263-1265

75. Niederberger M, Krumeich F, Muhr HJ, Müller M, Nesper R (2001) J Mater Chem 11:1941-1945

76. Patzke G R, Krumeich F, Nesper R (2002) Angew Chem Int Ed 41:2446-2461

77. Thomas J, Asnani M, Sharma S, Ramanan A (2008) In: Encyclopedia of nanoscience and nanotechnology, American Scientific Publishers, USA

78. Kurth DO, Lehmann P, Volkmer D, Coelfen H, Koop MJ, MullerA, Du Chesne A (2000) Chem Eur J 6:385-393

79. Spahr M E, Nesper R (2001) Z Anorg Allg Chem 627(9):2133-2138

80. Thomas J, Kannan KR, Ramanan A (2008) J Chem Sci 120(6):529-536

81. Yang Y, Cao M, Hu C, Guo Y, Wang E (2004) J Nanosci Nanotechnol 4(7):833-837

82. Kaur J, Kozhevnikov IV (2004) Catal Commun5:709-713

83. Li HL, Qi W, Li W, Sun H, Bu WF, Wu LX (2005) Adv Mater 17:2688-2692

84. Wang XL, Wang YH, Hu CW, Wang EB (2002) Mater Lett 56:305-311

85. Yao L, Lua SK, Zhang L, Wang R, Dong ZL (2014) J Hazard Mater 280:428-435

86. Kong Y, Pan L, Peng J, Xue B, Lu J, Dong B (2007) Mater Lett 61:2393-2397

87. Lin CG, Hu J, Song YF (2017) In: Advances in Inorganic Chemistry, Academic Press, UK

88. Ding D, Zhang Z, Chen R, Cai T (2016) J Hazard Mater 324:753-761

89. Park Y, Lee YC, Shin WS, Choi SJ (2010) Chem Eng J 162:685-695

90. Kishore PS, Viswanathan B, Varadarajan TK (2008) Nanoscale Res Lett 3:14-20

91. Han Y, Xiao Y, Zhang Z, Liu B, Zheng P, He S, Wang W (2017) Macromolecules 42:6543-6548

92. Han YK, Zhang ZJ, Wang YL, Xia N, Liu B, Xiao Y, Jin LX, Zheng P, Wang W (2011) Macromol Chem Phys 212:81-87

93. Gallegos AKC, Rosales MR, Baibarac M, Romero GP, Rincón ME (2007) Electrochem Commun 9(8):2088-2092

94. Wang R, Dang L, Liu Y, Jiao W (2019) Adv Powder Technol 30(7):1400-1408

95. Romero GP, Cantu LM, (1997) Adv Mater 9:144-147

96. Ammam M, Easton EB (2011) J Mater Chem 21:7886-7891

97. Herrmann S, Ritchie C, Streb C (2015) Dalton Trans 44:7092-7104

98. Li Y, Chang XR, Sang XJ, Li JS, Luo YH, Zhu ZM, You WS (2019) Eur J Inorg Chem 2019:3597-3604

99. Romero GP, Chojak M, Gallegos AKC, Asensio JA, Kulesza PJ, Pastor CN, Cantú LM (2003) Electrochem Commun 5(2):149-153

100. Cuentas-Gallegos AK, Lira-Cantú M, Casañ-Pastor N, Gómez-Romero P (2005) Adv Funct Mater 15(7):1125-1133

101. Yang H, Xie Y, Wang Y, Wu B, Chen Y, Xu B (2017) Nano-Struct Nano-Objects 11:76-81

102. Wang S, Li H, Li S, Liu F, Wu D, Feng X, Wu L (2013) Chem Eur J 19(33):10895-10902

103. Bhat AH, Bhat IUH, Khalil HPSA (2010) J Compos Mater 45:39-49

104. Matteis LD, Mitchell SG, Fuente JM (2010) J Mater Chem B2:7114-7117

105. Marinescu M, Popa CV (2022) Int J Mol Sci 23(10):5659

106. Ma D, Yan Y, Ji H, Chen C, Zhao J (2015) Chem Commun 51:17451-17454

107. Warra AA (2011) J Chem Pharm Res 3(4):951-958

108. Abu-Dief AM, Mohamed IMA (2015) Beni Suef Univ J Basic Appl Sci 4(2):119-133

109. Wagenknechta PS, Ford PC (2011) Coord Chem Rev 255:591-616

110. Carlin RL, De Jongh LJ (1986) Chem Rev 86(4):659-680

111. Philip S, Jayasree EG, Mohanan K (2020) Res Chem Intermed 46:75-99

112. Saha S, Dhanasekaran D, Chandraleka S, Panneerselvam A (2010) Adv Biol Res 4(4):224-229

113. Zhang N, Fan YH, Zhang Z, Zuo J, Zhang PF, Wang Q, Liu SB, Bi CF (2012) Inorg Chem Commn 22:68-72

114. Souane R, Isel F, Peruch F, Lutz PJ, Chimi CR (2002) Comp Rend Chim 5:43-48

115. Tamizh MM, Mereiter K, Kirchner K, Karvembu R (2012) J Organomet Chem 700:194-201

116. Meyer GJ (2005) Inorg Chem 44(20):6852-6864

117. Chi Y, Chou PT (2010) Chem Soc Rev 39:638-655

118. Ostrowski AD, Ford PC (2009) Dalton Trans 48:10660-10669

119. Li E, Jie K, Liu M, Sheng X, Zhu W, Huang F (2020) Chem Soc Rev 49:1517-1544

120. Guerchais V, Ordronneau L, Bozec HL (2010) Coord Chem Rev 254:2533-2545

Chapter II

Self-Assembly of Anderson Cluster Based Hybrid Solids: Synthesis, Structure and Application

Summary

Three Anderson-Evans type polyoxomolybdate hybrid solids $[\{\mathrm{H}pz\}_2\{H_7CrMo_6O_{24}\}]\cdot 6H_2O$ (**1**), $[\{Cr_3(O)(CH_3COO)_6(H_2O)_3\}_2\{H_7CrMo_6O_{24}\}]\cdot 24H_2O$ (**2**) and $[Na\{Na(H_2O)_3\}_2\{H_6CrMo_6O_{24}\}]\cdot 2H_2O$ **(3)** have been crystallized via solvent evaporation technique in the presence of pyrazole (*pz*) as organic ligand. The solids were characterized using single crystal X-ray diffraction, fourier transform infrared spectroscopy and thermal analysis. While, solid **1** is an example of organically templated Anderson-Evans cluster based hybrid solid (Type I); in both **2** and **3** Anderson cluster is stabilized due to inorganic cationic moieties. Crystal structure analysis of **1**-**3** suggested that supramolecular interactions facilitate the crystal packing in synthesized solids. The role of synthetic parameters in dictating the nature of self-assembly of solids in aqueous medium was analyzed and the potential of solids **1**-**3** for the synthesis of Polypyrrole or Polypyrrole composite using chemical oxidative polymerization of pyrrole was examined.

II.1 Introduction

Self-assembly of hybrid solids involves a spontaneous aggregation of molecular precursors usually driven by metal-ligand coordination and supramolecular interactions such as hydrogen bonding, $\pi\cdots\pi$ and C-H$\cdots\pi$ interactions [1, 2]. However, synthetic parameters such as temperature, pH, metal ions, nature of organic ligand and solvent can alter the nature of the reacting molecular precursors. Therefore, subtle changes in reaction parameters can affect the aggregation of molecular precursors in the reaction medium, which in turn, affects the crystallization of hybrid solids [3-6]. Polyoxometalates, particularly Anderson–Evans cluster based solids provide an excellent opportunity to explore these issues as they can form a large variety of hybrid solids ranging from organically templated cluster based solids to coordination polymer incorporated cluster anions forming extended 3-D architectures [7, 8].

Anderson-Evans cluster has the general formula $[H_x(XO_6)M_6O_{18}]^{(9-x)-}$, where x = 6-7, M = addenda atoms (Mo^{VI}) and X = a central heteroatom [9]. Since, it can incorporate various heteroatoms, inorganic and organic cations and molecules exhibiting various coordination modes, it serves as an attractive building block for the crystallization of hybrid solids having rich topology, intriguing physico-chemical properties and diverse applications [10-13]. In addition, Anderson-Evans cluster specifically exhibits a relatively high tendency to undergo protonation and incorporate a large number of lattice water molecules during crystallization [14-16]. However, there are only limited examples of organically templated Anderson-Evans cluster based solids reported in literature (refer Table II.1).Therefore, in the present work an attempt has been made to synthesize Anderson-Evans cluster based solids using organic ligands and understand the role of synthetic parameters in dictating the nature of self-assembly in aqueous medium. The results are significant as such analysis provides clues for engineering new solids with desired structure and dimensionality. In addition, the use of Anderson solids, for the synthesis of Polypyrrole (Ppy) or Polypyrrole composite via oxidative polymerization has also been investigated.

Table II.1 Organically templated Anderson-Evans cluster based solids reported in literature.

S. No.	Solid	Cell parameters	Synthetic technique	Structural description	Ref.
1	$\{\mathrm{H}pym\}_2[\{\mathrm{H_7CrMo_6O_{24}}\}]\cdot 2\mathrm{H_2O}$ *pym*= pyrimidine	Triclinic *P*-1 a = 6.830(1) Å b = 10.159(1)Å c = 10.644(2) Å α = 76.922(3)° β = 74.540(3)° γ = 87.543(4)° Z = 1	Solvent evaporation method	Anderson-Evans cluster anions linked to a pair of protonated pyrimidine moieties through C-H···O forming a zig–zag 1-D chains.	16
2	$\{(\mathrm{H}temed)_3\}[\{\mathrm{H_6CrMo_6O_{24}}\}_2]\cdot 16\mathrm{H_2O}$ *temed*= tetramethylethylenediamine	Monoclinic $P2_1/c$ a = 13.592(3) Å b = 21.475(5) Å c = 14.286(3) Å α= 90° β = 114.538(4)° γ=90° Z = 2	Solvent evaporation method	Organic amine links Anderson-Evans cluster into 1-D chains through N-H···O interactions.	16
3	$(\mathrm{BEDT\text{-}TTF})_4[\mathrm{Cr(OH)_6Mo_6O_{18}}]\cdot 2\mathrm{H_2O}$ BEDT-TTF= bis(ethylenedithio) tetrathiafulvalene]	Triclinic *P*-1 a = 5.9545(2) Å b = 16.3767(6) Å c = 21.8643(6) Å α= 110.829(2)° β = 91.262(2)° γ = 98.129(1)° Z = 1	Electrochemical synthesis	The cluster and the organic moieties are arranged alternatively leading to 1-D chains through H-bonding interactions.	17
4	$\{(\mathrm{N_2H_5CO})[(\mathrm{CH_3})_3\mathrm{N(CH_2)_2OH}]_2\}[\mathrm{H_6CrMo_6O_{24}}]\cdot 4\mathrm{H_2O}$	Monoclinic $C2/c$ a = 13.707(3) Å b = 22.113(4) Å	Solvent evaporation method at	Anderson anion cluster is linked to a pair of choline molecules and one	18

		c =13.194(3) Å α=90° β= 109.73(3)° γ= 90° Z = 4	room temperature	protonated urea molecule leading to 3-D assembly via $N_{(urea)}$-H···O interactions.	
5	$(4\text{-H}\mathit{ampy})_2[H_3O]$ $(H_7CrMo_6O_{24})\cdot$ $2H_2O$ *ampy* = aminopyridine	Triclinic *P*-1 (no. 2) *a* = 7.951(5) Å *b* = 10.036(5) Å *c* = 10.345(5) Å α= 88.976(5)° β= 78.016(5)° γ= 86.207(5)° Z = 1	Hydrothermal synthesis	Protonated 4-aminopyridine moieties and H_3O^+ cations link Anderson polyoxoanions through N-H···O interactions forming a layered structure.	19
6	$(H_3O)[(3\text{-a}\mathit{mpy})_2$ $(H_6CrMo_6O_{24})]\cdot$ $3H_2O$	Triclinic *P*-1 *a* = 7.848(8) Å *b* = 10.180(10) Å *c* = 10.410(10)Å α = 88.031(3)° β = 78.308(2)° γ = 88.842(3)° Z = 1	Hydrothermal synthesis	Protonated 3-aminopyridines link the Anderson cluster anion through strong N-H···O interactions.	20
7	$(C_4H_{10}NO)_3$ $[H_6CrMo_6O_{24}]\cdot$ $4H_2O$	Triclinic *P*-1 *a* = 7.947 (4) Å *b* = 9.965 (5) Å *c* = 13.740 (7) Å α = 110.392 (1)° β = 102.921 (1)° γ = 90.635 (1)° Z = 1	Refluxed and cooled to room temperature, followed by solvent evaporation.	The cluster anion, organic cations and water molecules are linked by N-H···O and O-H···O interactions.	21
8	$(\mathrm{H}\mathit{bipy})_2$ $[Cr(OH)_6Mo_6O_{18}$ $H](\mathit{bipy})$ *bipy* = bipyridine	Triclinic *P*-1 *a* = 8.540 (5) Å *b*= 10.593 (5)Å *c*= 11.864 (5)Å α =74.901 (5)° β =85.216 (5)° γ = 88.651 (5)° Z= 1	Hydrothermal synthesis	$[Cr(OH)_6Mo_6O_{18}]^{3-}$ anion and three *bipy* molecules, two of which are protonated are linked via H-bonding interactions leading to supramolecular assembly.	22

II.2 Experimental

II.2.1 Synthesis

All reagents were of reagent grade and were used as received from commercial sources without further purification in the present thesis. The solids were synthesized using solvent evaporation technique, similar to that reported in literature [23]. Scheme II.1 summarizes the synthetic methodology employed in this study to prepare Anderson cluster based hybrid solids. Initially, two different aqueous solutions were prepared for the synthesis of **1**. Solution A was prepared by adding $Na_2MoO_4 \cdot 2H_2O$ (2.35 mmol, Merck, 99%) to a solution of $CrCl_3 \cdot 6H_2O$ (1.57 mmol, Merck, 99%) in 15 mL of water and 5 mL of glacial acetic acid. Solution B was prepared by adding pyrazole (2.52 mmol, Merck, 99%) to a solution of $CoCl_2 \cdot 6H_2O$ (1.68 mmol, Merck, 99%) in 10 mL of water and 10 mL of methanol. Subsequently, Solution **B** was added to Solution **A** and acidified using dilute HCl. The resultant green colored solution of pH ~ 2 was left for crystallization at room temperature. After 4 weeks, purple needle like crystals of **1** were obtained, filtered, washed with acetone and air dried. Yield: 72% (based on Mo).

When Solution **A** was left undisturbed at room temperature, dark green block like crystals of **2** were obtained after 3 weeks in about 54% yield (based on Mo). The crystals of **2** were washed with acetone, filtered and air dried. The filtrate upon evaporation at room temperature resulted in pink block like crystals of **3** after 2 weeks in about 32% yield (based on Mo). Using 2-aminopyrazine (2-*ampz*) instead of pyrazole resulted in crystallization of solid [Co(2-H*ampz*)$_2$Cl$_4$], **4**, which is discussed in detail in Chapter III.

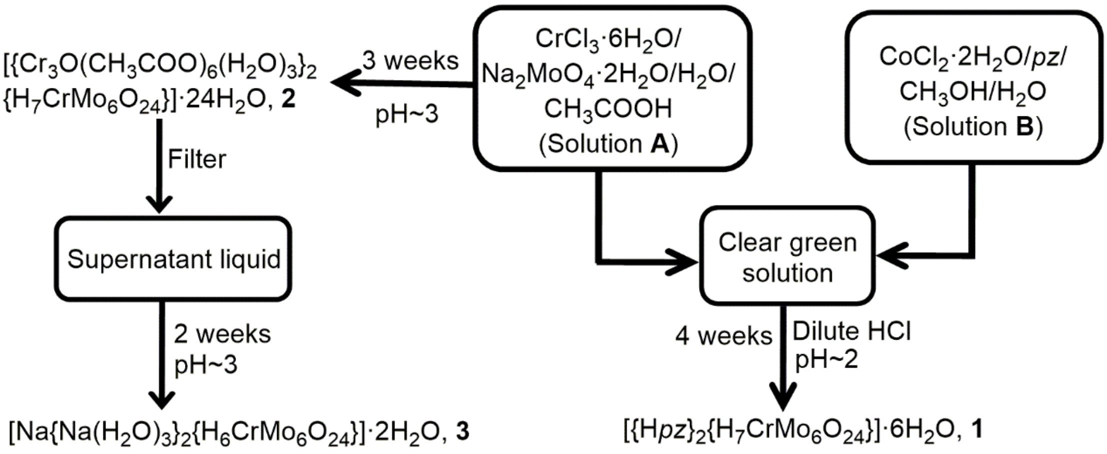

Scheme II.1 Scheme showing the synthetic pathway for the crystallization of solids **1-3**.

II.2.2 Synthesis of Polypyrrole using Anderson-Evans hybrid solids

To a stirring solution of 10 mL of $[\{Cr_3(O)(CH_3COO)_6(H_2O)_3\}_2\{H_7CrMo_6O_{24}\}].24H_2O$, **2** (0.03M), 0.5 mL pyrrole dissolved in 20mL of distilled water was added, followed by 0.02g of ammonium persulphate (APS). The contents were stirred for about 15 minutes and the resultant black powder was washed with distilled water, filtered and dried in oven at 50°C. The same procedure was repeated with solid **3**. Polypyrrole was also synthesized using only APS with the same concentration of pyrrole and APS as stated above.

II.2.3 Characterization

II.2.3.1 X-ray crystallographic studies

X-ray diffraction studies of crystal mounted on a capillary were carried out on a BRUKER AXS SMART-APEX diffractometer with a CCD area detector (MoKα = 0.71073Å, monochromator: graphite) [24]. Frames were collected at T = 298K (for **1**) and 293K (for **2** and **3**) by ω, ϕ and 2θ-rotation at 10s per frame with SAINT [25]. The measured intensities were reduced to F^2 and corrected for absorption with SADABS [25]. Structure solution, refinement, and data output were carried out with the SHELXTL program [26]. Non-hydrogen atoms were refined anisotropically. C-H and N-H hydrogen atoms were placed in geometrically calculated positions by using a riding model. Images were created with the DIAMOND program [27]. Hydrogen bonding interactions in the crystal lattice were calculated with SHELXTL and DIAMOND [26, 27]. Crystal and refinement data have been summarized in Table II.2.

II.2.3.2 Powder X-ray diffraction

Powder X-ray diffraction **(**PXRD) data was collected on a Malvern Panalytical Aeris diffractometer using Ni-filtered CuKα radiation. Data were collected with a step size of 0.02° and count time of 2s per step over the range $5° < 2\theta < 60°$.

II.2.3.3 Fourier Transform Infrared Spectroscopy

Fourier transform infrared (FTIR) spectra were recorded using Shimadzu FTIR spectrophotometer (model: IR Affinity-1S) equipped with Attenuated total reflection (ATR) in the range 400-4000 cm^{-1}.

II.2.3.4 Thermogravimetric Analysis

Thermogravimetric analysis (TGA) was done on Perkin-Elmer TGA7 from room temperature to $900^{o}C$ at a heating rate of $10^{o}C$/min. in nitrogen atmosphere to determine water and organic content as well as overall thermal stability of the products.

Table II.2 Crystal data and structure refinement parameters for **1-3**.

	1	**2**	**3**
Chemical formula	$C_6H_{22}CrMo_6N_4O_{30}$	$C_{24}H_{36}Cr_7Mo_6O_{80}$	$CrMo_6Na_3O_{32}$
Molecular weight	1257.91	2544.17	1208.61
Temperature (K)	298(2)	293(2)	293(2)
Crystal system	orthorhombic	Triclinic	Triclinic
Space Group	*Pbca*	*P*-1	*P*-1
a (Å)	23.1796(8)	10.1347(14)	6.4631(16)
b (Å)	11.1281(4)	14.688(2)	10.904(3)
c (Å)	25.1499(9)	15.442(2)	10.929(3)
α (°)	90.00	108.076(2)	109.100(4)
β (°)	90.00	93.539(2)	106.790(4)
γ (°)	90.00	92.825(2)	95.509(4)
Volume ($Å^3$)	6487.3(4)	2175.4(5)	681.1(3)
Z	8	1	1
ρcalc ($g\cdot cm^{-3}$)	2.576	1.942	2.700
μ (mm^{-1})	2.678	1.791	2.727
F (000)	4816	1240.0	1274
Crystal size (mm)	0.47 x 0.31 x 0.26	0.35 x 0.29 x 0.25	0.37 x 0.27 x0.22
Radiation	Mo *K*α	Mo *K*α	Mo *K*α
2Θ range for data collection (°)	4.12 to 56.280	2 to 60	2.08 to 50
Index ranges	$-28 \leq h \leq 30$, $-14 \leq k \leq 13$, $-33 \leq l \leq 29$	$-12 \leq h \leq 12$, $-17 \leq k \leq 17$, $-18 \leq l \leq 18$	$0 \leq h \leq 13$, $-12 \leq k \leq 13$, $-16 \leq l \leq 17$
Reflections collected	38438	20309	7773
Independent reflections	7911	7660	3380
Data/restraints/parameters	7911/0/442	7660/0/535	5549/0/433
Goodness-of-fit on F^2	1.061	1.051	1.125
$R[F^2 > 2\sigma(F^2)]$, $wR(F^2)$	0.0338, 0.0841	0.0313, 0.0954	0.0344, 0.0776

II.3 Results and Discussion

II.3.1 Crystal Structure of 1-3

II.3.1.1 Crystal Structure of 1

The asymmetric unit of **1** consists of one Anderson-Evans cluster anion, two protonated pyrazole moieties (designated as {N1N2} and {N3N4} hence forth) and six lattice water molecules. The crystal structure analysis of **1** revealed that Anderson-Evans cluster anion was identical to those reported in literature (Table II.1). The Anderson cluster anion *viz.* $[H_7CrMo_6O_{24}]$ was a B-type Anderson structure consisting of six $[MoO_6]$ octahedra arranged in a hexagonal manner around the central $[Cr(OH)_6]$ octahedron (FigureII.1). Each $[MoO_6]$ octahedra exhibited three kinds of Mo-O distances in **1**(Table II.3). These included molybdenum-terminal oxygen, Mo-Ot bonds (1.695(2)-1.709(2) Å) and two types of molybdenum bridging oxygen bonds namely Mo-Ob and Mo-Oc. While, Ob adopted a μ_2-bridging mode linking two adjacent molybdenum centers (1.892(2)-2.037(2) Å), Oc adopted μ_3-bridging mode linking two molybdenum centers and the central chromium atom (2.268(2)-2.314(2) Å). The bond-valence sum calculations [28] suggested that Cr was in +3 oxidation state, all Mo atoms were in the +6 oxidation state and seven oxygen atoms in **1** were protonated. Lattice water molecules namely O1S, O2S, O5S and O6S formed strong hydrogen bonds (Table II.4) with the cluster ions to form zig-zag 1-D chains propagating along *b* axis (FigureII.2). One of the pyrazole moieties *viz.* {N1N2} was linked to cluster anions via O1S through N-H···O interactions. O2S connected the 1-D chains via H-bonding interactions to form a sheet along *ab*-plane (FigureII.3). The sheets were further connected via lattice water molecules (O3S and O4S) and {N3N4} moiety to form 3-D supramolecular structure as shown in Figure II.4.

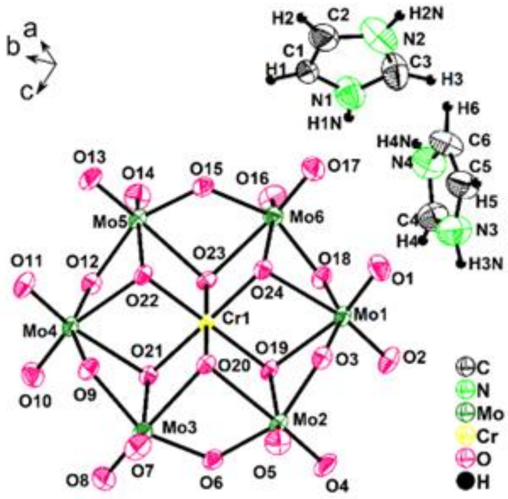

Figure II.1 ORTEP diagram of **1.** Non hydrogen atoms are shown as 50% ellipsoids and hydrogen atoms as arbitrary spheres. Lattice water molecules have been omitted for clarity.

Table II.3 Mo-O distances in **1**.

Category	**Mo···O**	**Bond Distance (Å)**
Molybdenum-terminal oxygen (Mo-Ot)	Mo1···O1	1.697(2)
	Mo1··· O2	1.706(2)
	Mo2···O7	1.691(2)
	Mo2···O8	1.690(2)
	Mo3···O11	1.702(2)
	Mo3···O12	1.706(2)
	Mo4···O15	1.705(2)
	Mo4···O16	1.708(2)
	Mo5··· O19	1.695(2)
	Mo5···O20	1.706(2)
	Mo6···O23	1.699(2)
	Mo6··· O24	1.709(2)
Molybdenum-bridging oxygen (Mo-Ob)	Mo1··· O6	1.946(2)
	Mo1··· O3	1.936(2)
	Mo2···O6	1.905(2)
	Mo2··· O9	2.037(2)
	Mo3··· O9	2.028(2)
	Mo3··· O13	1.899(2)
	Mo4··· O13	1.986(2)
	Mo4··· O17	1.892(2)
	Mo5··· O17	1.961(2)
	Mo5···O22	1.915(2)
	Mo6···O22	1.932(2)
	Mo6··· O3	1.946(2)

Molybdenum-internal oxygen (Mo-Oc)	Mo1···O4	2.280(2)
	Mo1··· O5	2.303(2)
	Mo2···O5	2.299(2)
	Mo2···O10	2.273(2)
	Mo3··· O10	2.272(2)
	Mo3··· O14	2.268(2)
	Mo4··· O14	2.274(2)
	Mo4··· O18	2.287(2)
	Mo5··· O18	2.299(2)
	Mo5···O21	2.314(2)
	Mo6··· O21	2.300(2)
	Mo6··· O4	2.279(2)

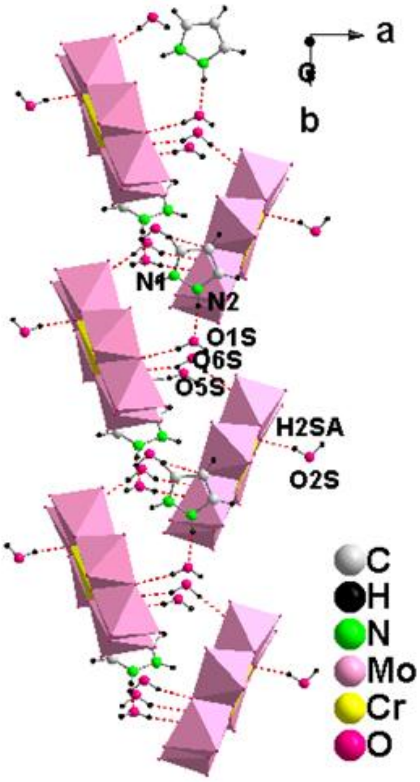

Figure II.2 1-D zig-zag chains in **1**. H-bonding interactions are shown in dashed red lines. Each cluster anion is linked to lattice water molecules O1S, O2S, O5S and O6S through H-bonding. Lattice water molecule, O1S is linked to {N1N2} moiety through N-H···O interaction.

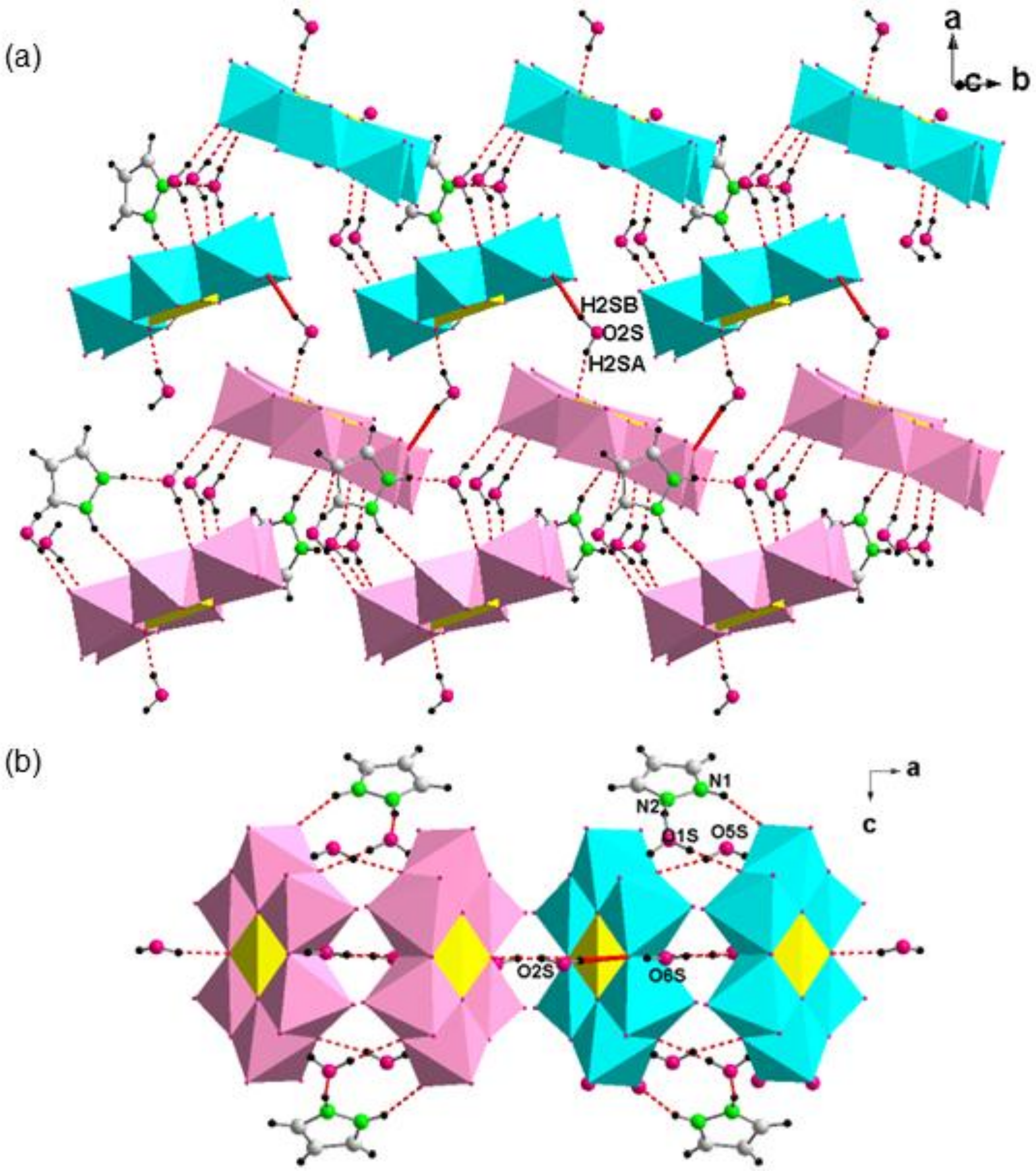

Figure II.3 (a) O2S connecting two neighboring 1-D zig-zag chains (depicted in cyan and pink polyhedral) to form 2-D sheet in **1**. Inter-chain H-bonding interactions are shown in solid red lines. (b) View along *b* axis showing two 1-D chains forming a sheet.

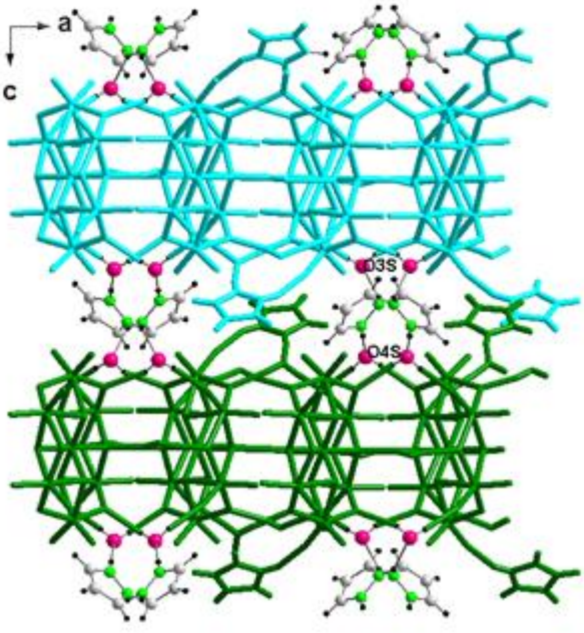

Figure II.4 View along *b* axis showing O3S and O4S connecting two neighboring sheets (depicted in cyan and green) via H-bonding interactions mediated by {N3N4} moiety in **1**.

Table II.4 H-bonding interactions in **1**.

D-H···A	**D-H (Å)**	**H···A (Å)**	**D···A (Å)**	**∠D-H···A (°)**
O(1S)-H(1SA)···O15	0.8510(27)	1.9202(19)	2.7628(32)	170.3(1)
O(1S)-H(1SB)···O5	0.8500(27)	2.0211(23)	2.8657(36)	172.3(1)
O(2S)-H(2SA)···O19	0.8489(28)	1.7511(19)	2.5699(32)	161.4(1)
O(2S)-H(2SB)···O12	0.8495(30)	1.9548(21)	2.7863(35)	165.8(1)
O(3S)-H(3SA)···O18	0.8507(28)	2.0102(19)	2.8175(33)	158.1(1)
O(3S)-H(3SB)···O14	0.8501(28)	1.9859(23)	2.8316(36)	173.0(1)
O(4S)-H(4SA)···O6	0.8509(30)	1.9710(19)	2.7902(35)	161.2(2)
O(4S)-H(4SB)···O10	0.8514(30)	2.0048(22)	2.8364(37)	165.2(2)
O(5S)-H(5SA)···O6	0.8494(24)	1.7503(19)	2.5757(30)	163.3(1)
O(5S)-H(5SB)···O10	0.8514(23)	1.9300(23)	2.7790(33)	174.8(1)
O(6S)-H(6SA)···O6	0.8492(28)	1.7807(19)	2.5732(32)	154.4(1)
O(6S)-H(6SB)···O3	0.8492(29)	1.9194(21)	2.7649(35)	173.5(1)
N(2)-H(2N) ···O(1S)	0.8608(32)	1.8238(32)	2.6733(46)	168.7(2)
N(3)-H(4N) ···O(4S)	0.8603(42)	1.8444(33)	2.7047(54)	179.5(2)
N(4)-H(4) ···O(3S)	0.8598(38)	1. 9493(30)	2.7090(49)	146.6(2)

Table II.5 O···O interactions in **1**.

O···O	**Bond distance (Å)**
O2···O23	2.7329(27)
O11···O24	2.7561(27)
O4···O21	2.6807(27)
O13···O20	2.6838(28)

II.3.1.2 Crystal Structure of 2

Solvent evaporation of Solution A (as shown in Scheme II.1) resulted in the crystallization of green block like crystals of $[\{Cr_3(O)(CH_3COO)_6(H_2O)_3\}_2\{H_7CrMo_6O_{24}\}].24H_2O$, **2**. The asymmetric unit of **2** consists of an Anderson-Evans cluster anion, $[H_7CrMo_6O_{24}]^{2-}$and the counter cation being a chromium trinuclear cluster, $[\{Cr_3(O)(CH_3COO)_6(H_2O)_3\}^{3+}$ as shown in Figure II.5. The inter cluster regions are occupied by twenty four lattice water molecules. Similar to the crystal structure of **1,** the Anderson cluster anion *viz.* $[H_7CrMo_6O_{24}]$, a B-type Anderson structure consist of six $[MoO_6]$ octahedra arranged in a hexagonal manner around the central $[Cr(OH)_6]$ octahedron (Figure II.5).The Mo-O distances in $[MoO_6]$ octahedra in **2** (Table II.6) ranges from 1.685(3)-1.709(2)Å for molybdenum-terminal oxygen (Mo-Ot), 1.935(3)-1.983(3) Å for molybdenum bridging oxygen (Mo-Ob) and 2.270(3)-2.314(3)Å for Mo-Oc bonds. The bond valence sum calculations suggested +3 oxidation state for Cr atoms and +6 oxidation state for all Mo atoms and protonation of seven oxygen atoms in **2**. Strong intermolecular hydrogen bonding interactions in **2** (2.462(4)-2.529(5) Å, Table II.7) between Anderson cluster and chromium acetate complex leads to 1-D chain (Figure II.6). The chains are further connected by inter chain H-bonding interactions (2.620(4)-2.641(4) Å) to form 2-D sheets as shown in Figure II.7. The packing of 2-D sheets into 3-D supramolecular structure is facilitated by lattice water molecules mediated by O···O interactions (2.604(6)-3.090(6) Å) as shown in Figure II.8a. Figure II.8b shows the interaction of water molecules resulting in 1-D zig-zag chain in **2**.

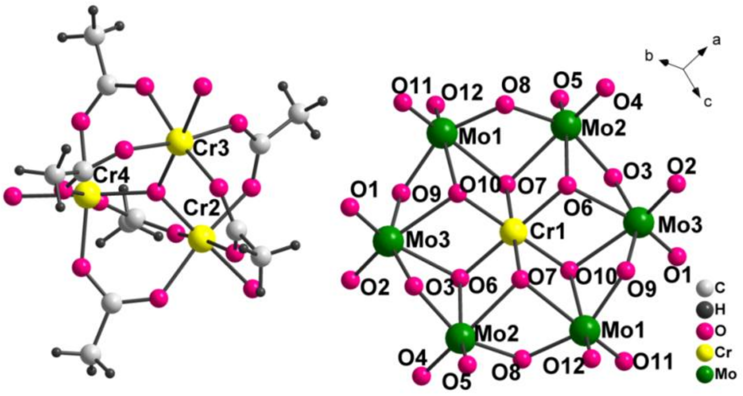

Figure II.5 Asymmetric unit in **2**. Lattice water molecules are omitted for clarity.

Table II.6 Mo-O distances in **2**.

Category	**Mo···O**	**Bond Distance (Å)**
Molybdenum-terminal oxygen (Mo-Ot)	Mo1···O11	1.689(3)
	Mo1···O12	1.704(3)
	Mo2···O4	1.697(3)
	Mo2···O5	1.707(3)
	Mo3···O1	1.685(3)
	Mo3···O2	1.709(2)
Molybdenum-bridging oxygen (Mo-Ob)	Mo1···O8	1.936(3)
	Mo1···O9	1.983(3)
	Mo2···O3	1.952(3)
	Mo2···O8	1.940(3)
	Mo3···O3	1.935(3)
	Mo3···O9	1.970(3)
Molybdenum-internal oxygen (Mo-Oc)	Mo1···O7	2.314(3)
	Mo1···O10	2.276(3)
	Mo2···O6	2.270(3)
	Mo2···O7	2.285(2)
	Mo3···O6	2.295(3)
	Mo3···O10	2.307(2)

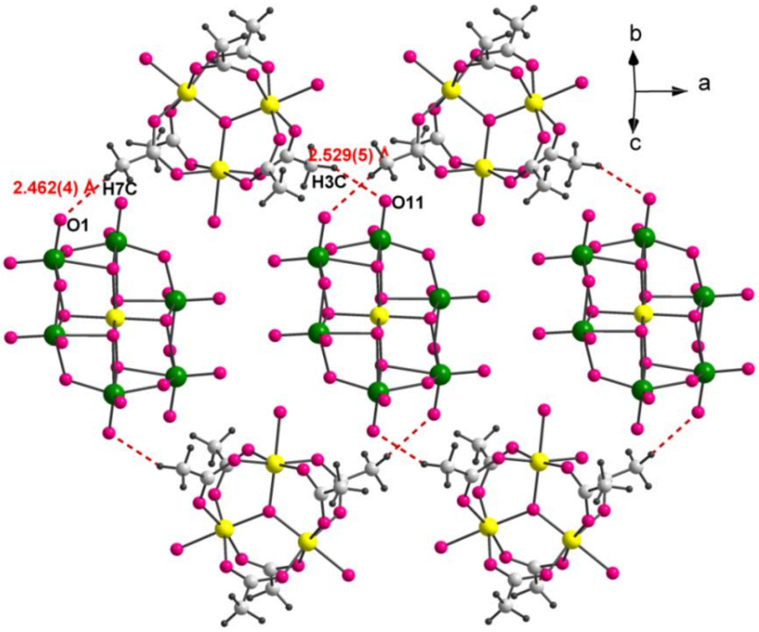

Figure II.6 Anderson clusters are connected by H-bonding interactions through chromium acetate complex to form 1-D chain.

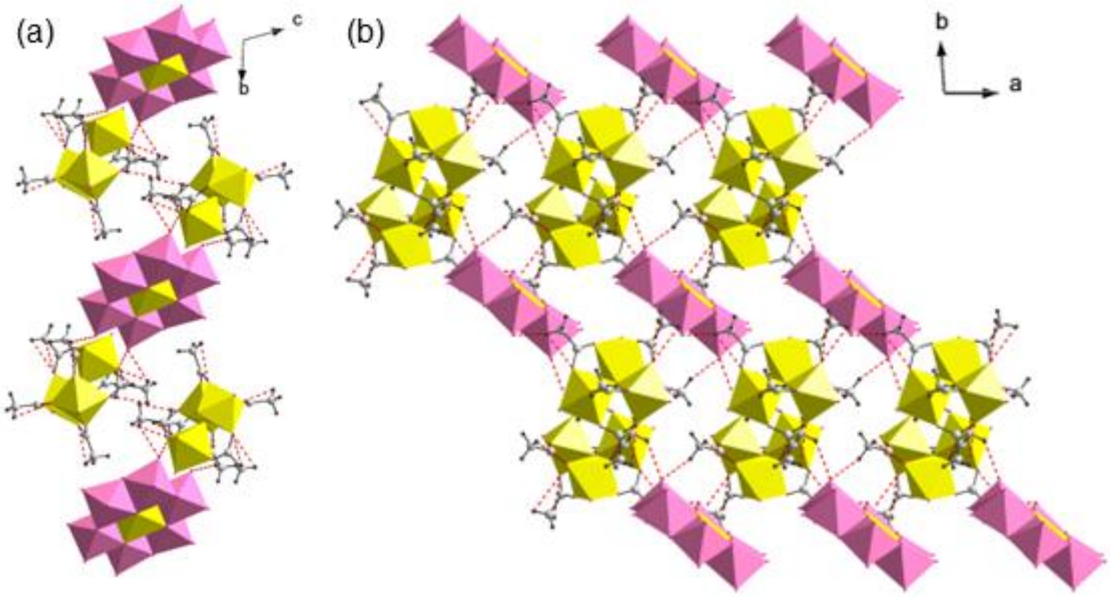

Figure II.7 (a) View along *a* axis showing 2-D sheets in **2** formed by H-bonding interactions between Anderson cluster and chromium acetate species. (b) View along *c* axis showing 2-D sheets in **2**.

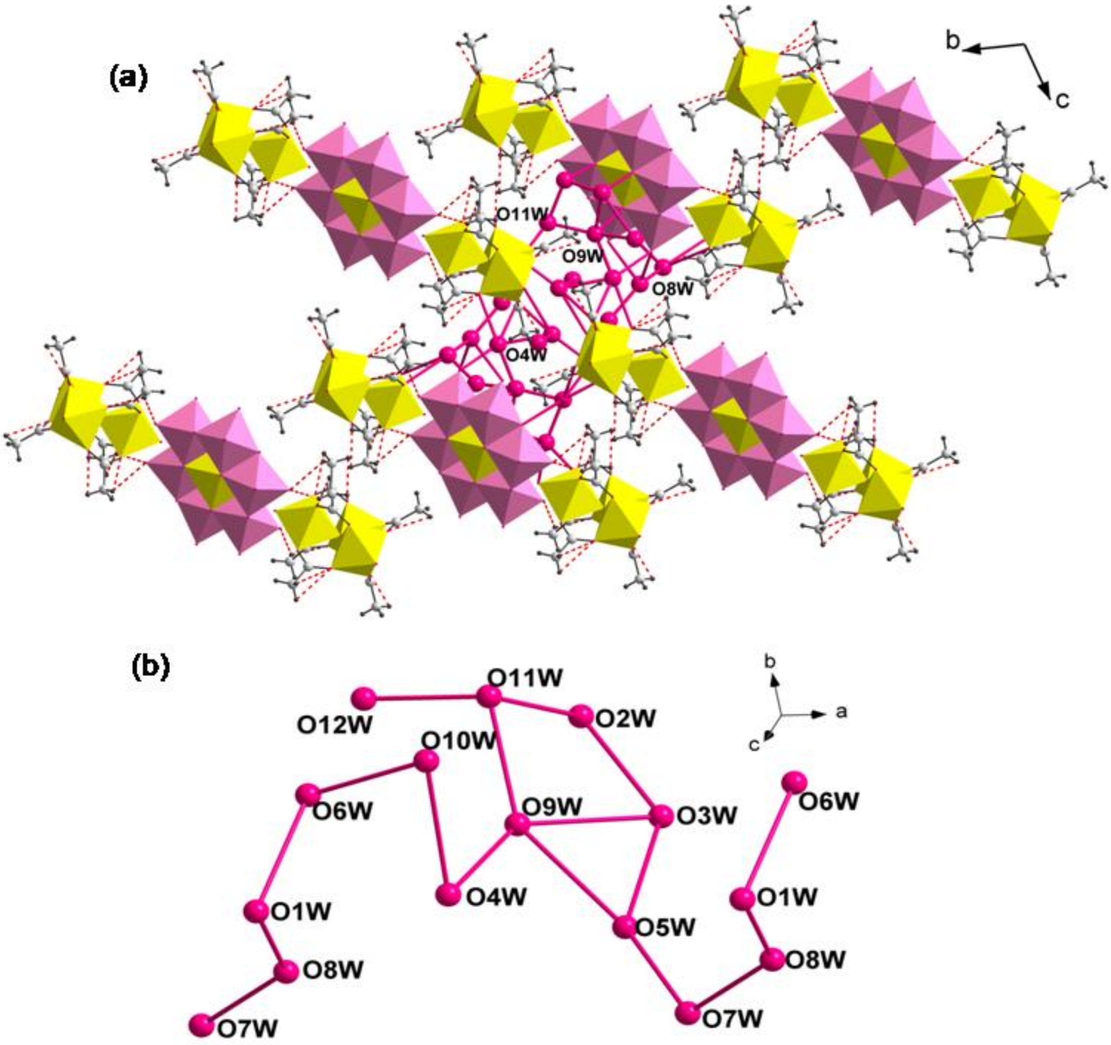

Figure II.8 (a) Two neighboring sheets are connected via hydrogen bonded clusters to form 3-D supramolecular structure. Lattice water molecules are shown in pink color and O···O interactions are shown in solid pink lines. (b) Water-water interactions resulting in 1-D zig-zag chain of water cluster in **2**.

Table II.7 H-bonding interactions in **2**.

D-H...A	**D-H (Å)**	**H...A (Å)**	**D...A (Å)**	**∠D-H...A (°)**
C3-H3C⋯O11	0.961(5)	2.529(5)	3.426(8)	155.44(3)
C7-H7C⋯O1	0.960(4)	2.462(4)	3.327(6)	149.81(2)
C9-H9B⋯O5	0.960(5)	2.641(4)	3.517(7)	151.99(3)
C1-H1A⋯O1	0.960(5)	2.620(4)	3.278(7)	126.13(2)
C3-H3A⋯O8	0.960(5)	2.777(6)	3.635(8)	149.37(2)
C1-H1A⋯O12W	0.960(5)	2.759(7)	3.539(9)	139.0(3)

Table II.8 O⋯O interactions in **2**.

O⋯O	Bond distance(Å)
O1w ⋯O8w	2.710
O7w⋯O8w	2.799
O6w⋯O8w	3.071
O6w⋯O10w	2.879
O4w⋯O10w	3.047
O4w⋯O9w	2.746
O5w⋯O9w	3.075
O5w⋯O7w	2.865
O9w⋯O11w	2.761
O3w⋯O5w	3.200
O3w⋯O9w	3.090
O2w⋯O3w	2.779
O2w⋯O11w	2.722
O11w⋯O12w	2.604

II.3.1.3 Crystal Structure of 3

The supernatant liquid after filtration of **2** was left undisturbed at room temperature and it resulted in the formation of pink crystals of $[Na\{Na(H_2O)_3\}_2\{H_6CrMo_6O_{24}\}].2H_2O$, **3**. It consists of Anderson cluster anion $[H_6CrMo_6O_{24}]^{3-}$ and hydrated sodium cations along with two lattice water molecules. Of the two sodium centers, Na2 is surrounded by lattice water molecules forming 1-D chains propagating along *c* axis (Figure II.9). Neighboring Na2 hydrate chains are connected by Anderson clusters to form 2-D sheets as shown in

Figure II.10. These neighboring 2-D sheets are further connected by sodium (Na1) hydrate complexes to form 3-D structure as shown in Figure II.11. The bond-valence calculations suggested that Cr atoms are in the +3 oxidation state and all Mo atoms are in the +6 oxidation state in **3**.

Table II.9 Mo-O distances in **3**.

Category	**Mo···O**	**Bond Distance (Å)**
Molybdenum-terminal oxygen (Mo-Ot)	Mo1···O1	1.694(2)
	Mo1···O2	1.708(3)
	Mo2···O3	1.709(3)
	Mo2···O4	1.718(2)
	Mo3···O5	1.696(2)
	Mo3···O6	1.685(2)
	Mo4···O7	1.695(1)
	Mo4···O8	1.707(3)
	Mo5···O9	1.703(3)
	Mo5···O10	1.709(2)
	Mo6···O11	1.699(2)
	Mo6···O12	1.696(2)
Molybdenum-bridging oxygen (Mo-Ob)	Mo1···O13	1.907(1)
	Mo1···O14	1.951(2)
	Mo2···O14	1.956(1)
	Mo2···O15	1.904(3)
	Mo3···O15	1.945(3)
	Mo3···O16	1.934(4)
	Mo4···O16	1.919(1)
	Mo4···O17	1.940(2)
	Mo5···O17	1.946(1)
	Mo5···O18	1.918(3)
	Mo6···O13	1.959(4)
	Mo6···O18	1.931(3)
Molybdenum-internal oxygen (Mo-Oc)	Mo1···O20	2.293(4)
	Mo1···O10	2.276(3)
	Mo1···O21	2.260(3)
	Mo2···O21	2.263(1)
	Mo2···O22	2.302(5)
	Mo3···O22	2.372(2)
	Mo3···O23	2.300(1)
	Mo4···O23	2.289(4)
Molybdenum-internal oxygen (Mo-Oc)	Mo4···O24	2.306(3)
	Mo5···O24	2.287(1)
	Mo5···O19	2.301(5)
	Mo6···O19	2.295(2)
	Mo6···O20	2.293(1)

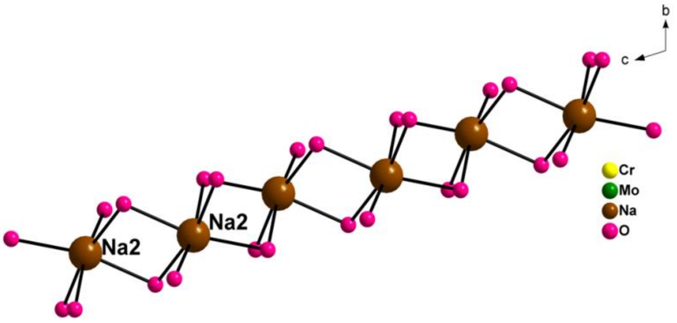

Figure II.9 Two sodium centers (Na2) connected by lattice water molecules forming 1-D chains propagating along *c* axis in **3**.

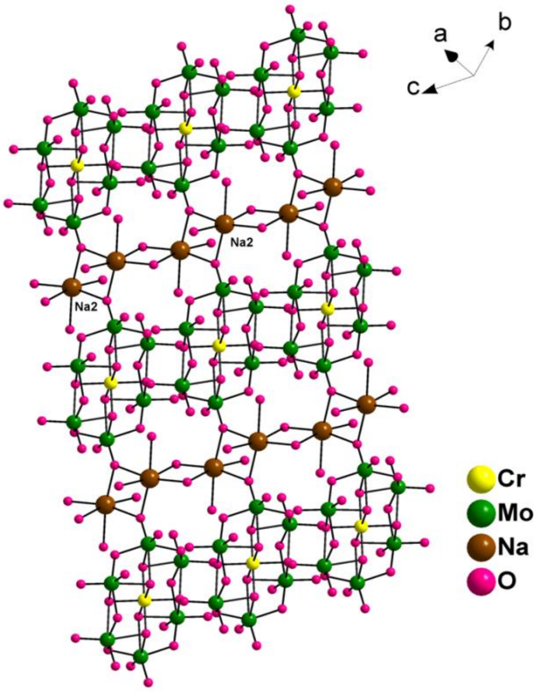

Figure II.10 Neighboring Na2 hydrate chains are connected by Anderson clusters to form 2-D sheets in **3**.

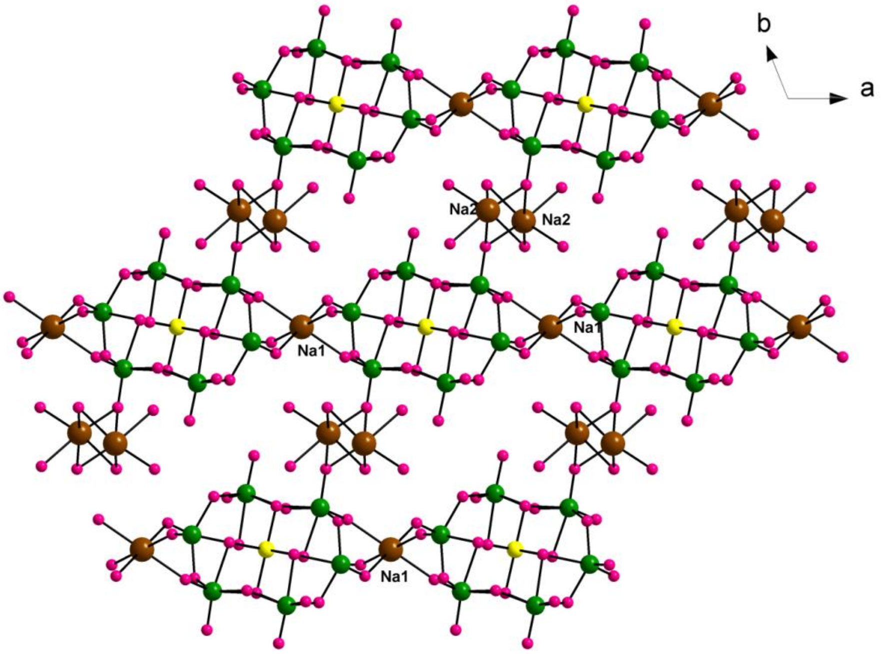

Figure II.11 2-D sheets are connected by sodium (Na1) hydrate complexes to form 3-D structure.

II.3.2 Vibrational and Thermal Analysis

The FTIR spectra of solids **1**-**3** displayed similar vibrations which are characteristic of the Anderson-type structure (Figure II.12). Vibrational bands were observed between 890 and 950 cm^{-1} for the Mo-Ot bonds, between 660 and 740 cm^{-1} for the Mo-Ob groups, and between 400 and 600 cm^{-1} for the Mo-Oc groups. In **1**, peaks in the range 3000-3300 cm^{-1} could be attributed to stretching vibrations of the N-H group in the pyrazole moiety. Peaks at 1621 and 1517 cm^{-1} corresponded to C-N stretching and N-H bending vibrations respectively. In **2**, strong bands at 1612 and 1456 cm^{-1}were attributed to $\nu_{as}(CO_2)$ and ν_s (CO_2) modes, respectively of the bridging acetic acid groups and strong band observed at 665 cm^{-1} were attributed to the $\nu_{as}(Cr_3O)$ vibration. **3** also showed IR spectra characteristics of the Anderson cluster anion.

TG analysis of **1** (FigureII.13a) showed weight loss in three steps. In **1**, the first weight loss upto 110°C corresponding to 8.9% was due to loss of six lattice water molecules (calcd. 8.6%). The thermal degradation of two pyrazole moieties could be accounted for the second weight loss of 11.4% upto350°C (calcd. 10.9%). Subsequent loss could be assigned to the decomposition of $\{CrMo_6O_{24}\}$ cluster anion.TGA of solids **2** and **3** showed the weight loss in multiple steps wherein the first step was due to loss of lattice water molecules. In **2**, weight loss in next step was observed corresponding to the loss of chromium trinuclear complex, followed by degradation of Anderson cluster (Figure II.13b). **3** showed loss of lattice water molecules and degradation of Anderson cluster (Figure II.13c).

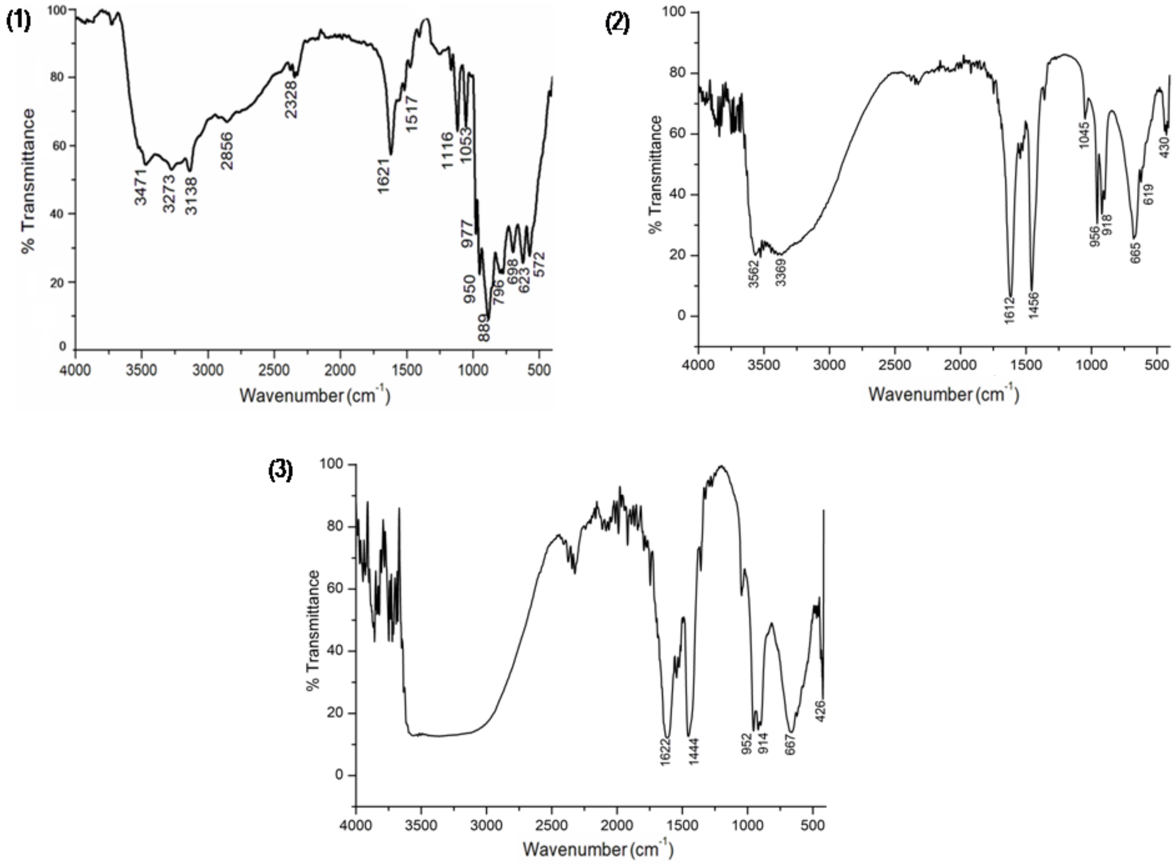

Figure II.12 FTIR spectra of solids **1, 2** and **3**.

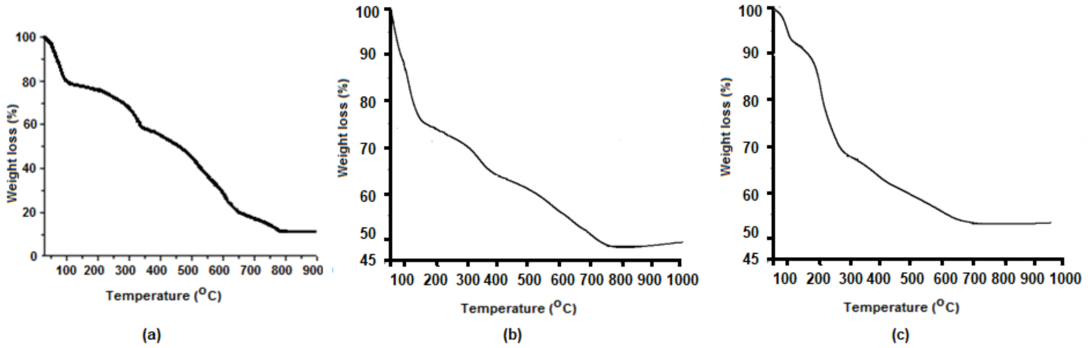

Figure II.13 TG analysis plot of (a) **1**, (b) **2** and (c) **3.**

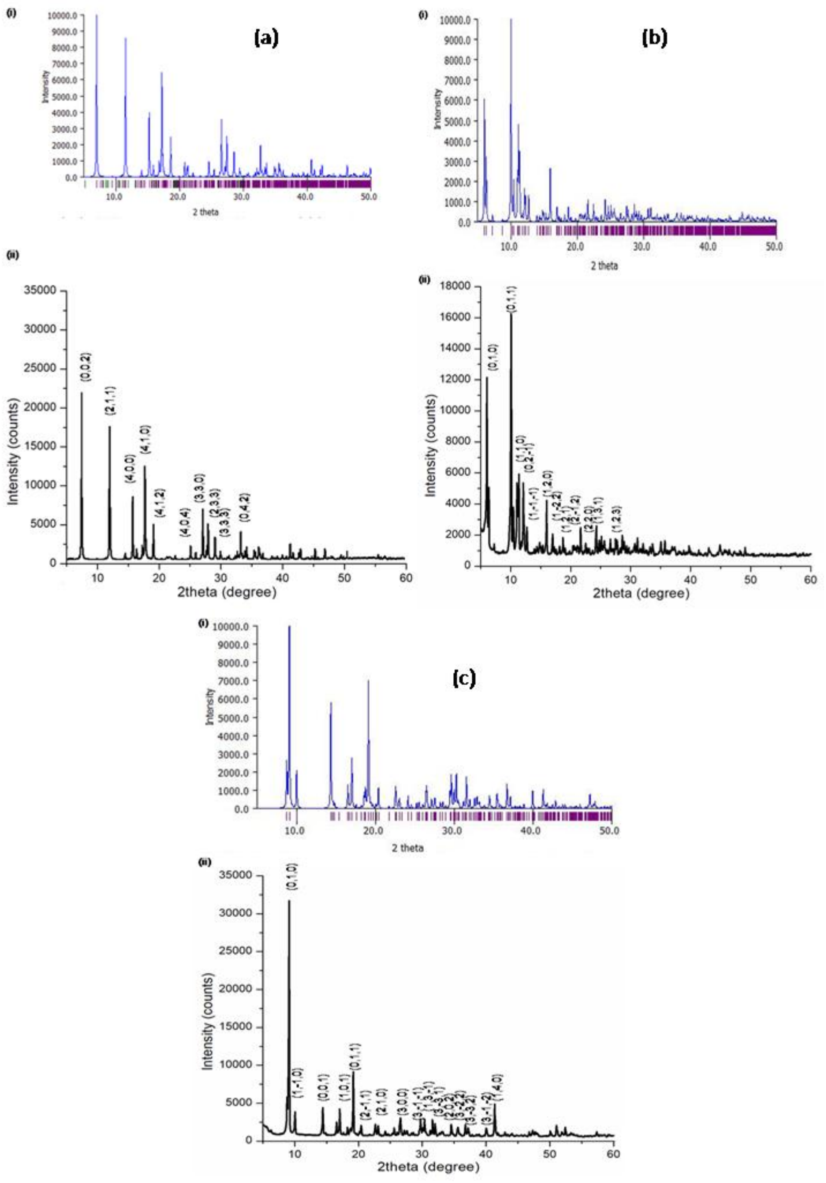

Figure II.14 (i) Simulated and (ii) experimental powder X-ray patterns of (a) **1**, (b) **2** and (c) **3.**

II.3.3 Chemistry of Formation

Self-assembly of Anderson-Evans cluster based solids usually occurs via solvent evaporation technique under acidic conditions. The synthetic methodology used in the current investigation involved mixing of aqueous molybdate solution containing chromium ions with a solution of cobalt ions in the presence of an organic ligand *viz.* pyrazole, under constant stirring. Once the two solutions were mixed, the solution was further acidified using HCl. Finally, the resultant solution when left undisturbed resulted in crystallization of solid **1**. The addition of HCl resulted in a decrease in the pH of the reaction medium and provided large number of protons in the solution. Therefore, the addition of HCl had a twofold effect. Firstly, the highly acidic pH favored the formation of protonated $[Hx(XO_6)M_6O_{18}]^{(9-x)-}$ cluster species and secondly, it resulted in the protonation of the organic ligands. Therefore, in the case of **1**, the increase in positively charged organic moieties $(H\mathit{pz})^+$ (pKa of pyrazole: 2.1[29]) inhibited cobalt-pyrazole interaction resulting in an organically templated hybrid solid $[\{H\mathit{pz}\}_2\{H_7CrMo_6O_{24}\}]\cdot 6H_2O$ (**1**). Additionally, the crystal structure of **1** also showed the presence of six lattice water molecules. Earlier it has been demonstrated in several examples that aggregation of water cluster is a secondary factor in the crystal packing of such complex structures [16]. Protonation of Anderson-Evans cluster anion and synthesis under ambient conditions are the key factors that seem to be responsible for the aggregation of water molecules in cluster based solids. A close examination of results reported in literature (Table II.1) also suggested that Anderson-Evans cluster based solids synthesized under hydrothermal conditions were less hydrated as compared to those obtained via solvent evaporation technique.

When solution **A** consisting of sodium molybdate, chromium chloride and acetic acid was allowed to evaporate at room temperature, it resulted in the formation of **2** and **3.** The presence of acetic acid favored the formation of chromium acetate trinuclear complex which acted as a counter cation to the Anderson cluster anion, **2**. Since most of the chromium ions were utilized during the crystallization of **2**, the remaining Anderson anions aggregate along with sodium ions to form hydrated Anderson cluster, **3**.

II.3.4 Synthesis of Polypyrrole and Polypyrrole composite using Solids 1-3

Polypyrrole, a conductive polymer, has gained immense attention owing to its interesting properties and wide range of applications [30]. One of the simple and feasible methods for the synthesis of Polypyrrole (Ppy) is by chemical oxidative polymerization of pyrrole monomer. Various oxidizing agents like ferric chloride ($FeCl_3$), ammonium persulphate (APS), etc. are commonly used for polymerization [31]. Polyoxometalates, especially those containing molybdenum, have also been used in the synthesis of polymers or polymer composites since they can provide sufficient oxidizing medium for oxidative polymerization and can even form composite materials with the polymer [32]. Based on these considerations, Anderson cluster based solids **2** and **3** were examined for the formation of Polypyrrole and Polypyrrole composite through oxidative polymerization of pyrrole. Use of solid **1** was avoided as it already had an organic component incorporated in it which could hinder the polymerization process.

Ppy was successfully synthesized using APS in presence of Anderson cluster solid $[\{Cr_3(O)(CH_3COO)_6(H_2O)_3\}_2\{H_7CrMo_6O_{24}\}].24H_2O$, **2** as per the procedure described in Section II.2.2. FTIR spectrum showed bands characteristics of the pyrrole ring (refer Figure II.15a). The formation of polypyrrole was further confirmed from the PXRD patterns of the synthesized polymer. X-ray diffraction pattern of synthesized polypyrrole showed a broad peak at $2\theta=26°$, which is characteristic peak of amorphous polypyrrole [33] as observed in Figure II.15b. Polymerization of pyrrole was also carried out using

Solid **2** without APS and also using only APS as the oxidizing agent. In the later case polypyrrole was obtained, but the yield was very less when synthesis was carried out using only APS (i.e. in the absence of **2**). When solid **3** was used for polymerization of pyrrole, it resulted in the formation of Ppy along with traces of Anderson solid **3** which was confirmed from the PXRD pattern as shown in Figure II.16 indicating the formation of a composite material.

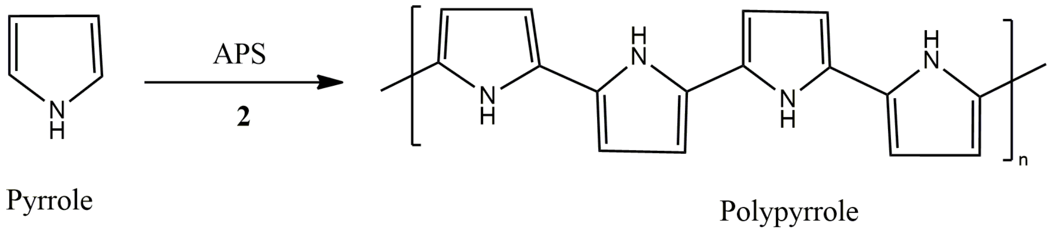

APS = $(NH_4)_2S_2O_8$

2 = $[\{Cr_3(O)(CH_3COO)_6(H_2O)_3\}_2\{H_7CrMo_6O_{24}\}]\cdot 24H_2O$

Scheme II.2 Formation of Polypyrrole using APS and solid **2.**

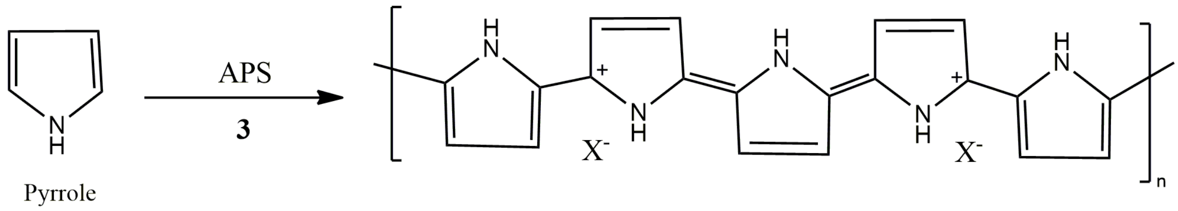

APS = $(NH_4)_2S_2O_8$

3 = $[Na\{Na(H_2O)_3\}_2\{H_6CrMo_6O_{24}\}]\cdot 2H_2O$

X = $\{H_6CrMo_6O_{24}\}$

Scheme II.3 Formation of Anderson-Polypyrrole composite using APS and solid **3.**

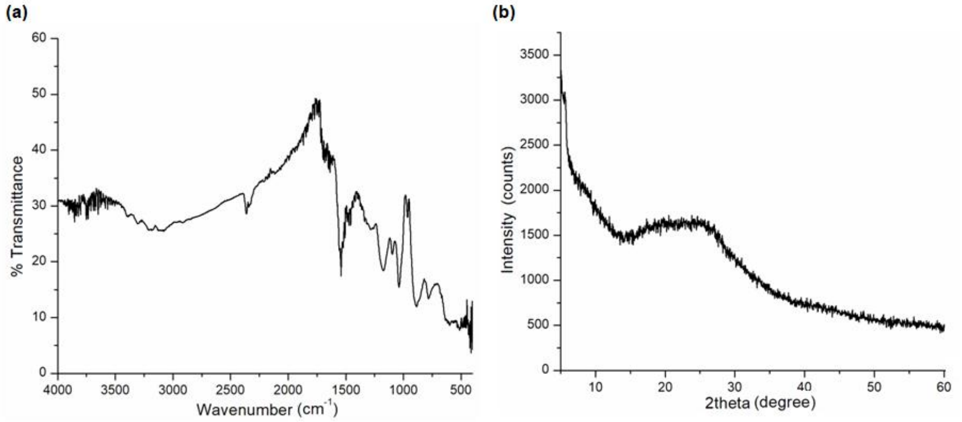

Figure II.15 (a) FTIR spectrum and (b) PXRD pattern of Polypyrrole synthesized using APS and Solid **2**.

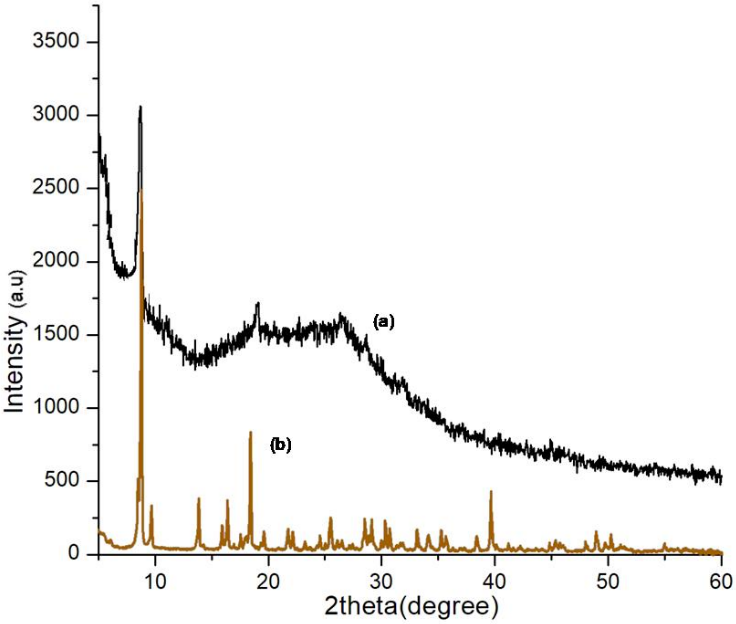

Figure II.16 (a) PXRD pattern of product synthesized using APS and solid **3**, (b) PXRD pattern of Anderson cluster, **3.**

II.4 Conclusions

Anderson-Evans type polyoxomolybdate solids **1-3** have been crystallized via solvent evaporation technique. Solvent evaporation technique offers a facile method for the synthesis of hybrid solids. Subtle changes in reaction parameters can affect the nature of molecular precursors in solution and offer alternative pathway for the crystallization of new phases. Detailed structural analysis revealed the role of supramolecular interactions in the crystal packing of solids. The hydrogen bonding interactions mediated by organic cations in **1** and by lattice water molecules in all the three solids plays a significant role in stabilizing the crystal packing. The ability of solids **2** and **3** for the synthesis of Polypyrrole and Polypyrrole composite using oxidative polymerization method was investigated. Anderson cluster based solids were found to be promising candidates for effective polymerization of pyrrole and for preparing polymer based composite materials.

References

1. Ariga K, Hill JP, Lee MV, Vinu A, Charvet R, Acharya S (2008) Sci Technol Adv Mater 9:014109
2. Lazzari M, Rodríguez-Abreu C, Rivas J, López-Quintela M (2006) J Nanosci Nanotechnol 6(4):892-905
3. Elemans JAAW, Rowan AE, Nolte RJM (2003) J Mater Chem 13:2661-2670
4. Misra A, Kozma K, Streb C, Nyman M (2020) Angew Chem Int Ed 59:596-612
5. Pradeep CP, Long DL, Cronin L (2010) Dalton Trans 39:9443-9457
6. Wang X, Vittal JJ (2003) Inorg Chem 42:5135-5142
7. Blazevic A, Rompel A (2016) Coord Chem Rev 307:42-64
8. Cindrić M, Veksli Z, Kamenar B (2009) Croat Chem Acta 82:345-362
9. Wu P, Wang Y, Huang B, Xiao Z (2021) Nanoscale 13:7119-7133
10. Ali Khan M, Shakoor Z, Akhtar T, Sajid M, Asif HM (2021) Inorg Chem Commun 133:108875
11. An H, Li Y, Xiao D, Wang E, Sun C (2006) Cryst Growth Des 6:1107-1112
12. Jin P, Wei H, Zhou L, Wei D, Wen Y, Zhao B, Wang X, Li B (2021) Mol Catal 510:111705
13. Boulmier A, Vacher A, Zang D, Yang S, Saad A, Marrot J, Oms O, Mialane P, Ledoux I, Ruhlmann L, Lorcy D, Dolbecq A (2018) Inorg Chem 57:3742-3752
14. Kumar D, Ahmad S, Prakash GV, Ramanujachary KV, Ramanan A (2014) Cryst Eng Comm 16:7097-7105
15. Yang YY, Song Y, Liu LY, Qu XS (2011) Acta Cryst E67:m776
16. Singh M, Kumar D, Ramanan A (2014) Proc Natl Acad Sci India Sect A Phys Sci 84:305-314
17. Ouahab L, Golhen S, Yoshida Y, Saito G (2003) J Clust Sci 14:193-204

18. Wang SM, Li YW, Feng XJ, Li YG, Wang EB (2010) Inorg Chim Acta 363:1556-1560
19. Wu XJ, Shen XM, Zhang P, Deng Q, Lü SZ, Cai TJ (2011) Z. Kristallogr New Cryst Struct 226:387
20. Peng ZS, Zhang CL, Shen XM, Deng Q, Cat TJ (2011) J Coord Chem 64:2848-2858
21. Yang YY, Song Y, Liu LY, Qu XS (2011) Acta Crystallogr Sect E Struct Rep Online 67(Pt 6):m776
22. Li XM, Guo Y, Shi T, Chen YG (2016) J Clust Sci 27:1913-1922
23. Pavani K: Transition metal complex templated polyoxomolybdates: synthesis, structure and magnetism. Indian Institute of Technology, Delhi, India (2007)
24. Bruker Analytical X-ray Systems (2000) SMART: Bruker Molecular Analysis Research Tool, Version 5.618
25. Bruker Analytical X-ray Systems (2000) SAINT-NT, Version 6.04
26. Bruker Analytical X-ray Systems (2014) SHELXTL
27. Klaus B, University of Bonn, Germany DIAMOND, Version 4.1
28. Brown ID, Altermatt D (1985) Acta Crystallogr B 41:244-247
29. Dewick PM (2006) Essentials of Organic Chemistry: For Students of Pharmacy, Medicinal Chemistry and Biological Chemistry, John Wiley & Sons Ltd, England
30. Hao L, Dong C, Zhang L, Zhu K, Yu D (2022) Polymers 14:5139
31. Zhang X, Zhang J, Song W, Liu Z (2006) J Phys Chem B 110:1158-1165
32. Gómez-Romero P, Casañ-Pastor N, Lira-Cantú M (1997) Solid State Ionics 101-103: 875-880
33. Chaluvaraju BV, Sangappa KG, Murugendrappa MV (2015) Polym Sci Ser A 57:467-472

Chapter III

Crystallization of Cobalt Based Hybrid Solids

Summary

In this chapter, two cobalt based pseudopolymorphs, *viz*. [Co(2-H*ampz*)$_2$Cl$_4$], **4** and [Co(2-*ampz*)$_4$Cl$_2$], **5** (Type IV hybrid solids), were synthesized using solvent evaporation method and characterized by SCXRD, FTIR, TGA and elemental analysis. It was observed that H-bonding and $\pi\cdot\cdot\pi$ interactions play a major role in the stabilization of crystal packing in both the solids. Therefore, three-dimensional Hirshfeld Surfaces and associated two-dimensional finger print plots have been performed to gain insight into these interactions. The classical electrostatic energy was found to be dominant in the crystal structures as indicated by the energy framework analysis. In addition, antibacterial potential of the solids was investigated and found to possess remarkable inhibitory activity towards various bacterial strains. Further, molecular docking studies were also performed with DNA gyrase as the target protein; the synthesized complexes, particularly solid **5** exhibited good binding affinity.

III.1 Introduction

Pseudopolymorphs are solids having same chemical entities but in varying stoichiometries for example {Cu(*pdz*)Cl_2} and {Cu(*pdz*)Cl}, wherein *pdz*: pyridazine [1,2]. As discussed in chapter II, subtle changes in the synthetic parameters influence the self-assembly process which may result in the formation of new phases. While investigating the role of reaction parameters that affect the self-assembly process in the formation of polyoxomolybdate hybrid solids, a heterocyclic ligand 2-aminopyrazine (2-*ampz*) was chosen as the organic precursor instead of pyrazole (pz) as discussed in Scheme II.1. It resulted in the crystallization of pseudopolymorphs *viz.* $[Co(2\text{-H}ampz)_2Cl_4]$, **4** and $[Co(2\text{-}ampz)_4Cl_2]$, **5**. Both **4** and **5**, belong to Type IV of hybrid solids i.e., metal complexes.

Coordination complexes, especially transition metal complexes, are well-known for exhibiting a variety of coordination numbers, geometries, oxidation states and ligand binding affinities [3,4]. They constitute an important class of hybrid solids owing to their versatile applications in the field of catalysis, photochemistry and pharmaceuticals [5,6]. In recent years, the use of transition metal complexes as therapeutic compounds has gained great significance; particularly, cobalt based bioactive solids have been explored extensively owing to their potential as antiviral, antibacterial and anti-inflammatory agents [7-12]. Selection of ligands used for the formation of transition metal complexes is also crucial. The synergetic effect of metal centers and ligands can enhance the activity of the complexes. For instance, pyrazine and its derivatives, especially aminopyrazines, form an important group of nitrogen containing heterocyclic compounds with antibacterial, antifungal, anti-inflammatory, anti-cancer and antioxidant activities [13-15].

Therefore, the work presented in this chapter is focused on the synthesis, characterization, crystal structure, Hirshfeld surface analysis and antibacterial studies of two cobalt based pseudopolymorphs with 2-*ampz* *viz.* [Co(2-H*ampz*)$_2$Cl$_4$], **4** and [Co(2-*ampz*)$_4$Cl$_2$], **5**. Molecular docking studies predict the biological activities of the compounds. Hence, the potential binding interactions between the synthesized solids and selected proteins were also investigated by molecular docking studies.

III.2 Experimental

III.2.1 Synthesis

Solids **4** and **5** were synthesized using solvent evaporation technique at room temperature. **4** was synthesized using similar a synthetic protocol as described in Section II.2.1 of Chapter **2**, using 2-aminopyrazine as ligand instead of pyrazole. The purple block like crystals of **4** were obtained after 4-5 weeks in 80% yield (based on Co). **5** was crystallized from Solution **B** consisting of $CoCl_2.2H_2O$ and 2-aminopyrazine in water/methanol in 82% yield (based on Co) as shown in Scheme III.1.

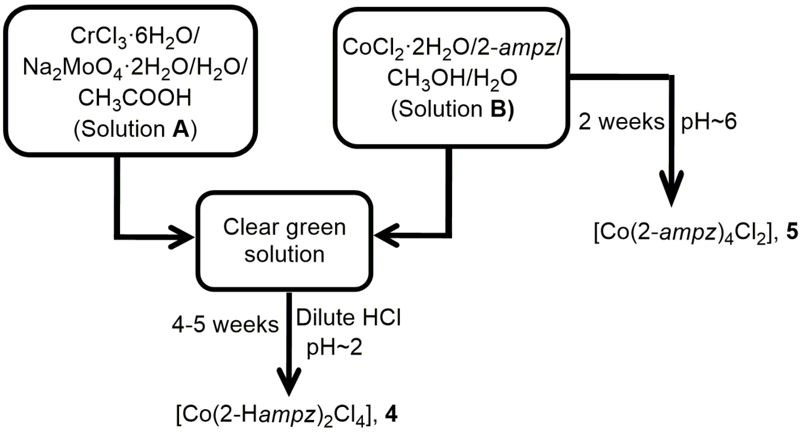

Scheme III.1 Scheme showing the synthetic pathway for the crystallization of **4** and **5**.

III.2.2 Characterization

The solids were characterized using single crystal X-ray diffraction, powder X-ray diffraction, fourier transform infrared spectroscopy and thermogravimetric analysis as discussed under Section II.2.3 in Chapter II. Crystal and refinement data have been summarized in Table III.1. Elemental analyses (C, H and N) were performed on ELEMENTAR Vario EL III CHNS Analyzer. Elem. Anal. Calcd. for **4**: C, 24.43; H, 3.05; N, 21.38. Found: C, 24.40; H, 3.03; N, 21.36%. For **5:** Calcd: C, 37.62; H, 3.91; N, 32.92. Found: C, 37.63; H, 3.92; N, 32.90%.

III.2.3 Magnetic susceptibility measurements

The magnetic susceptibilities of the solids were determined at room temperature using Guoy Balance (Sherwood, UK).

The magnetic moment and molar susceptibility are given by the following equations:

$$\text{Magnetic moment } (\mu) = 2.828 \sqrt{\chi_m \text{ x } T}$$

$$\chi_m = \chi_g \text{ x molecular weight}$$

$$\chi_g = \frac{C \text{ x } L \text{ x } (R-R_o)}{w \text{ x} 10^9}$$

where, C = Calibration constant

L = length of sample

W = weight of sample

R = sample reading

R_o = Empty tube reading

Table III.1 Crystal data and structure refinement parameters for **4** and **5**.

	4	**5**
Chemical formula	$C_8H_{12}Cl_4CoN_6$	$C_{16}H_{20}Cl_2CoN_{12}$
Molecular weight	392.97	510.27
Temperature (K)	296(2)	293(2)
Crystal system	Triclinic	Orthorhombic
Space Group	*P*-1	*P*ccn
a (Å)	7.1986(5)	7.6347(2)
b (Å)	7.3917(5)	15.7341(4)
c (Å)	7.8896(6)	18.6074(4)
α (°)	115.758(3)	90.00
β (°)	110.450(3)	90.00
γ (°)	96.904(3)	90.00
Volume (Å^3)	335.35(4)	2235.22(9)
Z	1	4
ρcalc (g·cm^{-3})	1.946	1.516
μ (mm^{-1})	2.069	1.038
F (000)	197	1044
Crystal size (mm)	0.42 x 0.35 x 0.23	0.30x 0.20x 0.15
Radiation	Mo Kα	Mo Kα
2Θ range for data collection (°)	6.362 to 56.534	3.2 to 27.5
Index ranges	$-9 \leq h \leq 9$, $-8 \leq k \leq 9$, $-10 \leq l \leq 10$	$-9 \leq h \leq 9$, $-20 \leq k \leq 20$, $-24 \leq l \leq 24$
Reflections collected	2582	2234
Independent reflections	1543 [Rint =0.0125]	2553[R_{int} = 0.024]
Data/restraints/parameters	1543/3/100	2553/4/157
Goodness-of-fit on F^2	0.899	1.057
$R[F^2 > 2\sigma(F^2)]$, $wR(F^2)$	0.0184, 0.0503	0.0250, 0.074

III.2.4 Hirshfeld surface analysis

Hirshfeld surface analysis represents a novel approach for visualization of molecular surfaces and for investigating intermolecular interactions in crystals. The Hirshfeld surface can be defined as the space occupied by a molecule in a crystal by partitioning the crystal electron density into molecular fragments and were named after F.L. Hirshfeld. Developed from Hirshfeld's idea of "stockholder partitioning" scheme for defining atoms in molecules, a weight function is defined for a molecule in a crystal by Spackman and Jayatilaka,

$$(\boldsymbol{r}) \; = \sum_{i \in \, molecule\ A} \rho_i{}^{at}(\boldsymbol{r}) \, / \sum_{i \in \, crystal} \rho_i{}^{at}(\boldsymbol{r})$$

$$= \rho_{promolecule}(\boldsymbol{r}) / \rho_{procrystal}(\boldsymbol{r})$$

where the numerator is a sum over the atoms in the molecule of interest (the promolecule) and the denominator is an analogous sum over the crystal (the procrystal). wA(r) is a continuous function with $0 < wA(r) < 1$. Hence, Hirshfeld surface is the region surrounding the molecule in the crystal where $wA(r) \geq 0.5$. It is the region where the ratio of promolecule contribution to the procrystal electron density exceeds from all other molecules in the crystal [16,17].

A van der Waals surface or an outer surface of the electron density also defines a volume around a molecule. But such molecular surfaces are defined only by the molecule itself, whereas the Hirshfeld surface is defined both by the molecule and its nearest neighbors, and hence can give information about intermolecular interactions. The presence of intermolecular interactions can be explained by mapping Hirshfeld surfaces on different properties viz., d_{norm}, d_i, d_e, molecular electrostatic potentials (MEP), curvedness and shape index. These properties can be analyzed using *Crystal Explorer* 21.5 software [18].

III.2.4.1 d_{norm}, d_e and d_i

d_{norm} is the normalized contact distance, defined in terms of d_e, d_i and the vdw radii of the atoms and mapped over red (distances shorter than sum of vdw radii) through white (distances equal to the sum of vdw radii) to blue (distances longer than sum of vdw radii) regions. 'd_{norm}' can be mathematically represented as [17]:

$$d_{norm} = \frac{(d_i - r_i^{vdw})}{r_i^{vdw}} + \frac{(d_e - r_e^{vdw})}{r_e^{vdw}}$$

where, d_e is the distance from a point on the surface to the nearest nucleus outside the surface and

d_i is the distance from a point on the surface to the nearest nucleus inside the surface;

r_i^{vdw} and r_e^{vdw} are the van der Waals radii of atoms present inside and outside the 3-D Hirshfeld surface

From the d_{norm} value, one can determine the regions involved in the intermolecular interactions in the crystals. d_i and d_e surfaces are viewed as red circular spots on each conformation and also consist of blue and green colored regions conveying the contact distances that are longer and equal to the sum of van der Waals radii. The nature of these two surfaces is also complementary to each other.

III.2.4.2 Shape index

Shape index is another interesting property of Hirshfeld surface that can represent the nature of self-complementary pairs in the crystal packing, where the two shapes differ only by a sign. Hence, it can be used to identify complementary hollows (red) and bumps (blue) where two molecular surfaces touch each other [17]. Shape index map is very sensitive to minute changes in the shape of a surface. Several small scattered yellowishred colored concave regions on them exhibits weak intermolecular interactions. Further, shape index also provides information on $\pi\cdots\pi$ interactions by the presence of red and blue colored triangular patches on surface of rings of the molecule [18,19].

III.2.4.3 Curvedness

Curvedness is a function of the root-mean-square curvature of the surface. The maps of curvedness typically show large regions of green (relatively flat) separated by dark blue edges (large positive curvature) [18]. Curvedness can be used to identify characteristic packing modes, especially planar stacking arrangements, and even the ways in which adjacent molecules contact one another. Relatively broad and flat regions on curvedness surface are characteristic of planar stacking of molecules [20]. Curvedness is a measure of ‘‘how much’’ shape, defined in terms of principal curvatures [21]. Areas on the Hirshfeld surface with a higher degree of curvedness tend to divide the surface into contact patches with each neighboring molecule; hence, the curvedness property could be used to define a coordination number in the crystal. Small yellow and red color spots may also be seen on the curvedness surface which indicates the presence of strong hydrogen bonding interactions.

III.2.4.4 Molecular electrostatic potentials (MEP)

Crystal Explorer can also generate electrostatic potential of the electron density mapped on the Hirshfeld surface. A clear insight about electrostatic interaction between neighboring molecules can be obtained which is indicated by red (electronegative) and blue (electropositive) regions on the electrostatic potential maps, while the white regions correspond to electrically neutral parts [22]. The electrostatic potentials were mapped on the Hirshfeld surface using the STO-3G basis set at the Hartree–Fock level of theory over the range ±0.1 au.

III.2.5 2-D finger print plots

2-D Finger print plot is a novel graphical method of representing the percentage contribution from various interatomic contacts in forming a 3-D Hirshfeld surface [23]. The graph is plotted using d_i and d_e distances on *x* and *y* axes respectively to represent the distance of any selected pair X and Y. These unique ‘finger print’ plots not only indicate which intermolecular interactions are present but also give the relative area of the surface corresponding to each kind of interaction. The contribution of each X···Y pair is represented by different colors; points with small contribution to the surface are colored blue, those with large contribution are indicated by colors ranging from green to red while the points with no contribution are left uncolored [23].

The molecular Hirshfeld surface analyses and their associated 2-D finger print plots (full and decomposed) were mapped employing the *Crystal Explorer* 21.5 program. The CIF files of the solids were given as input. The Hirshfeld surfaces were generated using a standard (high) surface resolution. The 2-D finger print plots were displayed using the expanded 0.6–2.8 Å range view with the d_i and d_e distance scales shown on the graph axes.

III.2.6 3-D Energy framework analysis

Energy frameworks provide a powerful and unique way of 3-D visualization of supramolecular aggregation of molecules in a crystal. Energy framework analysis by *Crystal Explorer* offers a better understanding of crystal packing by allowing calculation of various intermolecular interaction energies and a 3-D graphical representation of their magnitude [18]. The total interaction energy followed and used by Gavezzotti and others is [24]:

$$E_{tot} = E_{ele} + E_{pol} + E_{dis} + E_{rep}$$

which shows that the total energy framework is calculated by summing up of

E_{ele} classical electrostatic energy

E_{pol} polarization energy

E_{dis} dispersion energy

E_{rep} repulsion energy

This method was also extended to transition-metal coordination compounds as reported by Maloney *et al.* [25]. The interaction energies are calculated using molecular pair-wise interaction and are represented as cylinders joining the centroids of pairs of molecules. The radius of the cylinder is proportional to the magnitude of interaction energy.

The energy framework calculations were carried out using *Crystal Explorer* 21.5 software with HF energy model and 3-21G basis set by generating a molecular cluster around 3.8Å.

III.2.7 Antimicrobial studies

The determination of antibiotic susceptibility of a pathogen is important in selecting the most appropriate one for treating a disease. The *in vitro* screening of the antibacterial activities of the ligand, 2-aminopyrazine and its two Co(II) complexes were carried out using Kirby-Bauer Disc Method.

The Kirby-Bauer Disc Method is also called the agar diffusion method or the disk diffusion method [26]. In this method, a filter disk impregnated with an antibiotic is applied to the surface of an agar plate containing the organism to be tested and the plate is incubated at 37°C for 24-48 hours. As the substance diffuses from the filter paper into the agar, the concentration decreases as a function of the square of the distance of diffusion. At some particular distance from each disk, the antibiotic is diluted to the point that it no longer inhibits microbial growth. The effectiveness of a particular antibiotic is shown by the presence of growth-inhibition zones. These zones of inhibition (ZOIs) appear as clear areas surrounding the disk from which the substances with antimicrobial activity diffused. The diameter of the ZOI can be measured with a ruler and the results of such an experiment constitute an antibiogram. The agar diffusion method uses commercially available filter paper disks, each containing a defined concentration of a specific antibiotic. The relative effectiveness of different antibiotics provides the basis for a sensitivity spectrum of the organism.

III.2.6.1 Materials required

Sterile petriplates, Nutrient broth, MHA agar, Antibiotic discs (gentamycin), cultures of *Escherichia coli* (*E.Coli*), *Staphylococcus saprophyticus, Bacillus subtilis* and *Pseudomonas fluorescence.*

III.2.6.2 Procedure

The sterilized molten agar of bearable warmth was poured into the petridish and left to cool and solidified. A sterile swab was dipped into the broth cultures in excess moisture by pressing the swab against the side of the tube. Swab the surface of agar completely. Then the plates were turned 90 degrees and repeated swabbing. Ran the swab around the circumference of the plate and allowed the surface to dry for about 5 minutes before placing antibiotic disc on agar. Cut wells (10mm diameter and about 2 cm apart) in each of these plates using sterile cork borer. The samples were prepared by dissolving it in DMSO (1mg/ml) and added into the wells and allowed to diffuse at room temperature. Disc with DMSO but without samples were used as the control. The standard discs were placed aseptically with sterile forceps on the agar surface. Lightly touch each disc with sterile forceps to make sure that it is in good contact with agar surface. The inoculated petri dishes were incubated upside down at 35°C. After incubation for overnight, the ZOI was measured using a ruler at the widest diameter from one edge of the zone to the other edge. The disc diameter is reported in millimeters, looked upon the standardized chart and the result is reported as sensitive (S), resistant (R) or intermediate (I).

III.2.7 Molecular docking

Molecular docking is a computational technique used in the field of computational chemistry and drug discovery to predict the binding orientation and affinity of a small molecule (ligand) to a macromolecule (receptor), usually a protein [27].

Molecular docking typically involves three main steps: preparation of the ligand and receptor structures, generation of multiple conformations of the ligand and receptor, and scoring of the resulting conformations to identify the most likely binding mode. Various algorithms and scoring functions are used to evaluate the interactions between the ligand and receptor and to predict the binding affinity of the ligand for the receptor. The goal is to identify the optimal orientation of the ligand within the receptor, which maximizes the number of favorable interactions (such as hydrogen bonding, electrostatic interactions, and van der Waals forces) and minimizes any unfavorable interactions. Molecular docking is also used to understand the mechanism of action of drugs at the molecular level.

In silico docking studies were performed using Autodock 4.2 version [28] and the images were rendered using Biovia Discovery Studio Visualizer 2018 [29]. The crystal structures of the target enzyme/protein, DNA gyrase of *E.Coli* (PDB ID: 1AJ6) and *Bacillus subtilis* (PDB ID: 4DDQ) were obtained from the RCSB protein data bank in pdb format. The 3-D structure of the ligand 2-aminopyrazine (*2-ampz*) was downloaded from PubChem (https://pubchem.ncbi.nlm.nih.gov/compound/2-Aminopyrazine) and converted to pdb format using *Open Babel* software. The CIF files of the metal complexes were also converted to pdb using *Open Babel.* Before docking, there was a pre-treatment process for both the proteins and the ligands. The protein preparation was done by removing the native ligands and water molecules, followed by addition of missed hydrogen atoms. 2-*ampz* and its Co(II) complexes were also prepared for docking by adding hydrogen atoms and energy minimization was carried out using force field in Autodock. Grid maps were generated using Auto Grid programme. Lamarckian genetic Algorithm (LGA) was employed as docking algoritham and all the docking parameters were set to default [30]. The structure with the lowest binding free energy was chosen for the optimum docking conformation.

III.3 Results and Discussion

III.3.1 Crystal Structure of 4 and 5

III.3.1.1 Crystal Structure of [Co(2-H*ampz*)$_2$Cl$_4$], 4

Crystal structure analysis of **4** showed that [Co(2-H*ampz*)$_2$Cl$_4$] is centro-symmetric with the metal atom at the centre of an octahedron formed by four chlorine atoms and a nitrogen atom from each of the two 2-H*ampz* molecules (Figure III.1). While, Co–N bond distance is 2.1822(11) Å; the Co–Cl bond distance was found to be 2.4583(4) and 2.4645(4) Å. Each [Co(2-H*ampz*)$_2$Cl$_4$] complex is connected to neighboring complexes through H-bonding interactions between the chloride ions and N–H groups of 2-*ampz* ligands to form 1-D chain (Table III.2). Each of these chains is connected through H-bonding interactions to two others to form a 2-D sheet (Figure III.2). Each sheet is connected to two others through π–π stacking (3.406(3) Å) between 2-H*ampz* moieties of neighboring sheets (Figure III.3). Detailed structural analysis revealed that **4** is isostructural to [Fe(2-H*ampz*)$_2$Cl$_4$] reported by Rusbridge *et. al.*[31]. Interestingly, it is also the new pseudopolymorph of [Co(2-*ampz*)$_4$Cl$_2$], **5** [32] which will be discussed in detail in Section III.3.1.2. Unlike in [Co(2-*ampz*)$_4$Cl$_2$], one of the azine nitrogen atoms in

4 is protonated. Interestingly, this protonation seems to be the key factor for the crystallization of the new pseudopolymorph [Co(2-H*ampz*)$_2$Cl$_4$].

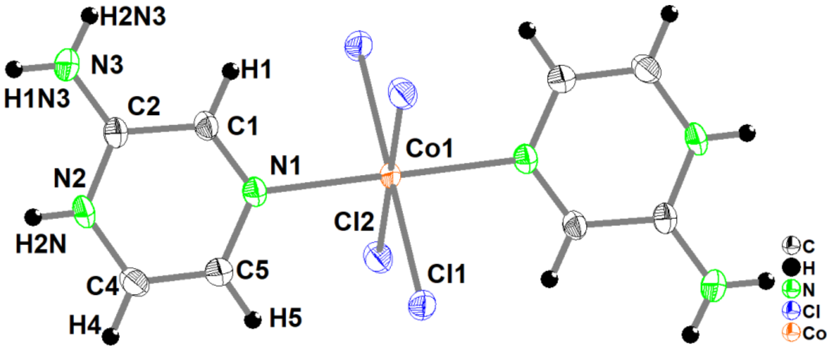

Figure III.1 ORTEP diagram of **4**. Non hydrogen atoms are shown as 50% ellipsoids and hydrogen atoms as arbitrary spheres.

Table III.2 H-bonding interactions in **4**.

D-H...A	**D-H (Å)**	**H...A (Å)**	**D...A (Å)**	**∠ D-H...A (°)**
N2-H3…Cl2	0.860(3)	2.617(4)	3.260(6)	132.52(8)
N3-H2A…Cl1	0.860(3)	2.638(4)	3.301(6)	134.82(9)
N3-H2B…Cl1	0.860(2)	2.322(5)	3.175(7)	171.65(9)

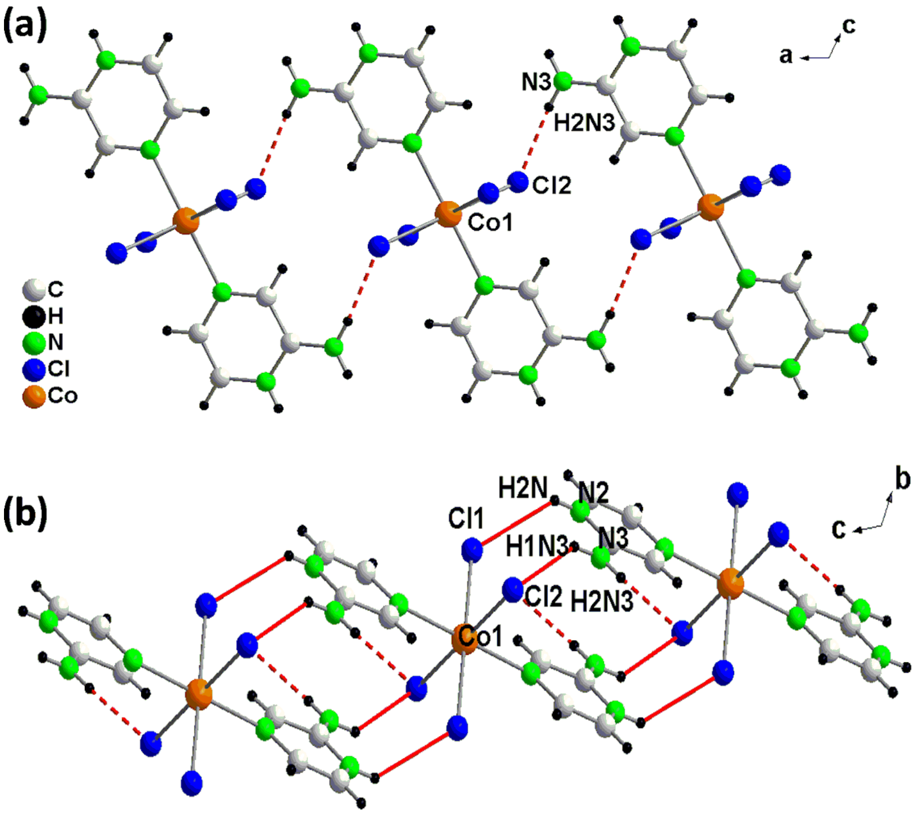

Figure III.2 (a) H···Cl interactions shown in dashed red lines link complex moieties to form 1-D chains propagating along *a* axis. (b) Inter-chain H···Cl interactions shown in solid red lines connect neighboring chains to form 2-D sheet.

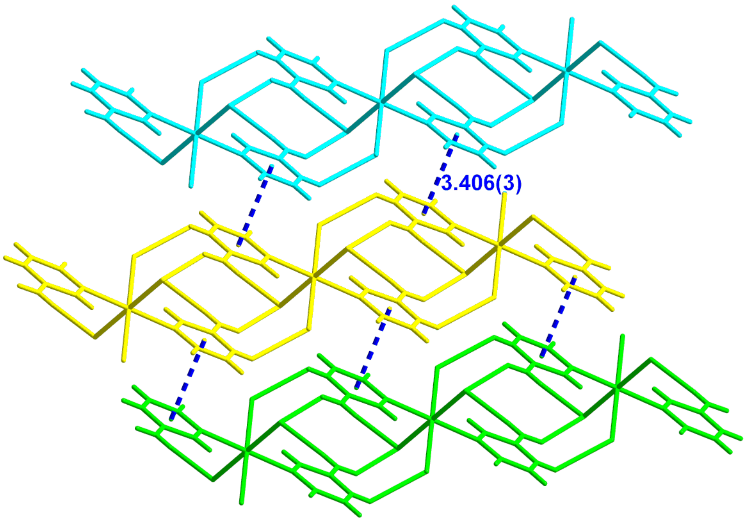

Figure III.3 Figure showing three sheets (depicted in cyan, yellow and green colors) connected to each other through π-π stacking.

III.3.1.2 Crystal structure of [Co(2-*ampz*)$_4$Cl$_2$], 5

Crystal structure of [Co(2-*ampz*)$_4$Cl$_2$] consists of Co^{2+} ion at the centre of the octahedron formed by four 2-*ampz* moieties and two chlorine atoms as shown in Figure III.4. The Co-Cl bond distance was found to be 2.421(0)Å, whereas the Co-N1 and Co-N4 bond distances being 2.207(1)Å and 2.194(1)Å respectively. Adjacent [Co(2-*ampz*)$_4$Cl$_2$] units are connected by N-H···Cl hydrogen bonding interactions of 2-*ampz* ligands to form 1-D zig-zag chains (Figure III.5a). Details of H-bonding interactions are given in Table III.3. Each 1-D chains are further connected to form 2-D sheets as shown in Figure III.5b. Intermolecular H-bonding interactions further connect the sheets to form 3-D network (Figure III.6).

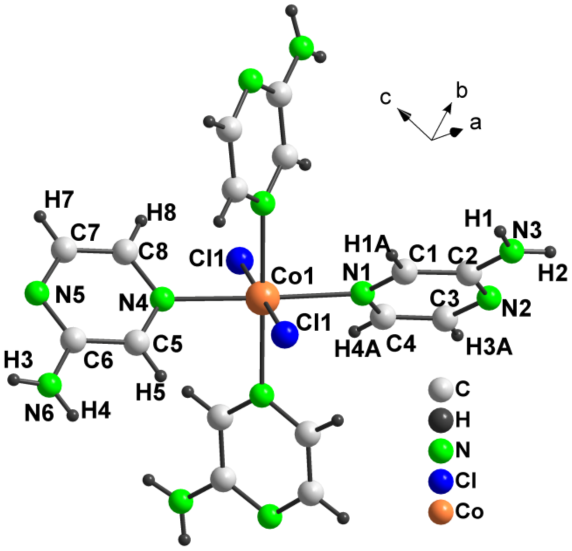

Figure III.4 Crystal structure of **5**.

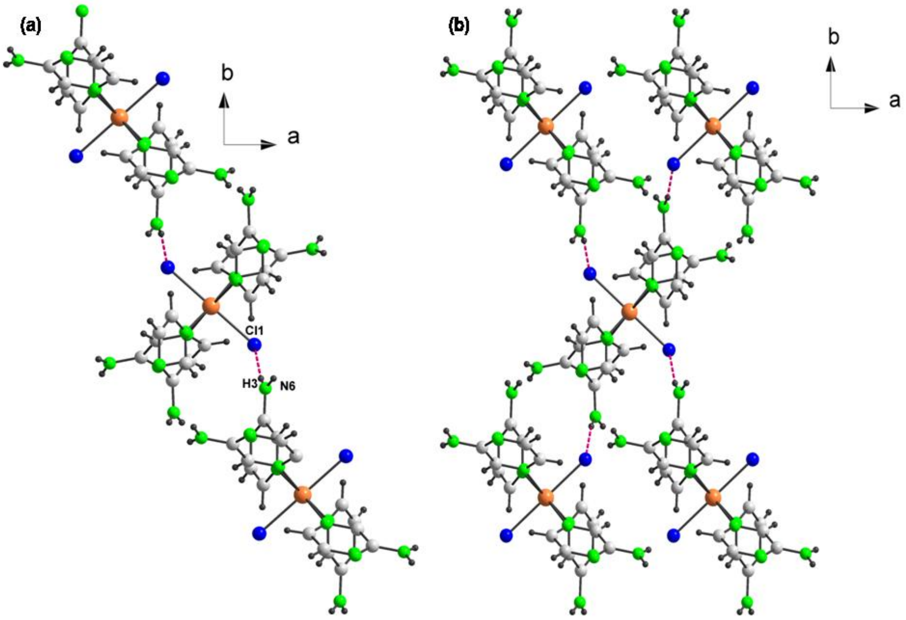

Figure III.5 (a) N-H···Cl interactions (shown in red dashed lines) leading to 1-D zig-zag chains in **5**. (b) Intermolecular H-bonding interactions connect neighboring chains to form 2-D sheets.

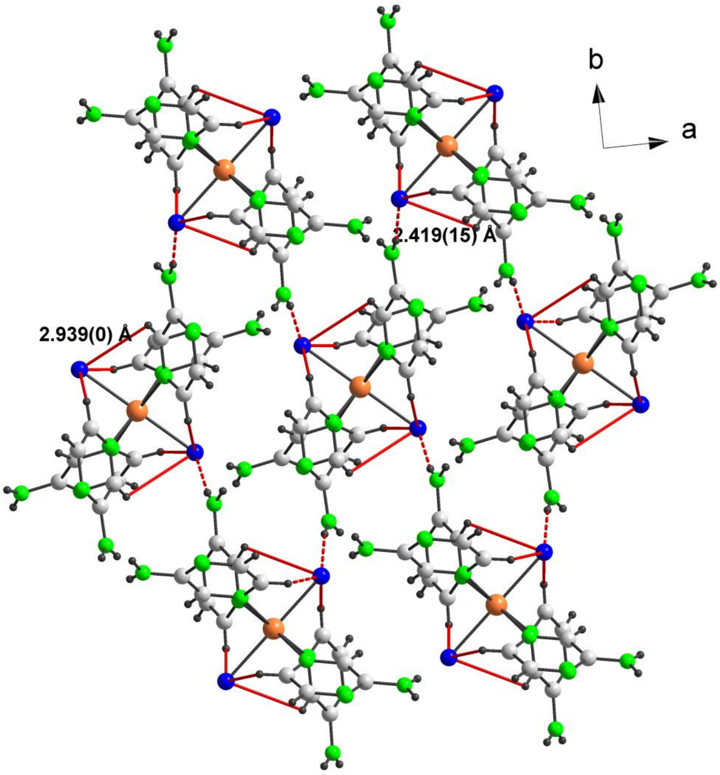

Figure III.6 Inter and intra molecular H-bonding further connects the sheets to form 3-D network. Intramolecular H-bonding is shown in solid red lines.

Table III.3 H-bonding interactions in **5**.

D-H...A	**D-H (Å)**	**H...A (Å)**	**D...A (Å)**	**∠ D-H...A (°)**
N3—H1···Cl1	0.85 (1)	2.36 (1)	3.209 (2)	175 (2)
N3—H2···N5	0.86 (1)	2.43 (2)	3.134 (2)	140 (2)
N6—H3···Cl1	0.85 (1)	2.42 (1)	3.265 (1)	171 (2)
N6—H4···N2	0.86 (1)	2.33 (2)	3.045 (2)	142 (2)

III.3.2 Vibrational and Thermal analyses

The FTIR spectra of **4** and **5** (Figure III.7) displayed bands in the region 3300-300 cm^{-1} due to N-H stretching vibrations of the 2-aminopyrazine ligand. The strong peaks in the range 1650- 1530 cm^{-1} could be attributed to N-H bending vibrations. A medium intensity band due to the C-N stretching was observed at around 1200 cm^{-1}. The low frequency region of the spectra indicated the presence of a medium intensity band at around 420 cm^{-1} in **4** and 428 cm^{-1} in **5** due to Co-Cl vibrations.

Figure III.8 shows the TG plots of **4** and **5**. TG analysis of **4** showed weight loss in two steps; an initial weight loss of 49.2% upto 360°C corresponding to the loss of two 2-*ampz* moieties (calcd. 48.3%). The second weight loss of 37.4% upto 690°C was observed in **4** corresponding to the loss of four chloride units (calcd. 36.1%). The residual 13.4% could be attributed to cobalt metal. On the other hand, in **5**, the first weight loss upto 370°C corresponding to 75% was due to the degradation of four 2-*ampz* moieties (calcd. 74.5%). Subsequent weight loss of 14% upto 700°C could be assigned to the loss of two chloride units (calcd. 13.9%). The remaining 11% could be attributed to cobalt metal.

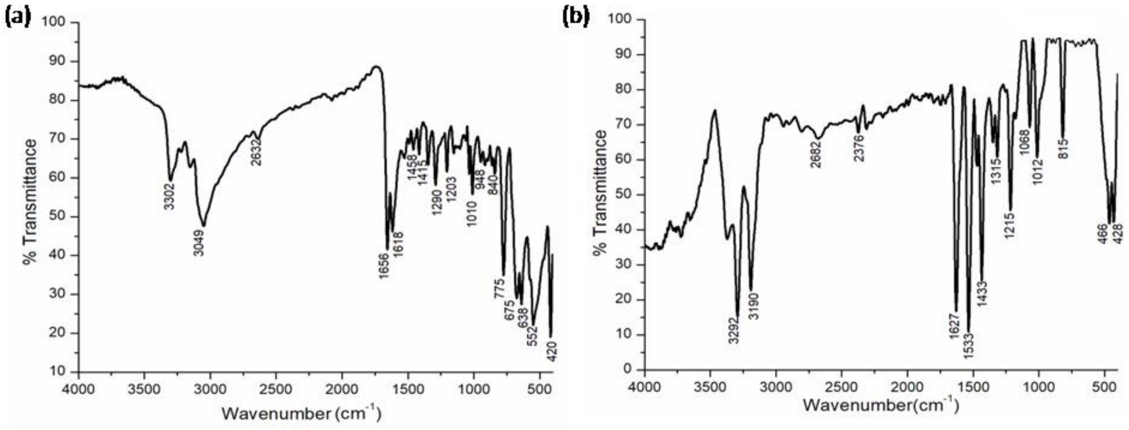

Figure III.7 FTIR spectrum of (a) **4** and (b) **5**.

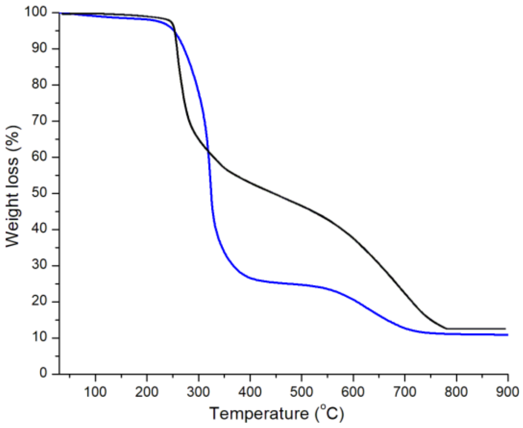

Figure III.8 TG plots of **4** (black) and **5** (blue).

III.3.3 Hirshfeld surface analyses

The Hirshfeld surface of **4** cover 309.80 Å² area and spread over 328.40 Å³ volumes with 0.5 isovalue. The 3-D “d_{norm}” surfaces were mapped (along *c* axis) over a fixed color scale of -0.484 to 0.949 Å, d_i ranging from 0.790 to 2.397 Å, d_e in the color scale of 0.790 to 2.398 Å, whereas, shape index mapped within the color range of -1.000 to 1.000 Å, and curvedness in the range of -4.000 to 0.400 Å respectively (along *b* axis), as shown in Figure III.9. The surfaces are shown transparent to permit visualization of the crystal structure.

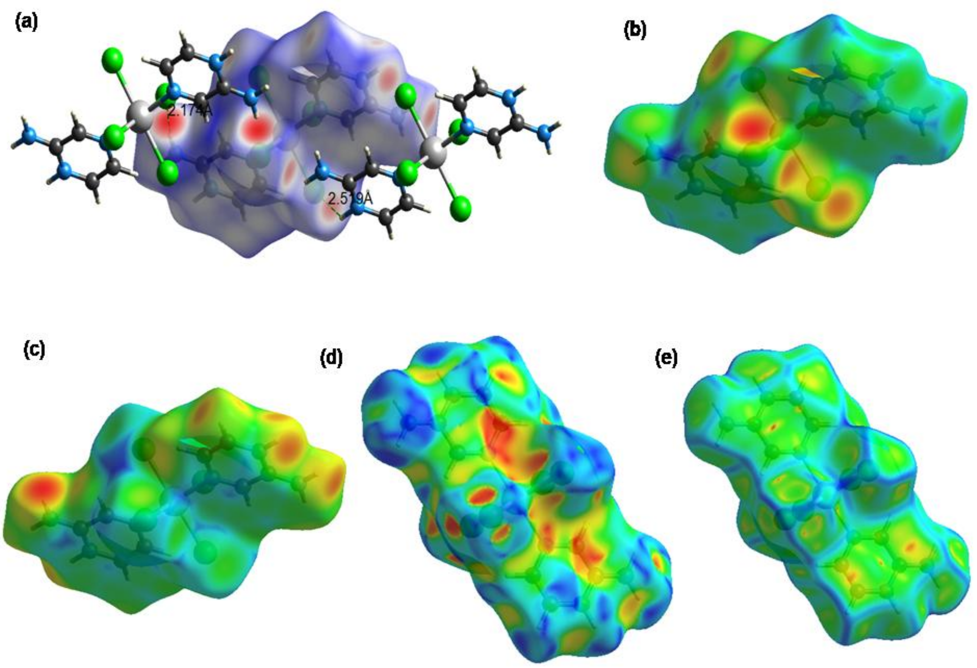

Figure III.9 Hirshfeld surfaces for visualizing the intermolecular contacts in **4** (a) d_{norm} highlighting the regions of N—H···Cl hydrogen bonds, (b) d_e, (c) d_i, (d) shape index and (e) curvedness.

The red spots inside the contours on shape index map indicate intermolecular interactions as given in Table III.3. The appearance of consecutive red and blue triangular patches over the aromatic ring in the shape index map (Figure III.9d) confirms the presence of weak π···π interactions in the crystal packing.

The large flat regions delineated by a blue outline on the curvedness map (Figure III.9e) shows the planar stacking of molecules [17].

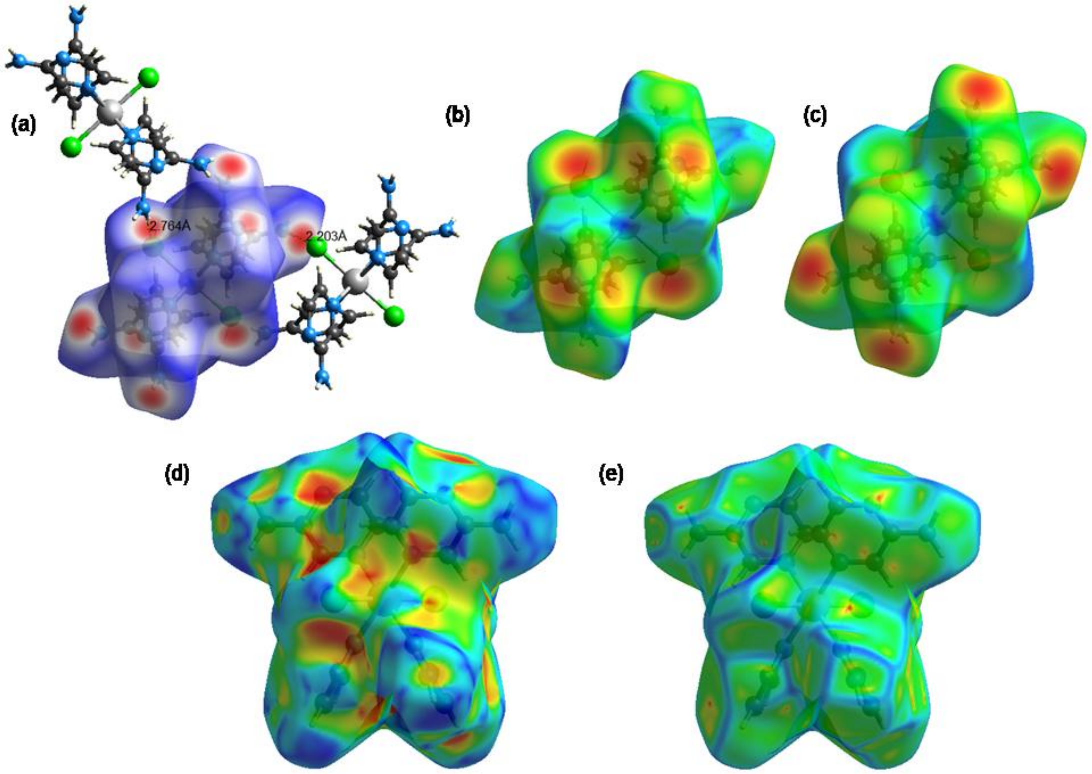

Figure III.10 Hirshfeld surfaces for visualizing the intermolecular contacts in **5** (a) dnorm highlighting the regions of N—H···Cl hydrogen bonds, (b) d_e, (c) d_i, (d) shape index and (e) curvedness (along *b* axis).

The Hirshfeld surface of **5** spread over 444.03 Å^2 area and holds 548.96 Å^3 volume with 0.5 isovalue; the scaled color patches on the surface were generated in the range -0.454 to 1.180Å, 0.810 to 2.660Å, 0.811 to 2.610 Å for d_{norm}, d_i and d_e respectively, whereas the shape index plot and curvedness plot are engendered from -1.00 to 1.00 a.u. and -4.000 to 0.400 a.u., respectively, as shown in Figure III.10. As discussed in the Hirshfeld surface (HS) of **4**, red circular spots on the Hirshfeld surface of **5** indicate intermolecular close contacts of N-H···Cl hydrogen bonding interactions as shown in Figure III.10a. Shape index map and curvedness map shows the characteristic features of weak π···π stacking interactions in the crystal structure of **5** (Figures III.10d and 10e).

III.3.3.1 Molecular electrostatic potentials (MEP)

The electrostatic potential maps reveal the electropositive regions represented by blue color and electronegative regions represented by red color in the molecules as shown in Figure III.11. In **4,** red color regions can be seen near the chlorine atoms corresponding to highly electrostatic negative acceptor potential whereas in **5** electronegative spots indicated by red color can be seen around chlorine atoms and also nitrogen atoms in the aromatic ring.

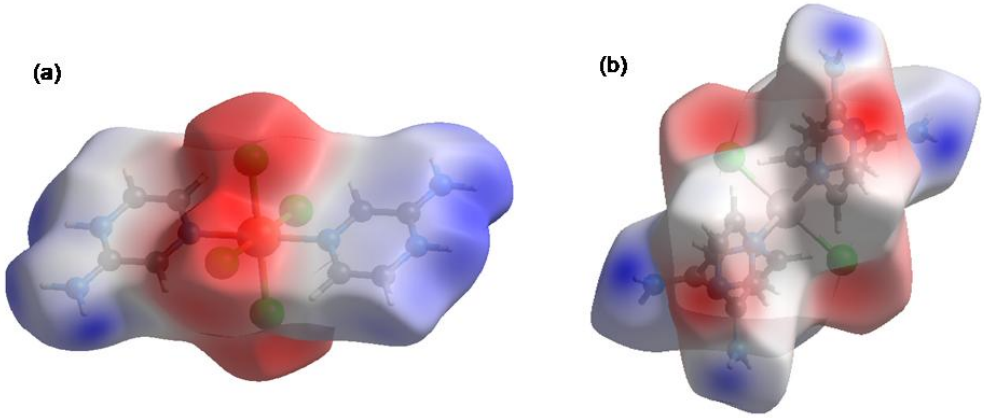

Figure III.11 Electrostatic potential mapped on the Hirshfeld surface of (a) **4** and (b) **5**.

III.3.3.2 Finger print plots

The 2-D finger print plots for overall and individual interactions in the crystal packing of solids **4** and **5** were calculated and results are shown in Figures III.12 and III.13 respectively.

In **4,** the major contribution to the HS area is due to H···Cl/Cl···H contacts (51.2%). H···Cl/Cl···H contacts can be attributed to N-H···Cl hydrogen bonding interactions and appear as two sharp symmetric spikes in the finger print plots of **4** (refer Figure III.12b). The second major contact is H···H, since it has a contribution of 22% to the total surface area (Figure III.12c). The C···H, N···H contacts also have significant contributions to the HS in **4** as can be seen in the 2-D plots.

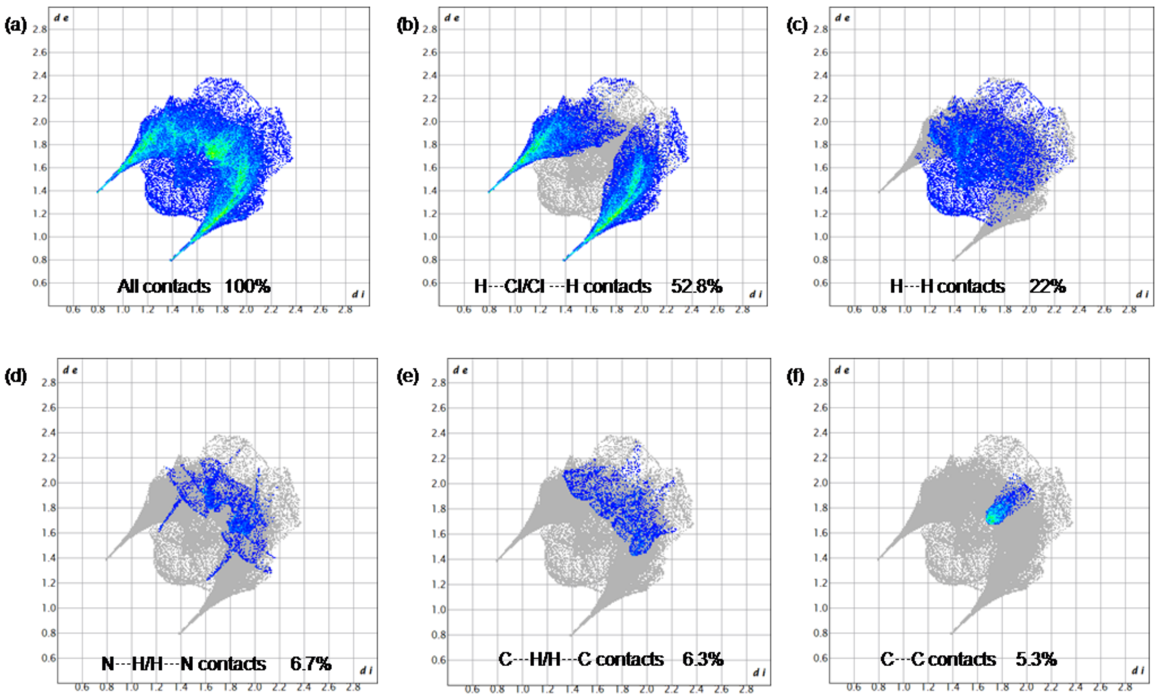

Figure III.12 2-D finger print plots of solid **4** showing the contributions of different types of interactions: (a) all intermolecular contacts, (b) H···Cl/Cl···H contacts, (c) H···H contacts, (d) N···H/H···N contacts, (e) C···H/H···C contacts and (f) C···C contacts. The outline of the full finger print is shown in grey.

Finger print plots revealed that H···Cl interactions plays a major role in the stabilization of crystal packing in **4**. However, in **5**, the H···H interactions are the most abundant contributing to 42.9% to the total Hirshfeld surface area as shown in Figure III.13b, followed by N···H interactions (23.8%) characterized by two sharp symmetric spikes at d_e+d_i~2.6Å (Figure III.13d). This is due to the abundance of H and N on the molecular surface of solid **5** arising from four 2-aminopyrazine moieties in the unit cell. H···Cl interactions also contribute significantly (15.7%) to the HS appearing as two prominent long spikes at d_e+d_i~2.8Å as shown in Figure III.13c. In addition, as can be seen in Figure III.13e, the C···H contacts contribute 12.9% to the Hirshfeld surface characterized by two symmetric wings in the FP plot.

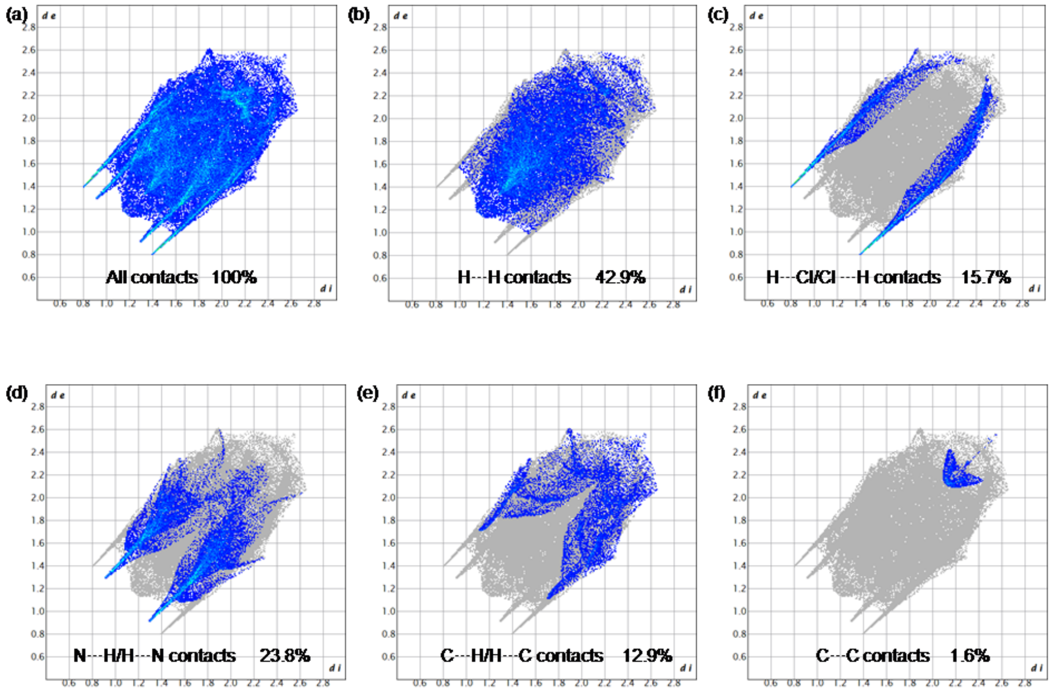

Figure III.13 2-D finger print plots of solid **5** showing the contributions of different types of interactions: (a) all intermolecular contacts, (b) H···H contacts, (c) H···Cl/Cl···H contacts, (d) N···H/H···N contacts, (e) C···H/H···C contacts and (f) C···C contacts. The outline of the full finger print is shown in grey.

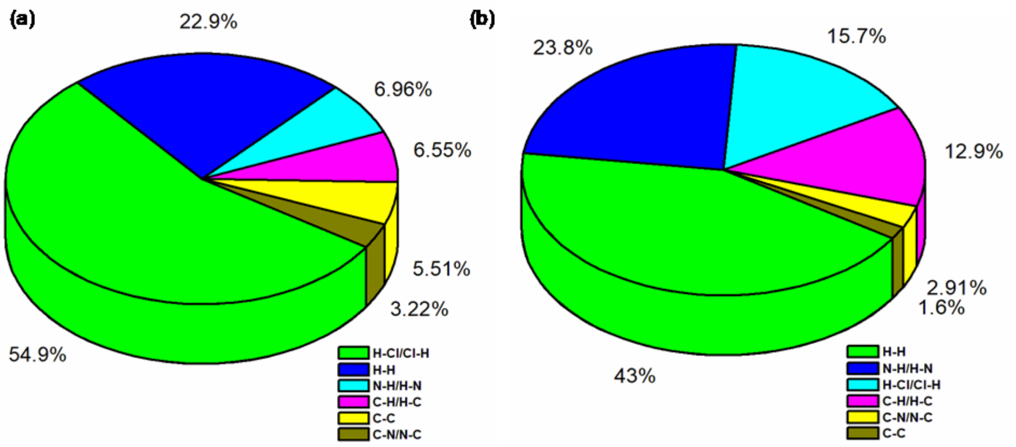

Figure III.14 Graphical representation of the contribution of interatomic contacts in the crystal packing of (a) **4** and (b) **5**.

III.3.4 Energy framework analysis

The various intermolecular interaction energies were computed for solids **4** and **5** by 3-D energy frameworks using the default red, green and blue colored solid cylinders in the construction of Columbic or classical electrostatic E_{ele}, dispersion E_{dis} and total energy components E_{tot}, respectively. The molecular pairs involved in the calculation of interaction energies for **4** and **5** are shown in Figures III.15.

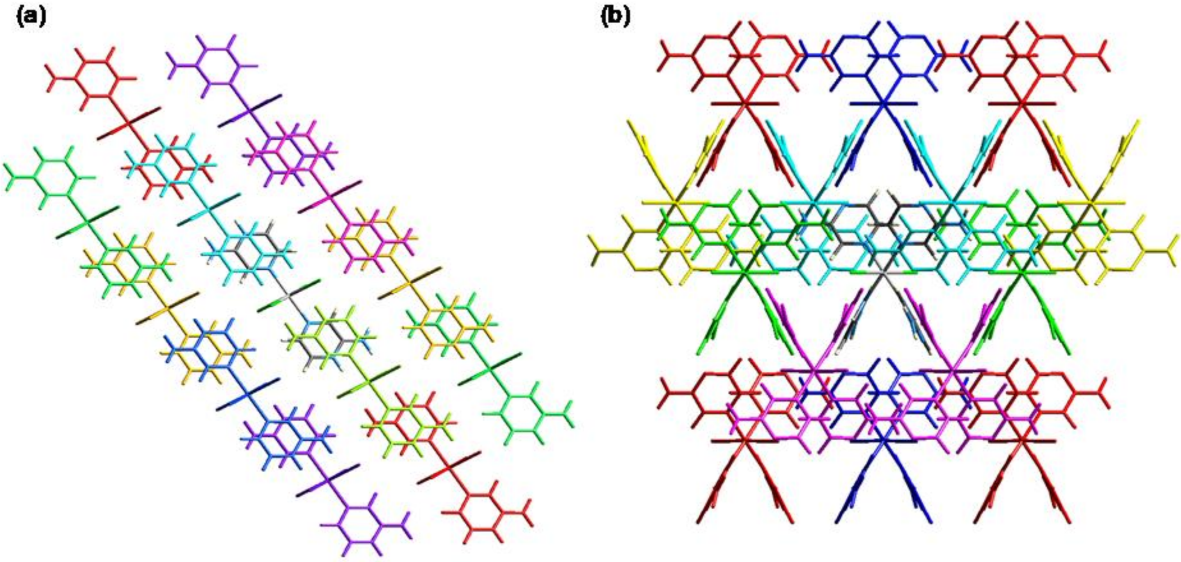

Figure III.15 Molecular pairs involved in the interaction of (a) **4** and (b) **5**.

3-D energy frameworks corresponding to coulomb energy (red), dispersion energy (green) and total energy (blue) along the crystallographic axis is displayed in Figures III.16 and III.17 for solids **4** and **5** respectively.

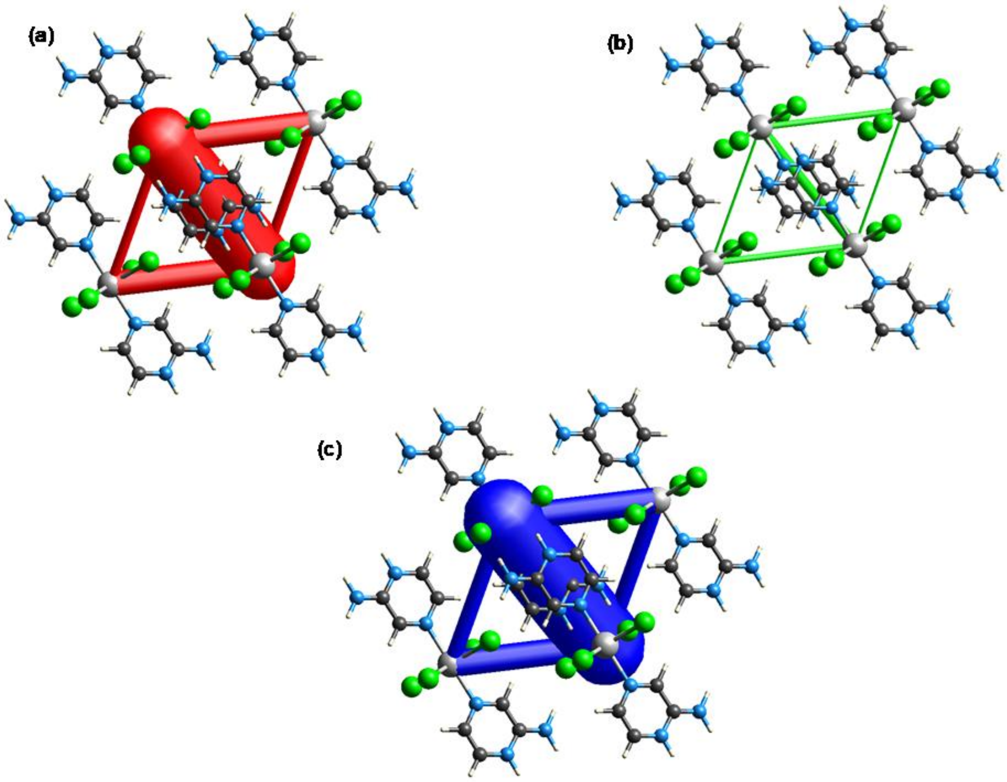

Figure III.16 Energy framework diagrams for a cluster of molecules in **4:** (a) electrostatic or Coulomb energy, E_{ele}; (b) dispersion energy, E_{dis} **(c)** total energy, E_{tot}. The cylindrical radius was adjusted to the scale factor of 80 kJ mol^{-1} with a cut-off value of 10 kJ mol^{-1}. Weak molecular interactions below threshold energy value of 10 kJ mol^{-1} were omitted for clarity.

As discussed in section III.2.6, the thickness of the cylinders in each energy framework corresponds to the strength of the interaction energies between respective molecular pairs which were also confirmed by the higher negative energy values as shown in Tables III.4 and III.5. The tables provide information on various interaction energies and total energies based on a color code scheme of molecular pairs interacting. In addition, other information can be obtained from the table, such as the existence of rotational symmetry operations with respect to the reference molecule (*Symop*), the centroid-to-centroid distance in Å between the reference molecule and interacting molecules (*R*) and the number of pair(s) of interacting molecules with respect to the reference molecule (*N*), which helps in the calculation of lattice energy of a crystal [33].

Table III.4 Interaction Energies (kJ/mol) in component form of **4**.

$$\mathbf{E_{tot} = E_{ele} \times k_{ele} + E_{pol} \times k_{pol} + E_{dis} \times k_{dis} + E_{rep} \times k_{rep}}$$

Color code	N	Symop	R	Electron Density	E_{ele}	E_{pol}	E_{dis}	E_{rep}	E_{tot}
🟥	2	x, y, z	15.01	HF/3-21G	0.0	-7.3	0.0	0.0	-4.7
🟧	2	x, y, z	7.20	HF/3-21G	-114.4	-90.0	-35.2	103.6	-122.7
🟩	2	x, y, z	8.10	HF/3-21G	-326.9	-117.3	-66.8	96.5	-391.4
🟩	2	x, y, z	13.79	HF/3-21G	0.0	-3.5	0.0	0.0	-2.2
🟦	2	x, y, z	8.62	HF/3-21G	-317.3	-112.8	-56.7	94.7	-371.0
🟦	2	x, y, z	8.14	HF/3-21G	-40.9	-30.7	-16.7	23.4	-57.8
🟪	2	x, y, z	12.72	HF/3-21G	0.0	-6.9	0.0	0.0	-4.5
🟪	2	x, y, z	7.89	HF/3-21G	-47.5	-35.6	-15.1	14.0	-73.8

Scale factors for benchmarked energy models

Energy Model	k_{ele}	k_{pol}	k_{disp}	k_{rep}
CE-HF ... HF/3-21G electron densities	1.019	0.651	0.901	0.811
CE-B3LYP ... B3LYP/6-31G(d,p) electron densities	1.057	0.740	0.871	0.618

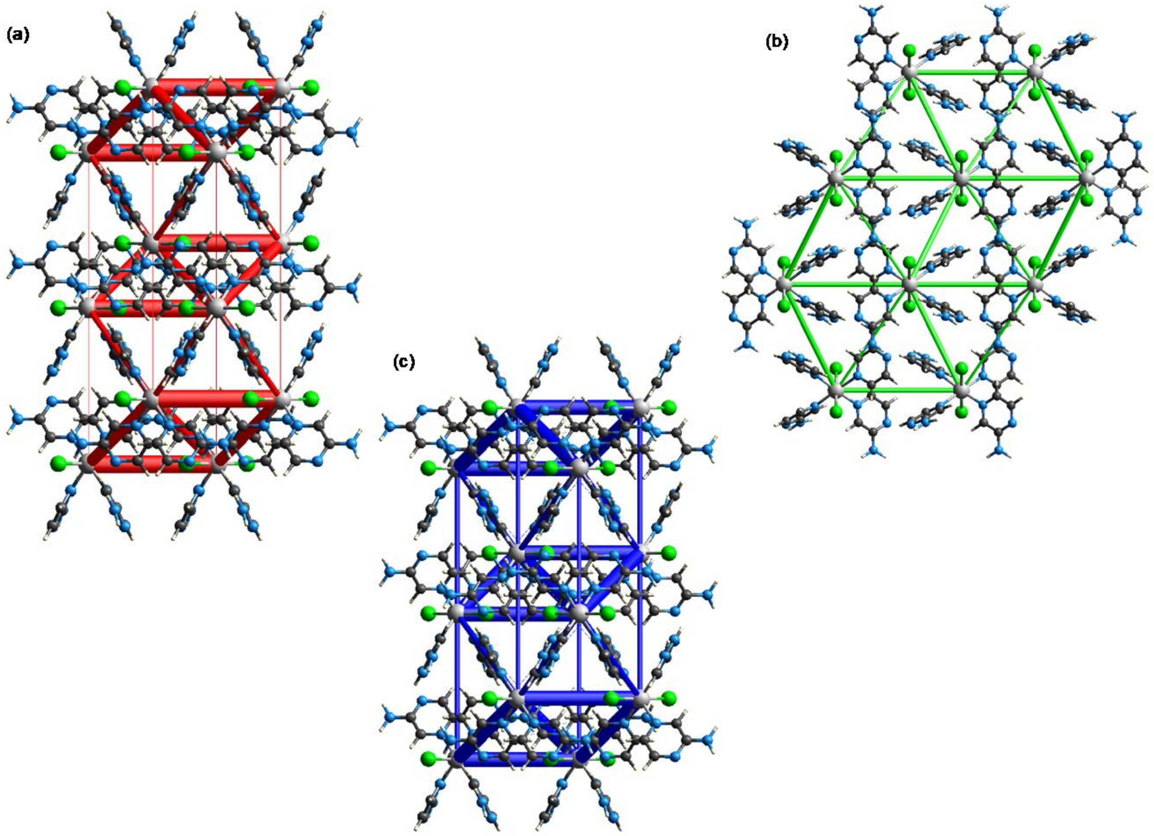

Figure III.17 Energy framework diagrams for a cluster of molecules in **5**: (a) electrostatic or Coulomb energy, E_{ele}; (b) dispersion energy, E_{dis} **(c)** total energy, E_{tot}. The cylindrical radius was adjusted to the scale factor of 80 kJ mol^{-1} with a cut-off value of 10 kJ mol^{-1}. Weak molecular interactions below threshold energy value of 10 kJ mol^{-1} were omitted for clarity.

$k_{el}e$, k_{dis}, k_{pol} and k_{rep} are the conversion factors for calculation of total energies which are reported only for two benchmarked energy models of electron density functions CE-HF…HF/3-21G and CE-B3LYP…B3LYP/6-31G(d,p), scaled appropriately and are displayed just below the tables III.4 and III.5 [34].

Table III.5 Interaction Energies (kJ/mol) in component form of **5.**

Color code	N	Symop	R	Electron Density	E_{ele}	E_{pol}	E_{dis}	E_{rep}	E_{tot}
🟥	4	-x+1/2, y, z+1/2	12.04	HF/3-21G	0.0	-3.7	0.0	0.0	-2.4
🟨	2	-x, -y, -z	14.43	HF/3-21G	0.0	-0.4	0.0	0.0	-0.2
🟩	2	x, y, z	7.63	HF/3-21G	-104.3	-35.6	-42.5	91.6	-93.5
🟦	2	-x, -y, -z	9.57	HF/3-21G	-70.7	-15.6	-44.1	38.4	-90.8
🟦	2	-x+1/2, y, z+1/2	9.30	HF/3-21G	-4.5	-2.0	-39.7	13.7	-30.5
🟪	4	x+1/2, -y, -z+1/2	10.28	HF/3-21G	-36.6	-12.8	-23.6	36.0	-37.7

Scale factors for benchmarked energy models

Energy Model	k_{ele}	k_{pol}	k_{disp}	k_{rep}
CE-HF ... HF/3-21G electron densities	1.019	0.651	0.901	0.811
CE-B3LYP ... B3LYP/6-31G(d,p) electron densities	1.057	0.740	0.871	0.618

The highest total interaction energy obtained was, E_{tot} = -391.4 kJ/mol in solid **4** at the molecular centroid distance R = 8.10Å (refer Table III.4). In **5,** the highest total interaction energy obtained was E_{tot} = -93.5kJ/mol as can be seen in table III.5.

An overall analysis of energy frameworks of **4** and **5** show that the major contribution towards the interaction energies comes from classical electrostatic or coulomb energy followed by dispersion energy. From the energy framework diagrams (Figures III.16 and III.17) and the interaction energy tables (tables III.4 and III.5), it can be inferred that classical electrostatic/Coulomb energy, E_{ele} dominates over the dispersion energy, E_{dis} frameworks in both solids **4** and **5.**

III.3.5 Antibacterial activities

Solids **4, 5**, ligand **(**2-aminopyrazine) and cobalt chloride were screened for their antibacterial activity against four different bacterial strains; two-gram positive bacteria: *Staphylococcus saprophyticus, Bacillus subtilis* and two gram negative bacteria*: E. Coli, Pseudomonas fluorescence.* Gentamycin was used as the standard. The solvent (DMSO) was used as the control. The results are shown in Figure III.18. The calculated zone of inhibition is listed in Table III.6

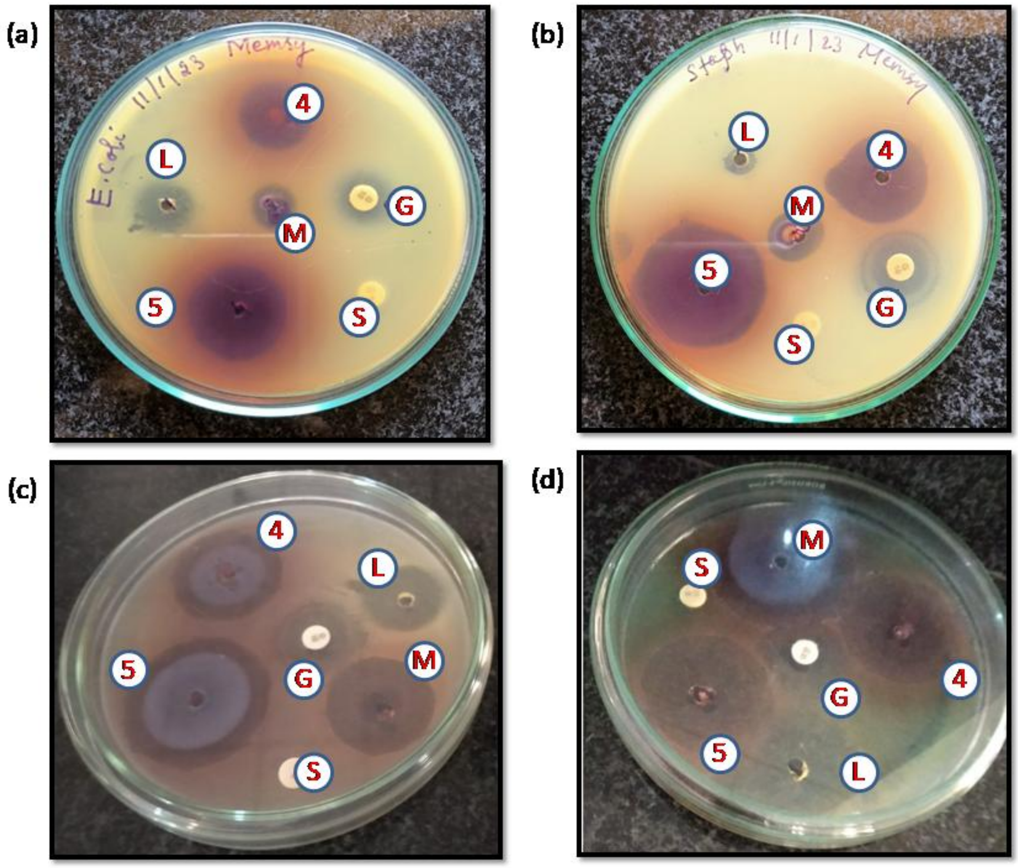

Figure III.18 Anti bacterial activity of solids **4** and **5** compared with 2-*ampz*, cobalt chloride and standard antibiotic Gentamycin (S-solvent, L-2-*ampz*, M-cobalt chloride, G-Gentamycin); (a) *Escherichia Coli*, (b) *Staphylococcus saprophyticus*, (c) *Bacillus subtilis* and (d) *Pseudomonas fluorescence.*

Table III.6 Anti bacterial activity (zone of inhibition) against clinical pathogens.

Microorganism	**Zone of inhibition (mm)**				
	4	**5**	2-*ampz*	$CoCl_2.6H_2O$	Standard (Gentamycin)
E.Coli	19	25	12	10	15
Staphylococcus saprophyticus	22	32	14	16	20
Bacillus subtilis	25	38	20	23	18
Pseudomonas fluorescence	32	36	28	26	16
Solvent-DMSO	No activity				

From the anti bacterial studies, it was observed that **4** and **5** showed higher activities than the free ligand 2-*ampz* and metal chloride, $CoCl_2.6H_2O$. Both solids showed higher activities when compared with the standard Gentamycin towards both gram-positive and gram-negative bacteria. Solid **5** was particularly more sensitive than solid **4** towards all bacterial strains. The greater sensitivity of **5** could be attributed to the presence of four 2-*ampz* moieties in the structure in contrast to two 2-*ampz* units in **4.**

The higher activity of metal complexes when compared to ligand can be explained on the basis of Tweedy’s chelation theory [35,36]. Chelation reduces the polarity of the metal ion due to partial sharing of the positive charge with the donor atom of the ligand and also due to delocalization of π-electrons over the chelate ring. This decrease in the polarity enhances the lipophilic nature of the complexes, which makes it easier to penetrate the cell walls of microorganisms thus interfering with the normal cell processes.

III.3.6 Molecular docking studies

In order to better understand the antibacterial potentials of **4** and **5,** molecular docking studies were carried out using DNA gyrase present in *E.Coli* (PDB ID: 1AJ6) and *Bacillus Subtilis* (PDB ID: 4DDQ) as the protein target. The DNA gyrase enzyme, a subclass of Topoisomerase II, is an attractive target due to its presence in all microbes. It plays a significant role in DNA replication and catalyses the ATP-dependent negative super-coiling of double-stranded closed-circular DNA [37].

The negative values of the binding free energy of the docked complexes (refer Table III.7) indicated that the complexes reasonably bind to the DNA gyrase. 2-*ampz* and solids **4** and **5** interact with the target enzyme mainly through H-bonding and Vander Waals interactions.

Table III.7 Interaction of 2-*ampz*, **4** and **5** with protein targets, 1AJ6 and 4DDQ.

Compound	**1AJ6**		**4DDQ**	
	Interacting residues (H-bonding)	**B.E (kcal/mol)**	**Interacting residues (H-bonding)**	**B.E (kcal/mol)**
2-*ampz*	GLY77, ARG76, GLU50	-3.8	VAL38, ARG39	-3.59
4	VAL118, VAL97, ASN46, ASP49	-5.06	PHE479, ASP481, MET102, VAL104	-3.65
5	ALA100, ILE94, ASP45, ASN46	-5.70	ASP297, ARG298, ARG484, ASP96, PRO219, LEU264, ALA221	-6.37

The binding energies of 2-*ampz*, **4** and **5** with 1AJ6 were found to be -3.8, -5.06 and -5.70 kcal/mol respectively. With 4DDQ, binding energies were -3.59, -3.65 and -6.37 kcal/mol for 2-*ampz*, **4** and **5** respectively. In this analysis, **5** showed relatively high negative binding energies, indicating its greater affinity towards DNA gyrase. Strong H-bonding interactions could be the reason for the enhanced activity of **5** than **4**. The results were in good agreement with the wet lab experiments. The docking results with DNA gyrase present in *E.Coli* and *Bacillus Subtilis* are represented in figures III.19 and III.20 respectively.

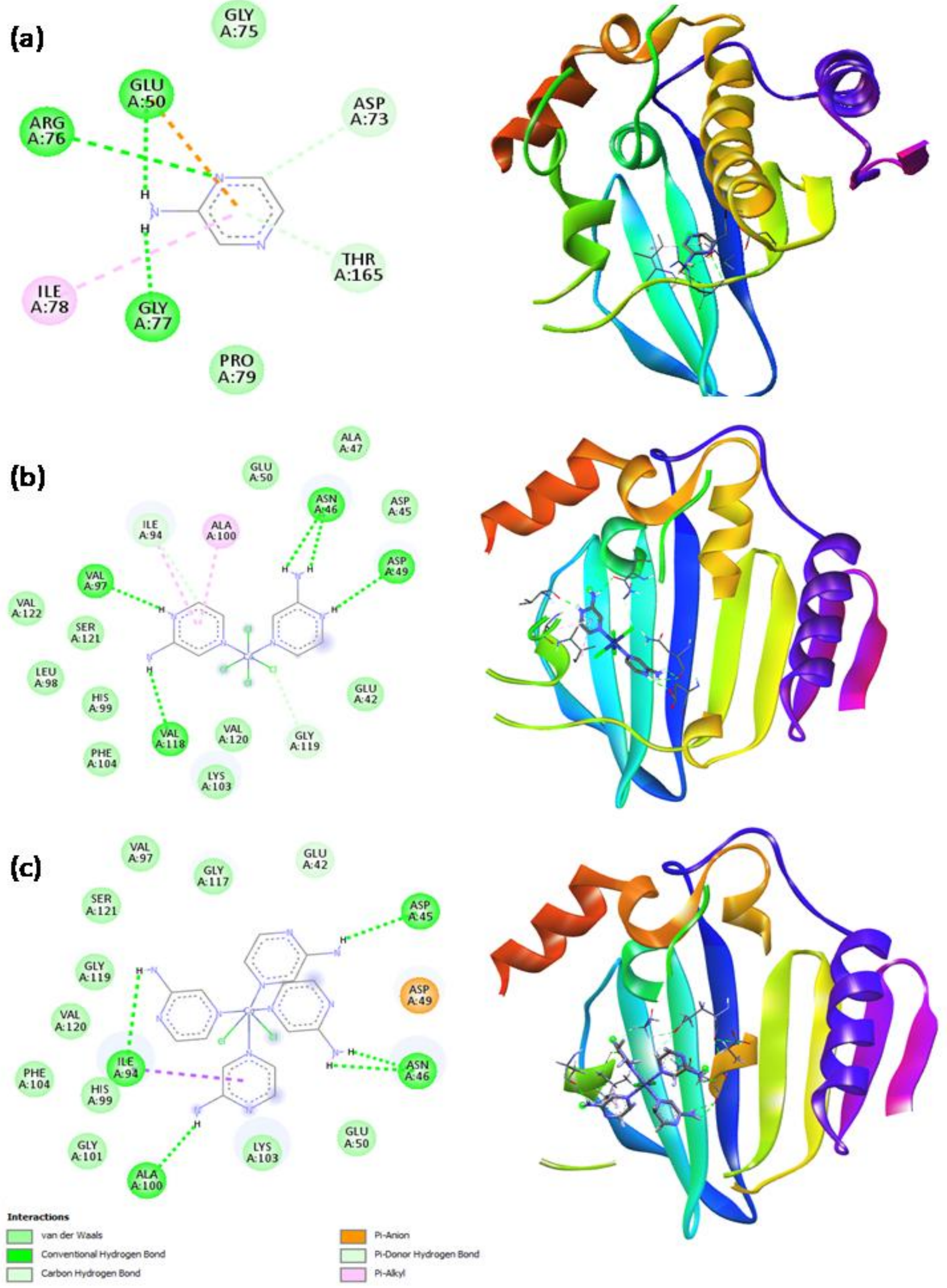

Figure III.19 Molecular docking of (a) 2-*ampz*, (b) **4** and (c) **5** with the target protein PDB ID: 1AJ6. Left and right hand images represent 2-D and 3-D interaction diagrams respectively.

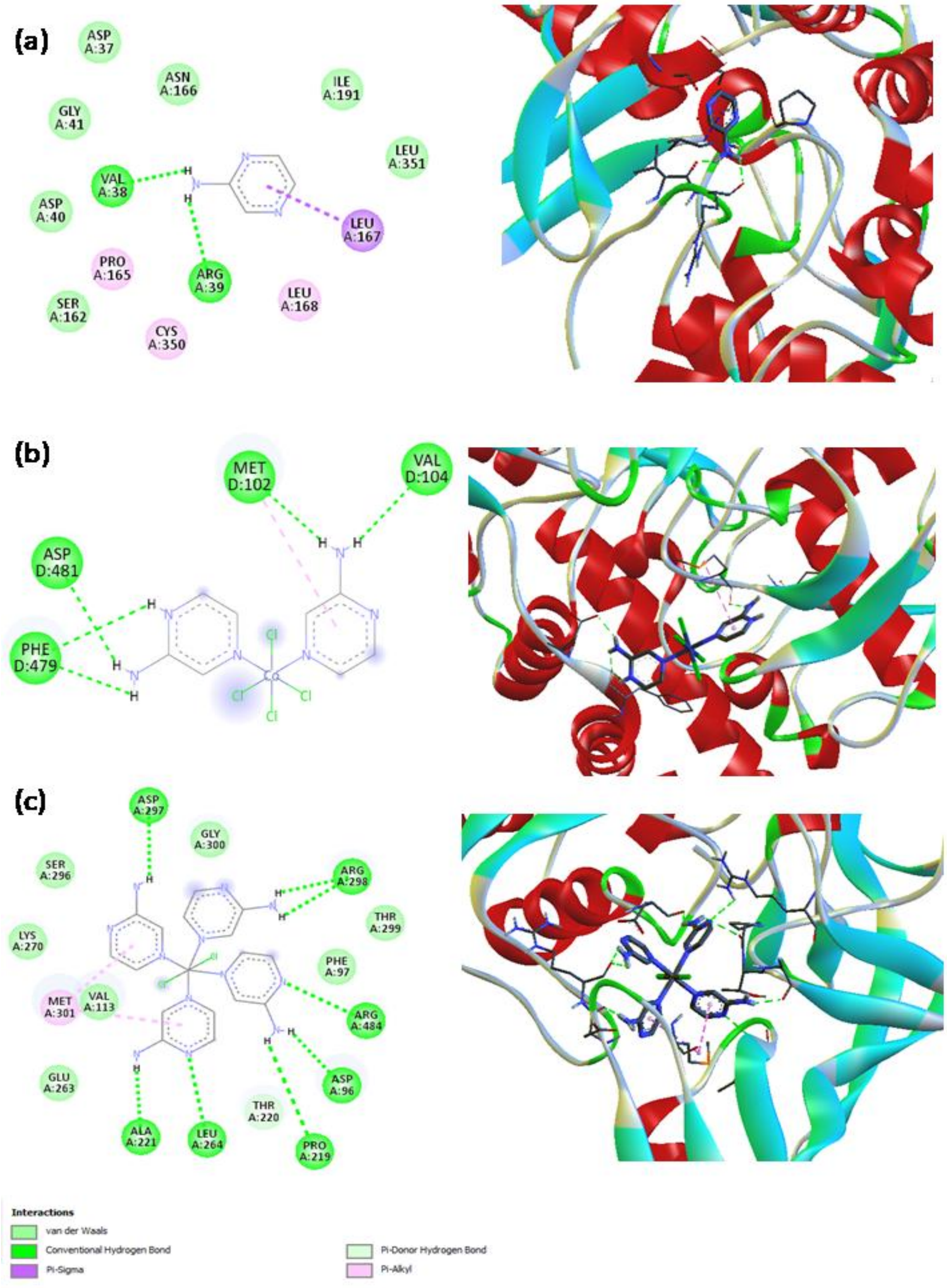

Figure III.20 Molecular docking of (a) 2-*ampz*, (b) **4** and (c) **5** with the target protein PDB ID: 4DDQ. Left and right hand images represent 2-D and 3-D interaction diagrams respectively.

III.3.8 Magnetic properties

For solids **4-5**, the magnetic moment was calculated using spin only formula, $\mu = [n(n+2)]^{1/2}$ BM (where n is number of unpaired electrons).

In solids **4-5**, only one cobalt center is present and the observed magnetic moment obtained was 4.61 and 5.83 BM respectively. The calculated magnetic moment using spin only formula is 3.80. Therefore, the observed value showed a deviation from the calculated values which indicated that other parameters seem to be affect the magnetic behavior of these two solids.

III.4 Conclusions

Two cobalt based pseudopolymorphs with 2-*ampz viz.* $[Co(2\text{-H}\mathit{ampz})_2Cl_4]$, **4** and $[Co(2\text{-}\mathit{ampz})_4Cl_2]$, **5** were synthesized using solvent evaporation method and characterized by SCXRD, FTIR, TGA and elemental analysis. The role of non-covalent interactions that stabilize the crystal packing was investigated in detail using Hirshfeld surface analyses, finger print plots and energy framework analysis. The metal complexes **4** and **5** showed significant antibacterial activities when compared with the ligand, 2-*ampz* and with the standard antibiotic Gentamycin. **5** exhibited greater sensitivity towards all bacterial strains. Molecular docking studies were carried out to substantiate the *in vitro* antibacterial studies and also to find out the best binding site of the complexes with the target protein. From the *in vitro* and *in silico* studies it can be concluded that the synthesized Co(II) complexes can be promising novel antimicrobial agents.

References

1. Nangia A, Desiraju GR (1999) Chem Commun 7:605-606

2. Thomas J, Ramanan A (2016) J Chem Sci 128:1687-1694

3. Elgrishi N, Chambers M B, Wang X, Fontecave M (2017) Chem Soc Rev 46:761-796

4. Wagenknechta P S, Ford P C (2011) Coord Chem Rev 255:591-616

5. Warra AA (2011) J Chem Pharm Res 3(4):951-958.

6. Haas KL, Franz KJ (2009) Chem Rev 109:4921-4960

7. Schwartz JA, Lium EK, Silverstein SJ (2001) J Virol 75:4117-4128

8. Chang EL, Simmers C, Knight DA (2010) Pharmaceuticals 3:1711-1728

9. Dimiza F, Papadopoulos AN, Tangoulis V, Psycharis V, Raptopoulou CP, Kessissoglou DP, Psomas G (2010) Dalton Trans 39:4517-4528

10. Dimiza F, Papadopoulos AN, Tangoulis V, Psycharis V, Raptopoulou CP, Kessissoglou DP, Psomas G J (2012) Inorg Biochem 107:54-64.

11. Patel M, Chhasatia M, Bhatt B (2011) Med Chem Res 20:220-230.

12. Sathyadevi P, Krishnamoorthy P, Alagesan M, Thanigaimani K, Thomas Muthiah P, Dharmaraj N (2012) Polyhedron 31:294-306

13. Ferreira SB, Kaiser CR (2012) Expert Opin Ther Pat 22:1033-1051

14. El-Emary T (2006) J Chin Chem Soc 53:391-401

15. Hamada M, Roy V, McBrayer TR, Whitaker T, Urbina-Blanco C, Nolan SP, Balzarini J, Snoeck R, Andrei G, Schinazi RF, Agrofoglio LA (2013) Eur J Med Chem 67:398-408

16. Hirshfeld FL (1977) Theoret Chim Acta 44:129-138

17. Spackman MA, Jayatilaka D (2009) Cryst Eng Comm 11:19-32

18. Spackman PR, Turner MJ, McKinnon JJ, Wolff SK, Grimwood DJ, Jayatilaka D, Spackman MA (2021) J Appl Cryst 54:1006-1011

19. R.A. Ayten (2019) Acta Crystallogr E75:1467-1471
20. Gumus I, Solmaz U, Binzet G, Keskin E, Arslan B, Arslan H (2018) J Mol Struct 1157:78-88
21. Chopra D (2018) Understanding intermolecular interactions in the solid state: Approaches and techniques (Vol. 26), Royal Society of Chemistry, UK
22. Spackman MA, McKinnon JJ, Jayatilaka D (2008) Cryst Eng Comm 10:377-388
23. Spackman MA, McKinnon JJ (2002) Cryst Eng Comm 4:378-392
24. Gavezzotti A (2002) J Phys Chem B 106 (16):4145-4154
25. Maloney AGP, Wood PA, Parsons S (2015) Cryst Eng Comm 17:9300-9310
26. Murray PR, Baron EJ, Pfaller MA, Tenover FC, Yolken HR (1995) Manual of Clinical Microbiology, 6th Ed. ASM Press, Washington DC
27. Meng XY, Zhang HX, Mezei M, Cui M (2011) Curr Comput Aided Drug Des 7(2):146-157
28. Morris GM, Huey R, Lindstrom W, Sanner MF, Belew KR, Goodsell DS, Olson AJ (2009) J Comput Chem 16:2785-2791
29. http://accelrys.com/products/discovery-studio/visualization-download.php
30. Morris GM, Goodsell DS, Halliday RS, Huey R, Hart WE, Belew KR, Olson AJ (1999) J Comput Chem 19:1639-1662
31. Rusbridge EK, Peng Y, Powell AK, Robinson D, Fitzpatrick AJ (2018) Dalton Trans 47:7644-7648
32. Kang W, Huo LH, Gao S, Ng SW (2009) Acta Crystallogr Sect E Struct Rep Online 65(12):m1502
33. Sang LT, Mukesh MJ, Edward RT (2019) Acta Crystallogr E75:308-318
34. Mackenzie CF, Spackman PR, Jayatilaka D, Spackman MA (2017) IUCr J 4(5):575-587

35. El-Megharbel SM, Adam AM, Meghdad AS, Refat MS (2015) Russ J Gen Chem 85:2366-2371
36. Patel MN, Pansuriya PB, Parmar PA, Gandhi DS (2008) Pharm Chem J 42:687-692
37. Sissi C, Palumbo M (2010) Cell Mol Life Sci 67:2001-2024

Chapter IV

Tetrachlorocuprate(II) hybrid solids templated by aminopyridines

Summary

In this chapter, phenomenon of chromotropism in aminopyridine based tetrachlorocuprates has been investigated. Isomeric aminopyridines namely 2-, 3- and 4-aminopyridine (*ampy*) based tetrachlorocuprate(II) solids *viz.* (2-H*ampy*)$_2$[CuCl$_4$] (**6**), (3-H*ampy*)$_2$[CuCl$_4$] (**7**) and (4-H*ampy*)$_2$[CuCl$_4$].H$_2$O (**8**) were synthesized under ambient condition using solvent evaporation method upon reacting copper(II) chloride with aminopyridine (*ampy*) in the presence of hydrochloric acid. The structural elucidation of the synthesized solids was carried out using fourier transform infrared spectroscopy, CHN analyses, single crystal X-ray diffraction and powder X-ray diffraction. The thermal stability of the solids was established using thermogravimetric analysis and spin only magnetic moment was calculated by means of magnetic susceptibility measurements. In addition, a detailed investigation of the intermolecular interactions and proportion of contacts has been evaluated using Hirshfeld surface analyses and associated 2-D finger print plots. Solids **6-8** exhibited chromotropism particularly solvatochromism and vapochromism. In addition, **8** showed reversible thermochromism in the solid state. Solids **6-8** belong to Type IV of hybrid solids.

IV.1 Introduction

Chromotropism is the reversible or irreversible change in color of a substance due to the physical and chemical properties of its ambient surrounding medium, such as temperature, pressure, light, solvent and ions [1]. The type of hybrid solids in which the above phenomena occur most frequently is undoubtedly the area of coordination complexes (Type IV). Among the different types of coordinate compounds of copper(II), anionic halocuprate(II) complexes containing protonated organic moieties as counter-ions represent a unique category of hybrid solids. Interestingly, most of these solids reported in literature exhibit thermochromism (refer Table IV.1). Thermochromism is a special type of chromotropism in which a solid undergoes a change in color upon heating [2]. This unique feature can be attributed to the ability of $\{CuCl_4\}^{2-}$ units to exist as either tetrahedral or square-planar motifs. In most of the cases, usually the green $\{CuCl_4\}^{2-}$ square planar phase undergoes transformation into pale green or yellow colored $\{CuCl_4\}^{2-}$ tetrahedral phase upon heating [3]. On the other hand, a very few tetrachlorocuprate(II) anion based solids can undergo a change in color upon applying pressure i.e. piezochromism [4,5] as shown in Figure IV.1. However, only two examples of photochromism [6] in tetrachlorocuprate(II) anion based solids has been reported so far [7,8]. To the best of our knowledge, other forms of chromotropism particularly vapochromism [9,10] or solvatochromism [11,12] have not been explored in tetrachlorocuprate(II) anion based solids. Therefore, based on the above considerations, in this chapter an attempt has been made to synthesize tetrachlorocuprates based on three isomeric aminopyridines (*ampy*) and to explore their ability to act as chromotropic probes. Under our experimental conditions, reaction of copper(II) chloride with 2-, 3- and 4-*ampy* in the presence of hydrochloric acid resulted in solids *viz.* (2-H*ampy*)$_2$[CuCl$_4$] (**6**), (3-H*ampy*)$_2$[CuCl$_4$] (**7**) and (4-H*ampy*)$_2$[CuCl$_4$].H$_2$O (**8**) under ambient conditions.

Hirshfeld surface analyses and 2-D finger print plots revealed significant intermolecular interactions that stabilize the crystal structures. It was found that **6-8** exhibited solvatochromism and vapochromism. In addition, **8** showed reversible thermochromism in the solid state. It is noteworthy that solvatochromism and vapochromism in $\{CuCl_4\}^{2-}$ based hybrid solids have been demonstrated for the first-time using solids **6-8**.

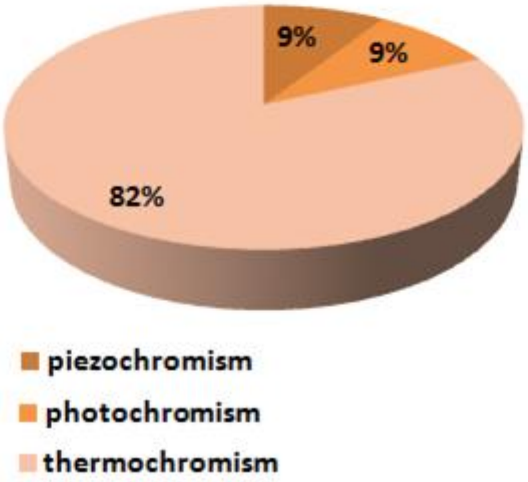

Figure IV.1 Figure showing the percentage of tetrachlorocuprate(II) anion based solids exhibiting thermo-, photo- and piezochromism.

Table IV.1 Literature review of Tetrachlorocuprate(II) solids exhibiting chromotropism.

S.No.	Solid	Cell parameters	Geometry of copper center	Synthesis	Chromotropic property	Ref.
1.	(DMe-DABCO)$[CuCl_4]$ DMe-DABCO = N,N'-dimethyl-1,4-diazoniabicyclo[2.2.2] octane	Monoclinic, $Pca2_1$ $a = 19.676$Å, $b = 8.083$Å, $c = 17.679$Å $\beta = 92°$, Z = 8 Yellow crystals	Distorted tetrahedral geometry	Hydrothermal technique	Thermochromism	[3]
2.	$(pipzH_2)[CuCl_4].2H_2O$	Monoclinic, $C2/c$ $a = 10.538$Å, $b = 7.431$Å, $c = 17.281$Å $\beta = 111.90°$, Z = 4, Yellow crystals	Distorted tetrahedron	Solvent evaporation	Thermochromism, Photochromism	[7]
	$(pipzH_2)_2[CuCl_4]Cl_2.3H_2O$ *pipz*= piperazine	Triclinic, P-1 $a = 9.264$Å, $b = 10.447$Å, $c = 11.366$ Å $\alpha = 68.38°$, $\beta = 82.86°$, $\gamma = 83.05°$, Z = 2 Green crystals	Square planar geometry			
3.	$(C_4H_9NH_3)_2[CuCl_4]$	Cell parameters not reported. Golden sheet-like crystals	Distorted tetrahedron	Reflux followed by recrystallization	Photochromism	[8]
4.	$[CH_3C(NH_2)_2]_2[CuCl_4]$ $CH_3C(NH_2)_2$ = acetamide	Monoclinic, $P2_1/a$ $a = 23.06$Å, $b = 7.93$Å, $c = 14.69$Å $\beta = 94.5°$, Z = 4, Yellow plates	Distorted tetrahedral geometry	Solvent evaporation	Thermochromism	[13]

5.	$(C_2H_5NH_3)_2[CuCl_4]$	Orthorhombic, *Pbca* a = 21.18Å, b = 7.47Å, c = 7.35Å Z = 4, Yellow sheets	Square planar	Solvent evaporation	Thermochromism	[14]
6.	$[(NH_3CH_2CH_2)_2NH_2]Cl.[CuCl_4]$	Orthorhombic, *Pnma* a = 7.117Å, b = 23.78Å, c = 7.342 Å Z = 4 a = 7.15Å, b = 23.70Å, c = 7.36 Å Z = 4, Yellow, green, orange*	Square planar	Solvent evaporation	Thermochromism	[15]
7.	$[(CH_3)_2CHNH_3]_2[CuCl_4]$	Triclinic, P-1 a = 7.245 Å, b = 14.588Å, c = 21.738Å α = 87.08°, β = 103.59°, γ = 104.73° Z = 6, Green needles[1a]	Distorted square planar geometry	Solvent evaporation	Thermo-Chromism[2]	**1a**. [16] **1b.** [17] **2.** [18]
	$[(C_2H_5)_2NH_2]_2[CuCl_4]$	Monoclinic, $P2_1/n$ a = 7.293Å, b = 14.881Å, c = 44.751Å β = 90.12°, Z = 12, Green needles[1b]	Distorted square planar geometry	Solvent evaporation		
8.	$[C_6H_5CH_2CH_2NHCH_3H]_2[CuCl_4]$	Monoclinic, $P2_1/c$ a = 6.495Å, b = 22.678Å, c = 8.584Å β = 116.08°, Z = 2, Green needles	Square planar geometry	Solvent exchange method	Thermochromism	[19]

9.	[*bzpipzn*] $[CuCl_4]0.5H_2O$	Monoclinic, $P2_1/a$ a = 17.015Å, b = 16.977Å, c = 11.377Å β = 97.15°, Z = 8, Yellow crystals	Moderately flattened tetrahedral geometry	Solvent evaporation	Thermochromism	[20]
	[*bzpipzn*]$[CuCl_4]$ *bzpipzn*= N-benzyl piperazine	Monoclinic, $P2_1$ a = 12.075Å, b = 28.479Å, c = 9.925Å β = 109.54°, Z = 8, Green crystals	Unequally flattened tetrahedral			
10.	Bis(dipropylammonium) tetrachlorocuprate(II)	Orthorhombic, *Pbca* a = 13.029Å, b =15.252Å, c = 20.997 Å Z = 8, Light green plates	Distorted tetrahedral geometry	Solvent evaporation	Thermochromism	[21]
11.	$(nmpH)_2[CuCl_4]$ *nmp* = N-methylphenethyl amine)	Monoclinic, $P2_1/c$ a = 6.495Å, b = 22.678Å, c = 8.584Å β = 116.08°, Z = 2, Green needles[1a]	Square planar geometry	Solvent exchange method	Piezochromism[2]	**1a.** [19] **1b.** [22] **1c.** [23] **1d.** [24]
	$(NphpipH_2)[CuCl_4]$ N*phpip*=N-phenyl piperazine	Orthorhombic, $P2_12_12_1$ a = 17.698Å, b = 8.615Å, c = 9.841 Å Z = 4, Yellow-green crystals[1b]	Flattened tetrahedral geometry	Solvent evaporation		**2**. [4]
	$(NbzpipzH_2Cl)_2[CuCl_4]$ N*bzpipz* = N-benzyl piperazine	Monoclinic, *Pc* a = 21.954Å, b = 7.089Å, c = 9.139Å β = 97.054°, Z = 2, Green crystals[1c]	Extremely flattened tetrahedron	Solvent evaporation		
	$(tmba)_2[CuCl_4]$ *tmba* = Trimethylbenzyl amine	Monoclinic, $P2_1/n$ a = 9.584Å, b = 9.104Å, c = 28.43Å β = 92.50°, Z = 4, Yellow leaflets[1d]	Flattened tetrahedron	Solvent evaporation		
12.	$(pCH_3C_6H_4NH_3)_2$	Orthorhombic, *Pbca*	Distorted	Solvent	Thermochromism[1a]	**1a**.[25]

	$[CuCl_4]$ $(pClC_6H_4NH_3)_2$ $[CuCl_4]$	a = 6.911Å, b = 7.052Å, c = 33.182 Å Flat sheet like yellow crystals$^{\mathbf{1a}}$ Monoclinic, $P2_1/c$ a = 16.4359Å, b = 7.396Å, c = 7.262 Å β = 101.51°, Z = 2 Brown plate like crystals$^{\mathbf{1b}}$	tetrahedral geometry Distorted tetrahedral geometry	evaporation Solvent evaporation		**1b**.[26]
13.	$(C_4H_6ClN_2S)_2[CuCl_4]$ $(C_4H_7N_2S)_2[CuCl_4]$	Triclinic, P-1 a = 8.168Å, b = 10.919Å, c = 11.437 Å α = 64.24°, β = 80.03°, γ = 84.72° Z = 2, Amber colored crystals Triclinic, P-1 a = 7.750Å, b = 8.474Å, c = 11.437 Å α = 64.24°, β = 80.03°, γ = 84.72°, Z = 2 Yellow colored crystals	Distorted tetrahedral geometry Distorted tetrahedral geometry	Solvent evaporation Solvent evaporation	Thermochromism	[27]
14.	$(C_3N_3H_{10})_2[CuCl_4]$	Triclinic, P-1 a = 9.522Å, b = 11.215Å, c = 7.680 Å α = 93.85°, β = 100.41°, γ = 84.48°, Z = 2, Green-yellow crystals	Flattened tetrahedron	Solvent evaporation	Thermochromism	[28]
15.	$(C_5N_3H_8O)_2[CuCl_4]$	Triclinic, P-1 a = 11.053Å, b = 11.334Å, c = 14.038Å α = 95.76,β = 101.35, γ = 90.15°, Z = 4 Dark green crystals	Square planar geometry	Solvent evaporation	Thermochromism	[29]
16.	$(C_7H_{11}N_2)_2[CuCl_4]$	Monoclinic, $C2/c$ a = 11.973Å, b = 12.522Å, c = 14.523Å β = 113.86°, Z = 4 Parallelepiped shaped yellow crystals	Compressed tetrahedral geometry	Solvent evaporation	Thermochromism	[30]
17.	$2[(CNH_2)_3][CuCl_4]$.	Monoclinic, $P2_1/c$	Pseudo	Solvent	Thermochromism	[31]

	$2H_2O$	a = 8.084Å, b = 18.484Å, c = 16.939 Å β = 91.44°, Z = 8 Parallelepiped yellowish-green crystals	tetrahedral geometry	evaporation		
18.	$(C_7H_7N_2)_2[CuCl_4]$	Monoclinic, *C2/c* a = 14.903Å, b = 7.815Å, c = 16.130Å β = 92.93°, Z = 8, Yellow crystals	Distorted tetrahedral geometry	Solvent evaporation	Thermochromism	[32]
19.	$(C_8H_{12}N)_2CuCl_4$	Triclinic, *P*-1 a = 7.923Å, b = 9.150Å, c = 16.134Å α = 75.40°, β = 86.96°, γ = 64.49° Z = 2, Yellow crystals	Flattened tetrahedral geometry	Solvent evaporation	Thermochromism	[33]
20.	(EDBE)$[CuCl_4]$ EDBE= 2,2'-(ethylenedioxy)bis(ethyl ammonium)	Orthorhombic, *Pccn* a = 23.613Å, b = 7.594Å, c = 7.625Å Z = 4, Thin yellow - green plates^{1}	Distorted tetrahedral geometry	Layering method	Thermochromism, Piezochromism^{2}	**1**.[34] **2.**[5]
21.	$[(R)\text{-}(+)\text{-}1\text{-}C_{10}H_7CH(CH_3)NH_3][CuCl_4]$	Monoclinic, $P2_1$ a = 12.715Å, b = 7.197Å, c =14.054Å β = 94.37°, Z = 2, Yellow crystals	Highly distorted tetrahedral geometry	Solvent evaporation	Thermochromism	[35]
	$[(R)\text{-}(+)\text{-}2\text{-}C_{10}H_7CH(CH_3)NH_3][CuCl_4]$	Monoclinic, C_2 a = 10.796Å, b = 7.234Å, c =16.945Å β = 97.00°, Z = 2, Green crystals	Distorted square planar	Solvent evaporation	Thermochromism	
22.	$(C_7H_7N_2S)_2[CuCl_4]$	Monoclinic, $P2_1/c$ a = 6.952Å, b = 9.697Å, c = 13.963Å β = 97.84°, Z = 2, Green crystals	Square planar	Reflux followed by recrystallization	Thermochromism	[36]

* Yellow plates at room temperature (RT), pale green below RT, convert to orange brown on heating to 120°C

IV.2 Experimental

IV.2.1 Synthesis

Initially, (2-H*ampy*)$_2$[CuCl$_4$] (**6**), (3-H*ampy*)$_2$[CuCl$_4$] (**7**) and (4-H*ampy*)$_2$[CuCl$_4$].H$_2$O (**8**) were crystallized from a solution of CuCl$_2$.2H$_2$O, *ampy* and HCl in methanol or water as per the procedure given in literature by Kumar *et. al.*[37] and Halvorson *et. al.*[38] respectively. For the synthesis of **6** and **7**, Cu(II)acetate.2H$_2$O (198 mg, 1 mmol) was dissolved in water (10 mL) and concentrated HCl (4 mL). Subsequently, aminopyridine (188 mg, 2 mmol) in methanol (15 mL) was added and the solution was kept for crystallization at room temperature. On the other hand, crystals of **7** were obtained upon evaporation of a saturated solution of 4-*ampy* and CuCl$_2$.2H$_2$O in a dilute HCl solution. The cell parameter of the as-synthesized crystals was established by single crystal X-ray diffraction.

In the present work, however it was observed that **6-8** could be synthesized using only water as a solvent (Scheme IV.1). Initially, 10 mL of an aqueous solution of 2-*ampy* (0.553 g, 2 mmol) was added to an aqueous solution (10 mL) of CuCl$_2$.2H$_2$O (0.507 g, 1 mmol) and stirred using a magnetic stirrer. 5M HCl was added dropwise to obtain a clear blue solution having pH = 1.0±0.1. The resultant solution was left undisturbed for crystallization. After a few weeks, orange crystalline blocks of **6** were obtained (yield, 78.9% based on copper). The crystals were filtered, washed with water and acetone and dried in air. The same procedure was repeated using 3-*ampy* and 4-*ampy* and green crystalline blocks of solid **7** (yield, 77.5% based on copper) and yellow flakes of solid **8** (yield, 79.2% based on copper) respectively were obtained after a few weeks. The phase purity of the as-synthesized crystals was established by Rietveld analysis [39].

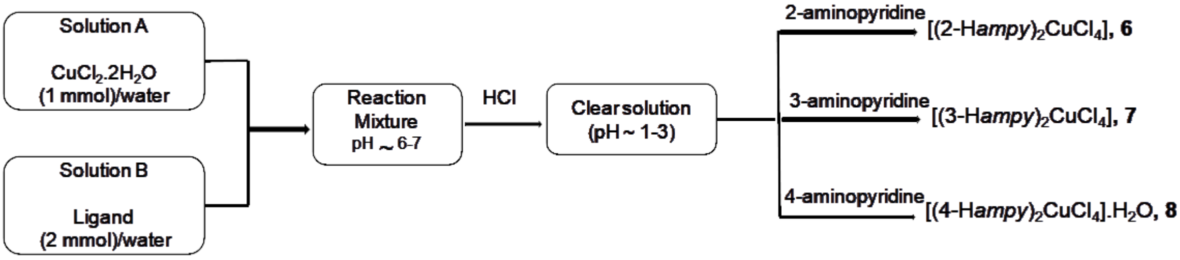

Scheme IV.1 Scheme showing the synthetic protocol.

IV.2.2 Characterization

The solids were characterized using techniques discussed under Section II.2.3 in Chapter II. Elemental analyses (C, H and N) were performed on ELEMENTAR Vario EL III CHNS Analyzer. The magnetic susceptibilities of the solids **6-8** were determined at room temperature using Guoy Balance (Sherwood, UK) and the spin only magnetic moment of the solids was calculated. The solid-state absorption spectra were recorded on a Jasco V-550 UV/Vis spectrophotometer in the range 200-800 nm. The electronic absorption spectra of **6-8** in different solvents were measured using Shimadzu UV-1800 spectrophotometer in the range 400-900 nm.

Results of CHN analysis of the bulk product were found to be consistent with the stoichiometry. Anal. Found:C, 30.01; H, 3.42; N, 14.08 %: Calcd: C, 30.30; H, 3.54; N, 14.15 % for **6**; Anal. Found: C, 30.25; H, 3.59; N, 14.50 %: Calcd: C, 30.30; H, 3.54; N, 14.15 % for **7** and Anal. Found: C, 21.06; H, 2.98; N, 10.42 %: Calcd: C, 21.53; H, 2.87; N, 10.05 % for **8**.

IV.2.3 Hirshfeld Surface Analyses

The molecular Hirshfeld surface analyses and their associated 2-D fingerprint plots (full and decomposed) were mapped employing the *CrystalExplorer* 21.5 program [40]. The CIF files of the solids were given as input [37,38]. The Hirshfeld surfaces were generated using a standard (high) surface resolution. The 2-D fingerprint plots were displayed using the expanded 0.6–2.8Å range view with the d_e (distance from a point on the surface to the nearest nucleus outside the surface) and d_i (distance from a point on the surface to the nearest nucleus inside the surface) scales shown on the graph axes.

IV.2.4 Investigation of vapochromism

0.5 g of solid **6** was heated in a silica crucible at 100°C for 30 minutes and cooled in a desiccator for 2 hours. Thereafter, a small glass vial (10 mL capacity) containing 5 ml of double distilled water and the silica crucible were placed in a sealed glass jar for 18 hours. The same procedure was repeated with ammonia as another analyte. Similar experiments were performed with solids **7** and **8**.

IV.2.5 Investigation of solvatochromism

Solvatochromic property of the solids was investigated by measuring the absorption spectra of the solids in different solvents like water, ethanol, acetone and dimethyl formamide (DMF) in the range 400-900 nm. The concentration of the solutions was adjusted to 3×10^{-6} M.

IV.2.6 Investigation of thermochromism

0.5 g of solids **6-8** was heated at 120°C in a silica crucible for 15 minutes and then cooled to room temperature in order to establish the reversibility of the process.

IV.3 Results and Discussions

IV.3.1 Crystal structure description

The crystallographic details for solids **6-8** have been summarized in Table IV.2.

Table IV.2 Crystallographic details of solids **6-8**.

	6	**7**	**8**
Formula	$C_{10}H_{14}Cl_4CuN_4$	$C_{10}H_{14}Cl_4CuN_4$	$C_{10}H_{16}Cl_4CuN_4O$
Formula weight	395.59	395.59	557.45
T (K)	293(2)	293(2)	295(2)
Space Group	*P*-1	*P*-1	*C*2/*c*
a, Å	7.929(4)	7.9736(7)	8.457(2)
b, Å	8.115(3)	8.1332(8)	14.318(2)
c, Å	13.667(4)	13.6304(13)	14.382(2)
α, °	91.21(3)	91.231(2)	90
β, °	94.71(3)	94.731(2)	95.82(1)
γ, °	114.55(4)	115.009(10)	90
V, $Å^3$	795.71(50)	796.78(13)	1732.50(184)
Z	2	2	4
d_{calc}, $g\cdot cm^{-3}$	1.651	1.649	2.137
$\mu_{MoK\alpha}$, cm^{-1}	2.034	2.032	2.347
λ (Å)	0.70930	0.71073	0.71073
$R_1(I>2\sigma I)$, WR_2(all)	0.0576, 0.1572	0.0455, 0.1344	0.0349, 0.0750
GOF	1.109	1.089	1.055

The asymmetric unit in all the three solids showed $[CuCl_4]^{2-}$anionic moiety displaying a distorted tetrahedral geometry. Solids **6** and **7** crystallized in the space group *P*-1 in contrast to solid **8** which crystallized in a monoclinic crystal system with space group *C*2/*c* and it had an additional lattice water molecule. In all the three solids, only the pyridinium N atom was protonated, whereas the amine group was unprotonated, resulting in a charge of +1 for the organic cation. Solids **6** and **7** were found to be isostructural (Figure IV.2). In **6** and **7**, each $[CuCl_4]^{2-}$ unit was hydrogen bonded to surrounding protonated aminopyridine moieties to form 1-D chains (Figure IV.3) which were further connected to form 3-D network (Figure IV.4). The crystal packing in **6** and **7** was also reinforced by $\pi\cdots\pi$ interactions between the protonated aminopyridine moieties. Also refer Table IV.3 and IV.4 for H-bonding interactions in **6** and **7**.

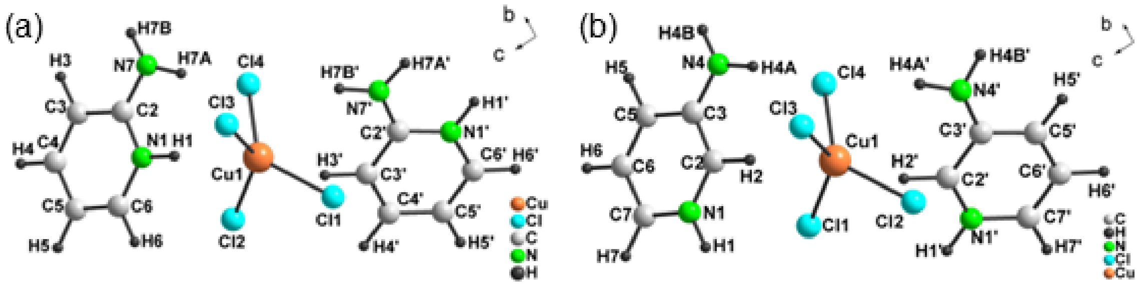

Figure IV.2 Asymmetric unit of (a) **6** and (b) **7**.

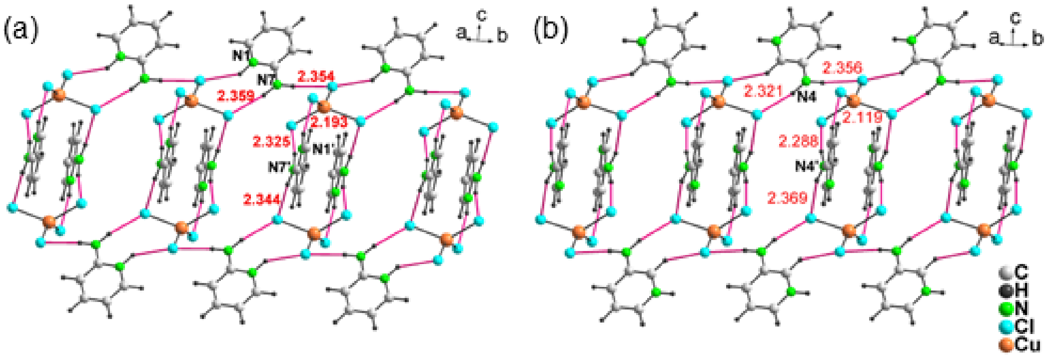

Figure IV.3 1-D chains formed via H-bonding interactions mediated by protonated aminopyridine moieties in (a) **6** and (b) **7**. Intra-chain H-bonding interactions are shown as red lines.

Table IV.3 H-bonding interactions in **6**.

D-H...A	D-H (Å)	H...A (Å)	D...A (Å)	∠ D-H...A (°)
N7-H7A···Cl	0.969(54)	2.359(69)	3.289(47)	160.71(3)
N1-H1···Cl2	1.009(14)	2.415(15)	3.230(35)	137.26(23)
N7-H7B···Cl4	0.995(47)	2.344(70)	3.334(80)	173.26(35)
N1-H1···Cl3	1.010(15)	2.193(14)	3.174(28)	163.40(24)
N7-H7B··· Cl2	0.982(42)	2.354(44)	3.333(7)	173.86(26)

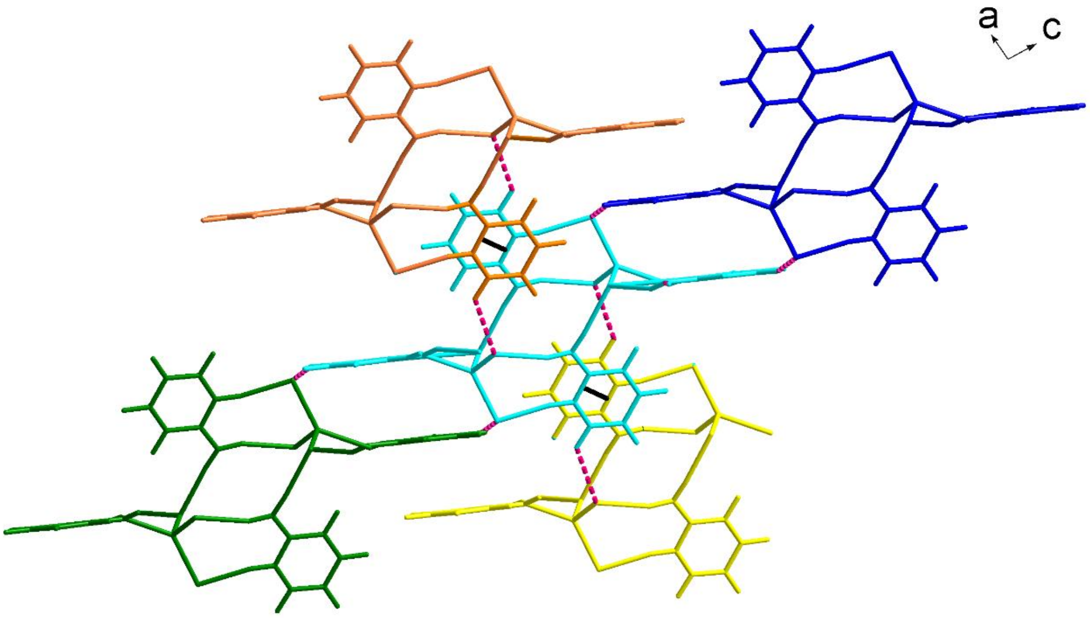

Figure IV.4 Through H-bonding interactions each 1-D chain is further extended into 3-D framework. Figure showing one chain (cyan) connected to four others (green, blue, orange, yellow). Inter-chain H-bonding interactions are shown in red dashed lines. Crystal packing in **6** and **7** is also facilitated by π···π interactions (3.767(31) and 3.779(1) Å respectively). π···π interactions are shown as black lines.

Table IV.4 H-bonding interactions in **7**.

D-H...A	**D-H (Å)**	**H...A (Å)**	**D...A (Å)**	**∠ D-H...A (°)**
N4-H4A···Cl4	0.983(59)	2.321(64)	3.289(5)	168.14(41)
N4-H4B···Cl1	0.995(39)	2.356(40)	3.344(5)	171.78(26)
N4-H4A···Cl4	0.992(38)	2.369(38)	3.330(6)	163.05(32)
N4-H4B···Cl2	0.989(34)	2.288(36)	3.260(5)	167.77(26)
C2-H2··· Cl4	1.081(3)	2.815(3)	3.726(4)	141.90(15)
C2- H2···Cl1	1.081(3)	2.367(1)	3.241(4)	136.86(16)
C5-H5···Cl3	1.081(3)	2.119(1)	3.167(4)	162.56(15)

Unlike, solids **6** and **7**, in **8** an additional lattice water molecule was observed in its asymmetric unit which enabled H-bonding interactions between $[CuCl_4]^{2-}$ units and water molecules to form 1-D chains propagating along *a* axis (Figure IV. 5). Through H-bonding interactions each 1-D chain was further extended into 3-D framework (Figure IV. 6). Also refer Table IV.5 for H-bonding interactions in **8**.

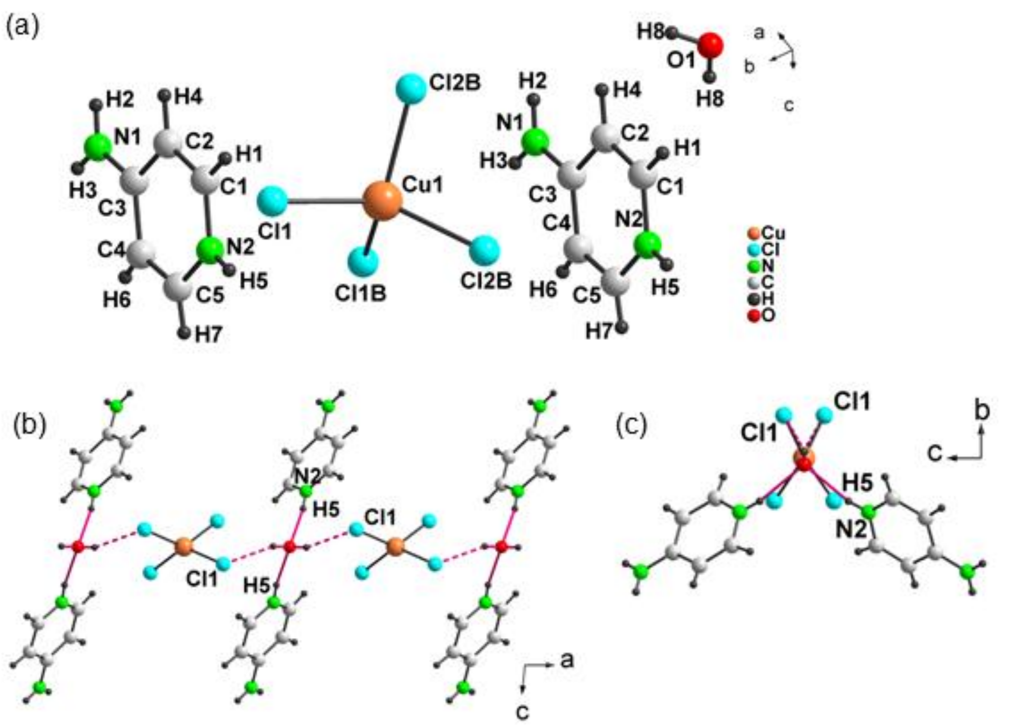

Figure IV.5 (a) Asymmetric unit in (4-H*ampy*)$_2$[CuCl$_4$].H$_2$O, **8**. (b) 1-D chains formed via H-bonding interactions mediated by protonated aminopyridine moieties and water molecule. H-bonding interactions mediated by lattice water molecule and [CuCl$_4$]$^{2-}$are shown in red solid and dashed lines respectively. (c) View along *a* axis.

Table IV.5 H-bonding interactions in **8**.

D-H...A	**D-H (Å)**	**H...A (Å)**	**D...A (Å)**	**∠ D-H...A (°)**
N2-H5···O1	0.798(46)	2.040(46)	2.824(5)	166.99(446)
O1-H8···Cl1	0.800(29)	2.456(32)	3.224(6)	161.36(27)
N1-H3···Cl2	0.795(40)	2.585(40)	3.353(5)	162.96(37)
N1-H2···Cl1	0.803(44)	2.582(43)	3.367(11)	124.31(10)

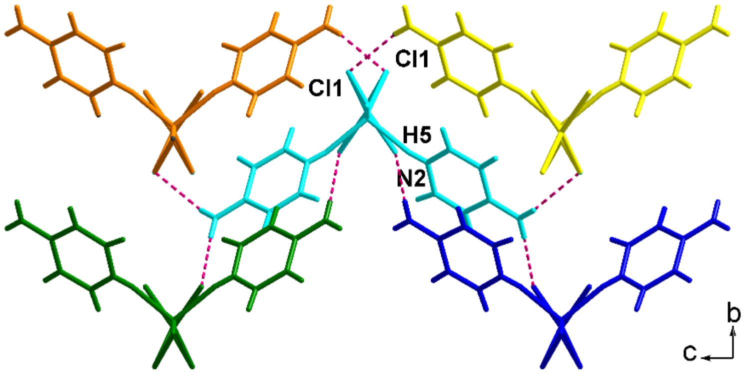

Figure IV.6 Through H-bonding interactions each 1-D chain is further extended into 3-D framework. Figure showing one chain (cyan) connected to four others (green, blue, orange, yellow). Inter-chain H-bonding interactions are shown in red dashed lines.

IV.3.2 Rietveld Analysis

Rietveld powder diffraction analysis of all the solids was carried out using GSAS to ensure homogeneity of the synthesized products. The phase purity of all the solids was established by Rietveld analysis and it was found that the cell parameters and space group from experimental powder data of bulk sample match well with those reported in literature [37,38]. Figures IV.7-9 represents Rietveld refinement of **6**-**8**. The red corresponds to the experimental data while black represents the calculated profile. The blue line gives the difference between the experimental and calculated diffraction profile.

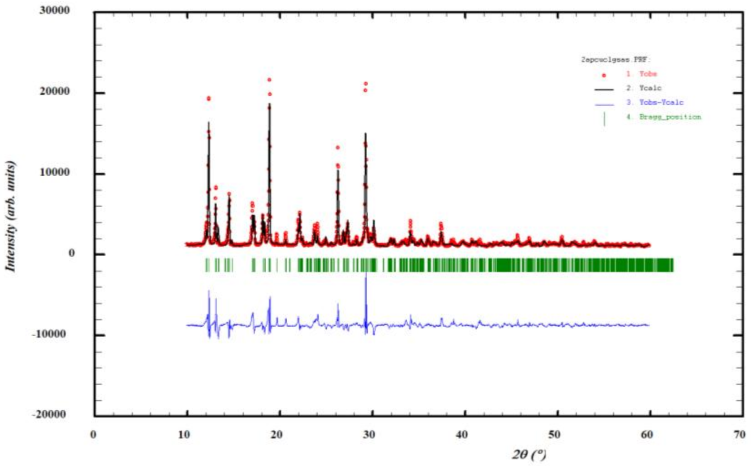

Figure IV.7 Rietveld refinement plot of **6.**

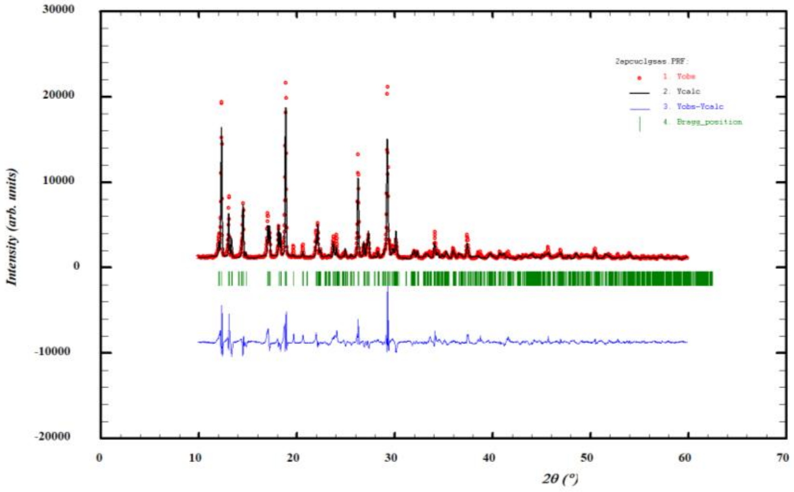

Figure IV.8 Rietveld refinement plot of **7.**

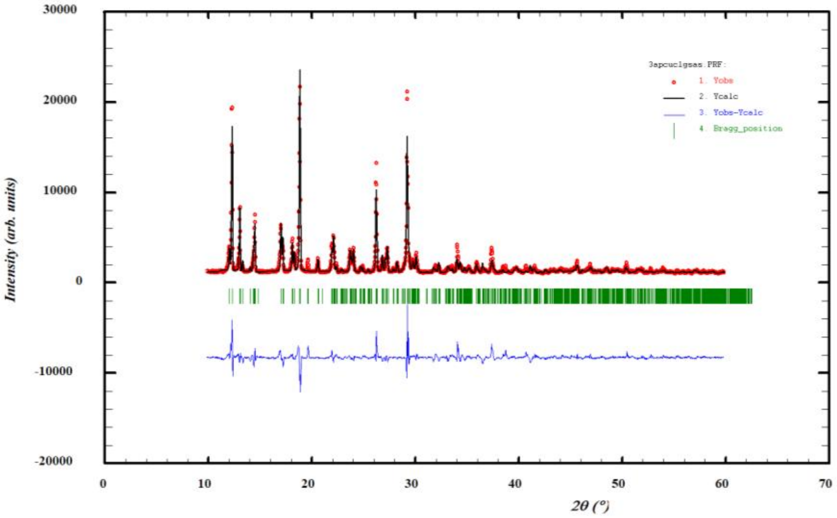

Figure IV.9 Rietveld refinement plot of **8.**

IV.3.3 Vibrational analyses

FTIR spectra of **6-8** showed a medium intensity band in the region 490-418 cm^{-1} due to Cu-Cl vibrations (Figure IV.10). The peaks due to N-H stretching vibrations could also be seen at around 3300-3100 cm^{-1}. The strong peaks in the range 1650-1540 cm^{-1} could be attributed to N-H bending vibrations [41]. A medium intensity band due to the C-N stretching was observed at around 1200 cm^{-1}.

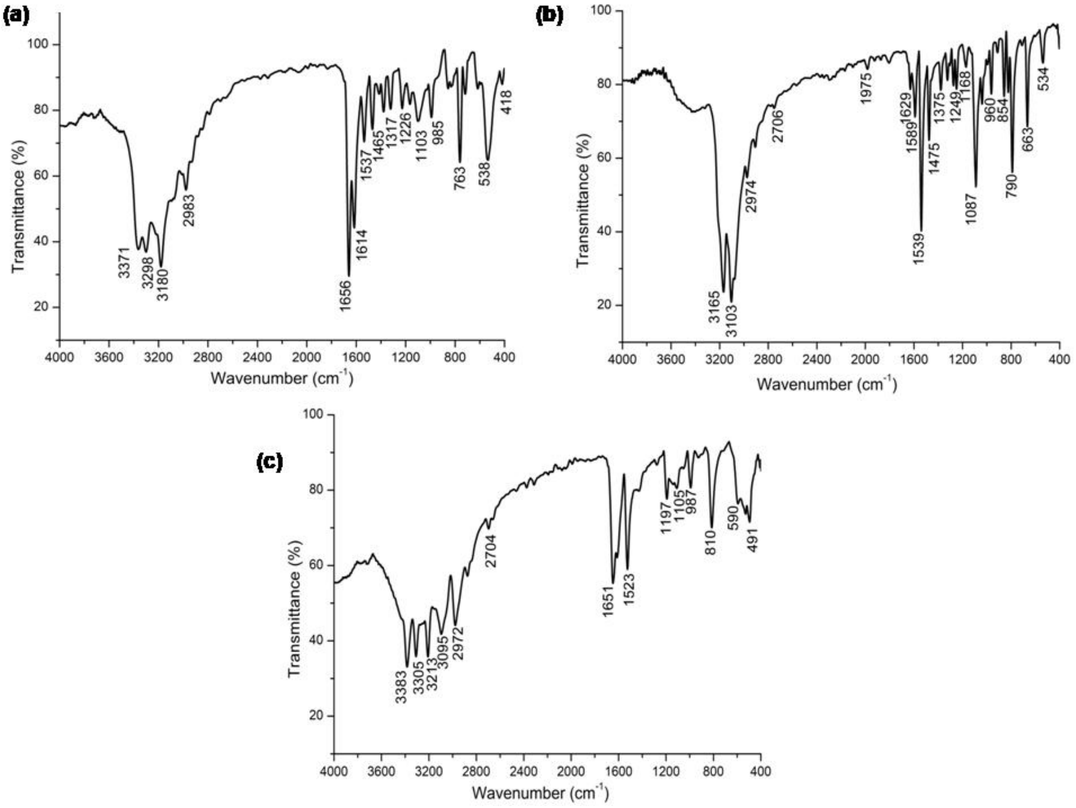

Figure IV.10 FTIR spectra of solids **6-8**.

IV.3.4 Thermal analyses

The thermal stability of solids **6-8** was established using TGA. For solids **6** and **7**, weight loss occurred in two consecutive steps in the temperature range of 160-330°C and 400-620°C, corresponding to the release of protonated aminopyridines and chloride ions respectively. The residual solid (~16%) could be attributed to elemental copper (Figure

IV.11). The TGA curve of **8** displayed three consecutive steps of weight loss in the temperature range 50-850°C which can be attributed to the loss of water molecule, aminopyridine moieties and chloride ions, leaving behind the residue of elemental copper (~19%) as shown in Figure IV.12. Differential Thermal Analysis (DTA) was also carried out to confirm the loss of lattice water molecule in **8**.

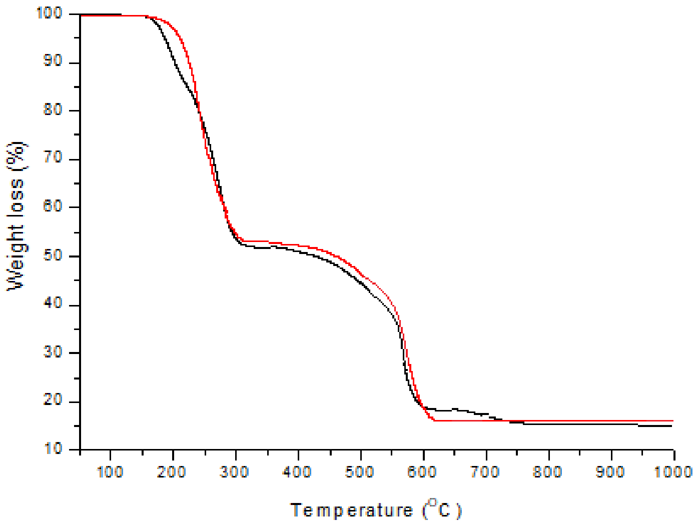

Figure IV.11 TGA curves of **6** and **7**.

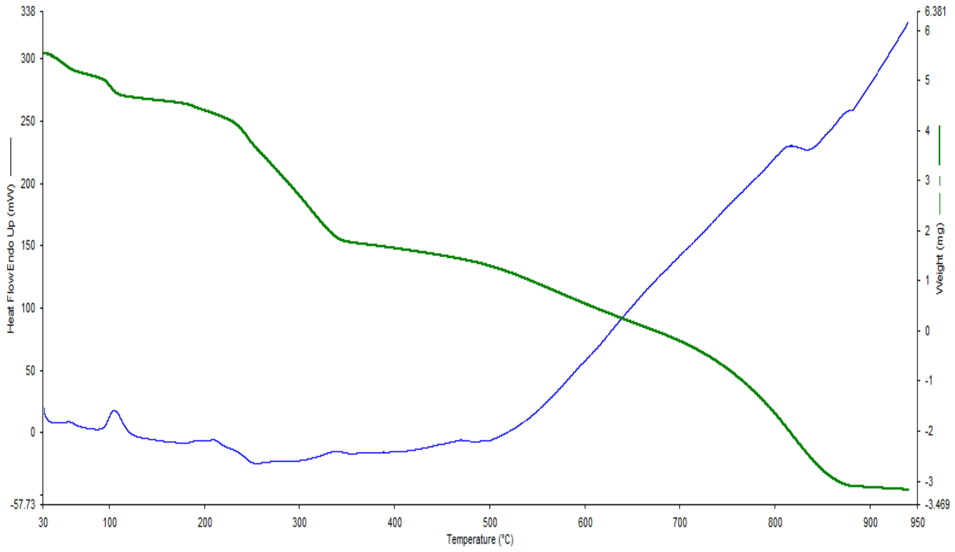

Figure IV.12 TGA-DTA curve of **8**.

IV.3.5 Magnetic studies

The spin only magnetic moment of the solids was found to be 1.4, 1.73 and 1.84BM for **6**, **7** and **8** respectively, which confirmed the +2 oxidation state of copper in **6-8**. The values were calculated using equations discussed under section III.2.3 in Chapter III. While **7** seemed to be paramagnetic in nature, a lower magnetic moment in **6** indicated anti-ferromagnetic interactions similar to those of related structures reported in literature [42, 43].

Table IV.6 Magnetic susceptibility measurements.

Solid	R_0	R	L (cm)	C	W (g)	χ_g	MW (g)	χ_m	μ (BM)
6	-24	100	1.8	1	0.1071	2.084×10^{-6}	395.5	0.861×10^{-3}	**1.4**
7	-29	118	1.7	1	0.0784	3.187×10^{-6}	395.5	1.26×10^{-3}	**1.73**
8	-29	86	1.6	1	0.0511	3.6×10^{-6}	413.5	1.422×10^{-3}	**1.84**

IV.3.6 Hirshfeld Surface Analyses

In order to get a deeper insight into various intermolecular interactions in the solids, the Hirshfeld surfaces (d_{norm}, d_i, d_e, shape index and curvedness) and 2-D fingerprint plots were generated using *Crystal Explorer 21.5* [40].

The Hirshfeld surfaces of **6** cover 374.05Å^2 area and spread over 388.96Å^3 volumes with 0.5 isovalue. The 3D d_{norm} surfaces were mapped over a fixed color scale of -0.468 to 1.308Å, the distance to the nearest nucleus inside the surface d_i ranging from 0.801 to 2.657Å, the distance to the nearest atoms outside d_e in the color scale of 0.800 to 2.554Å, whereas, shape index mapped within the color range of -1.000 to 1.000Å, and curvedness in the range of -4.000 to 0.400Å respectively, as shown in Figure IV.13. The surfaces are shown transparent to permit visualization of the crystal structure. The bright red spots on the d_{norm} surface as shown in Figure IV.13a display short intermolecular contacts which mainly corresponds to N-H···Cl and C-H···Cl hydrogen bonding interactions. The appearance of consecutive red and blue triangular patches over the aromatic ring in the shape index map (Figure IV.13d) and large flat regions delineated by a blue outline on the curvedness map (Figure IV.13e) indicate the presence of weak π···π interactions in the crystal packing.

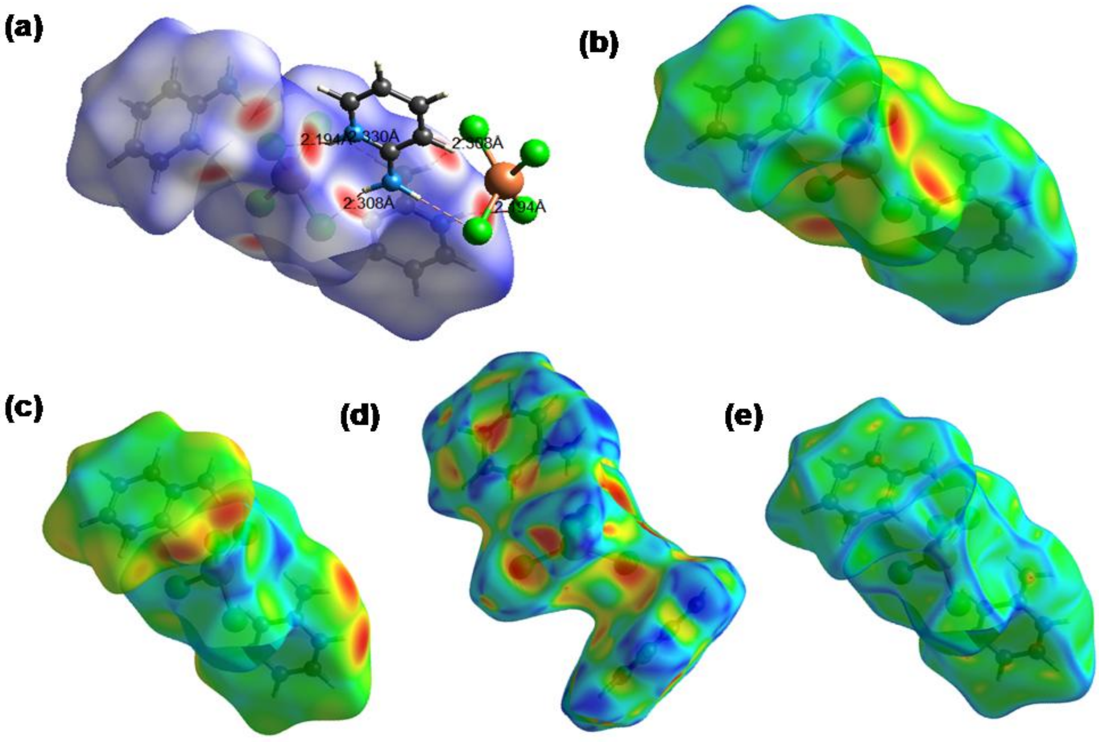

Figure IV.13 Hirshfeld surfaces for visualizing the intermolecular contacts in [(2-H*ampy*)$_2$CuCl$_4$], **6**. (a) d_{norm} highlighting the regions of N—H···Cl and C-H···Cl hydrogen bonds, (b) d_e, (c) d_i, (d) shape index and (e) curvedness.

The Hirshfeld surface of **7** spread over 360.14Å^2 area and holds 390.23Å^3 volume with 0.5 isovalue; the scaled color patches on the surface were generated in the range -0.523 to 1.348Å, 0.766 to 2.684Å, 0.766 to 2.545Å for d_{norm}, d_i and d_e respectively, whereas the shape index plot and curvedness plot are engendered from -1.00 to 1.00 a.u. and -4.000 to 0.400a.u., respectively, as shown in Figure V.14. Similar to **6**, red circular spots on the Hirshfeld surface of **7** indicate intermolecular close contacts of N-H···Cl and C-H···Cl hydrogen bonding interactions as shown in Figure V.14a. Shape index map and curvedness map shows the characteristic features of weak π···π stacking interactions in the crystal structure.

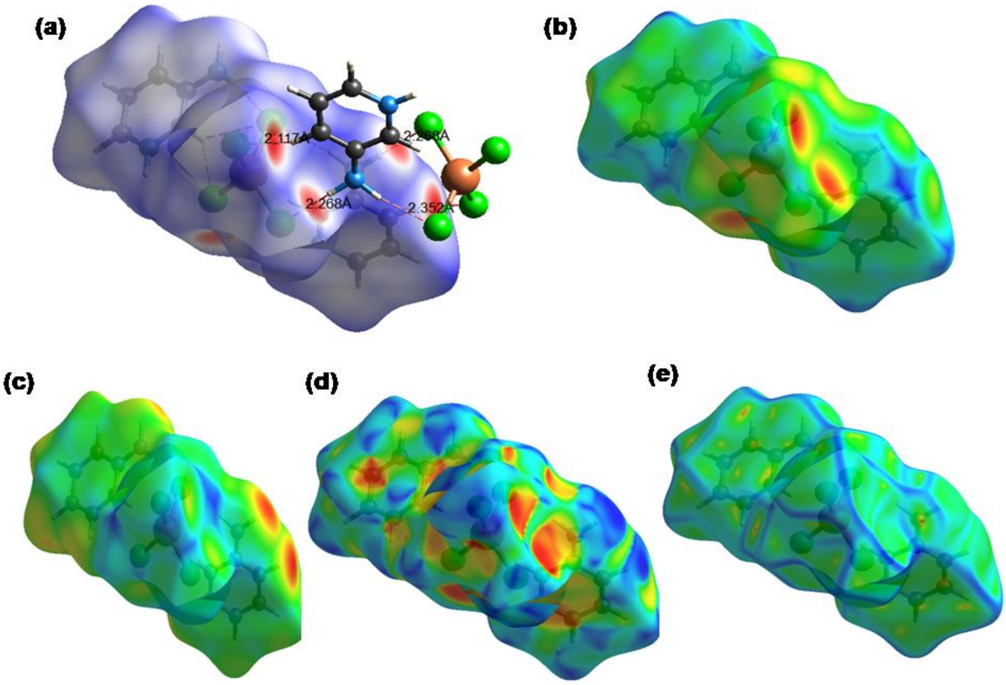

Figure IV.14 Hirshfeld surfaces for visualizing the intermolecular contacts in [(3-H*ampy*)$_2$CuCl$_4$], **7**: (a) d_{norm} highlighting the regions of N—H···Cl hydrogen bonds, (b) d_e, (c) d_i, (d) shape index and (e) curvedness.

The Hirshfeld surface of **8** cover 420.14Å^2 area and holds 490.23Å^3 volume with 0.5 isovalue; the scaled color patches on the surface were generated in the range -0.598 to 1.529Å, 0.745 to 3.195Å, 0.743 to 2.977Å for d_{norm}, d_i and d_e respectively, whereas the shape index plot and curvedness maps are plotted in the range -1.00 to 1.00 a.u. and -4.000 to 0.400a.u., respectively, as shown in Figure V.15. In **8**, the bright red circular spots on the surface correspond to N-H…Cl close contacts and also to H-bonding interactions mediated by water molecule. Shape index and curvedness plots suggests the presence of weak π···π stacking interactions similar to that in **6** and **7**.

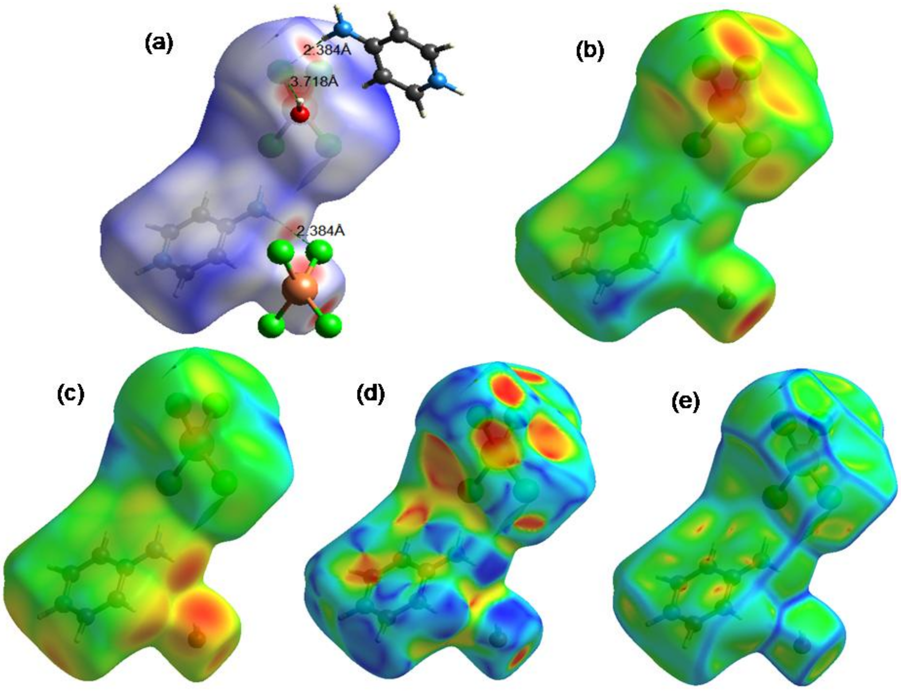

Figure IV.15 Hirshfeld surfaces for visualizing the intermolecular contacts in (4-H*ampy*)$_2$[CuCl$_4$].H$_2$O, **8**: (a) d_{norm} highlighting the regions of N-H···Cl and O-H···Cl hydrogen bonds, (b) d_e, (c) d_i, (d) shape index and (e) curvedness.

IV.3.6.1 Finger print plots

2-D finger print plots are an effective way for quantifying relative contribution of various intermolecular interactions that stabilize the crystal structure. The 2-D plot for overall and individual interactions in the crystal packing of **6**, **7** and **8** are shown in Figures IV.16-18 respectively**.** The most significant contact in all three solids was due to H···Cl/Cl···H contacts since it contributes 51.2% in **6**, 45.3% in **7** and 57.7% in **8** to the overall surface contacts. H···Cl/Cl···H contacts can be attributed to N-H···Cl and C-H···Cl hydrogen bonding interactions and appear as two sharp symmetric spikes in the finger print plots of **6-8** (refer Figures IV.16-18b).The second major contact is H···H, since it has a contribution of 25.9%, 27.2% and 19.8% in the crystal packing of **6**, **7** and **8** respectively. The C···H, N···H contacts also have significant contributions to the HS in all three solids as can be seen in the 2D plots. In **8**, another important contact is O···H contributing to 5.2% to the total surface due to the presence of water of crystallization.

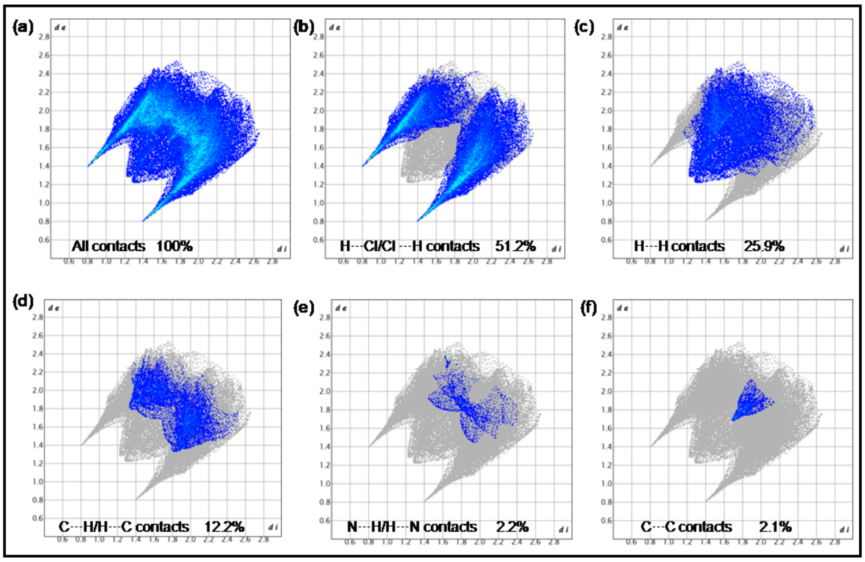

Figure IV.16 2-D fingerprint plots for **6** showing the contributions of different types of interactions: (a) all intermolecular contacts, (b) H···Cl/Cl···H contacts, (c) H···H contacts, (d) C···H/H···C contacts, (e) N···H/H···N contacts and (f) C···C contacts. The outline of the full fingerprint is shown in grey.

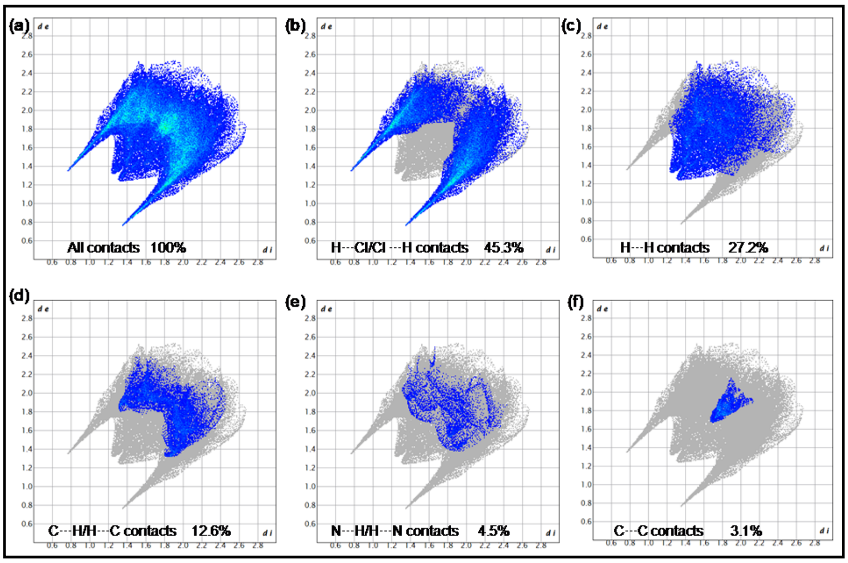

Figure IV.17 2-D fingerprint plots for **7** showing the contributions of different types of interactions: (a) all intermolecular contacts, (b) H···Cl contacts, (c) H···H contacts, (d) C···H/H···C contacts, (e) N···H/H···N contacts and (f) C···C contacts. The outline of the full fingerprint is shown in grey.

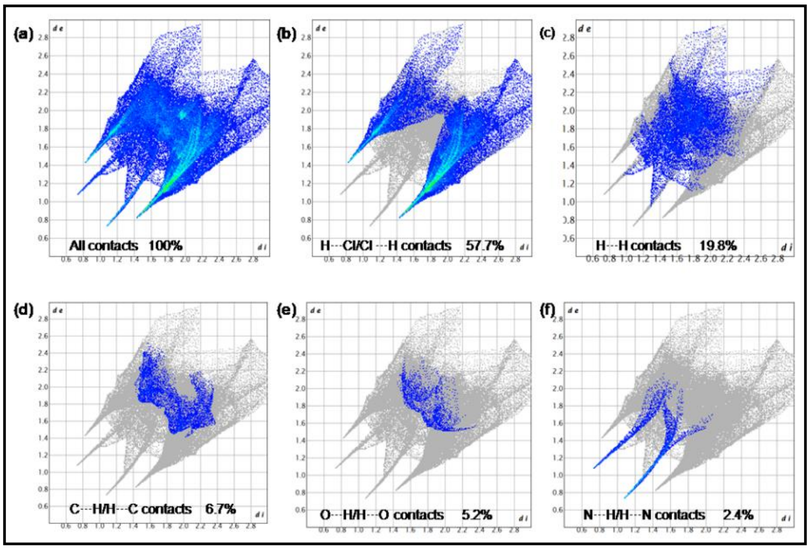

Figure IV.18 2-D fingerprint plots for **8** showing the contributions of different types of interactions: (a) all intermolecular contacts, (b) H···Cl contacts, (c) H···H contacts, (d) C···H/H···C contacts, (e) O···H/H···O contacts and (f) N···H/H···N contacts. The outline of the full fingerprint is shown in grey.

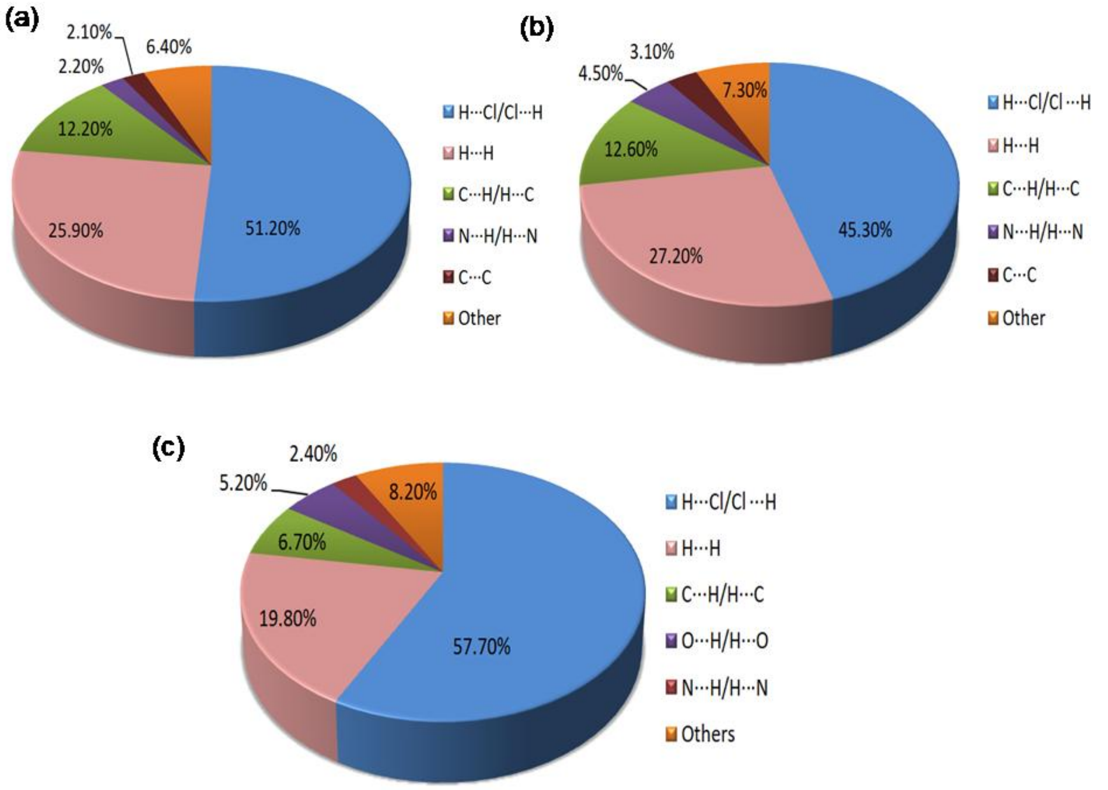

Figure IV.19 Graphical representation of the contribution of interatomic contacts in the crystal packing of (a) **6**, (b) **7** and (c) **8**.

IV.3.6.2 Crystal void analysis

The *Crystal Explorer 21.5* software can also be used to calculate the crystal voids contained in the solids, based on the electron density of the procrystal (0.002 au)-isosurface. Figure IV.20 gives a graphical representation of voids present in the crystal structure of solids **6**-**8**. The void volume in **6**, **7** and **8** corresponds to 75.85Å^3, 78.43Å^3 and 218.11Å^3 respectively; the surface area being 276.50Å^2, 283.48Å^2 and 671.94Å^2 respectively. The voids in solids appear to have occupied 9.53%, 9.84% and 12.58% of their respective unit cell volume. Thus, it can be inferred that cation and anion are strongly packed in the crystal structure.

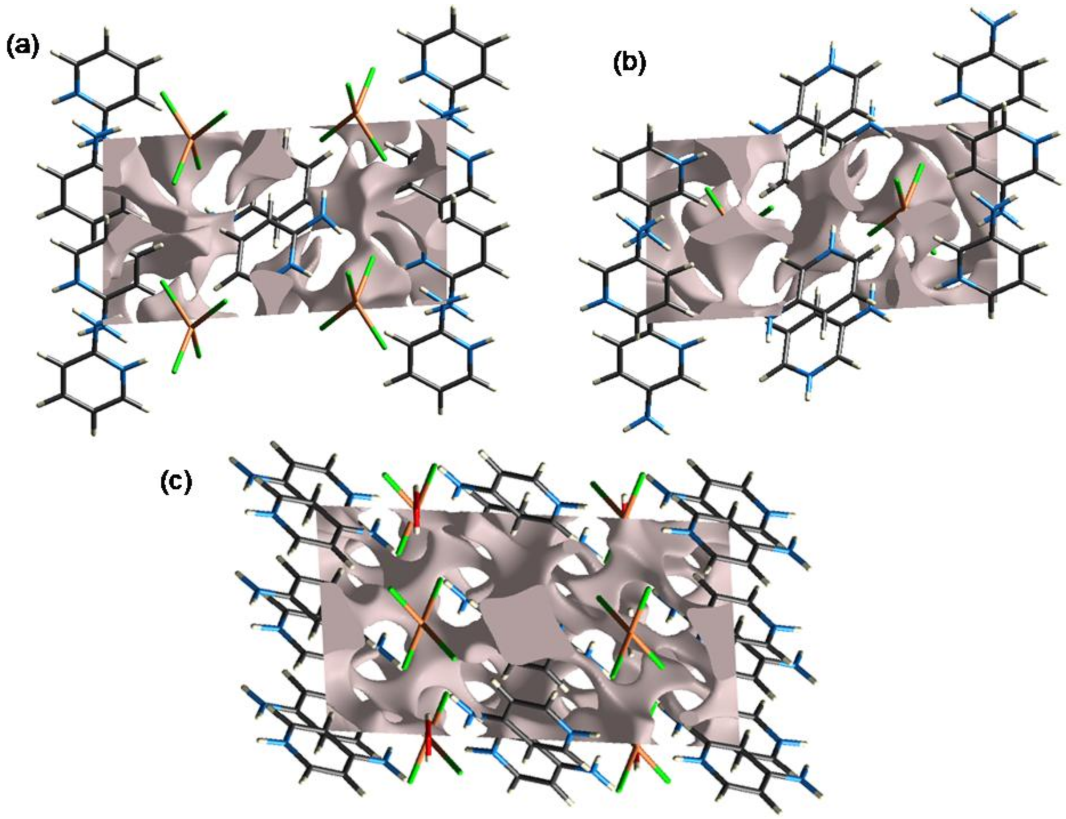

Figure IV.20 Graphical representation of void analysis along a crystallographic axis for solids (a) **6**, (b) **7** and (c) **8**.

IV.3.7 Chromotropism studies

The synthesized solids were found to exhibit chromotropic behavior particularly solvatochromism, vapochromism and thermochromism.

IV.3.7.1 Investigation of solvatochromism

The synthesized solids exhibited solvatochromism which was confirmed from the shift in absorbance peak in their electronic absorption spectra in different solvents as shown in Figure IV.21. From Figure IV.21, it was evident that **6-8** resulted in green colored solutions in polar protic solvents like water and ethanol and yellow colored solutions in polar aprotic solvents like DMF and acetone.

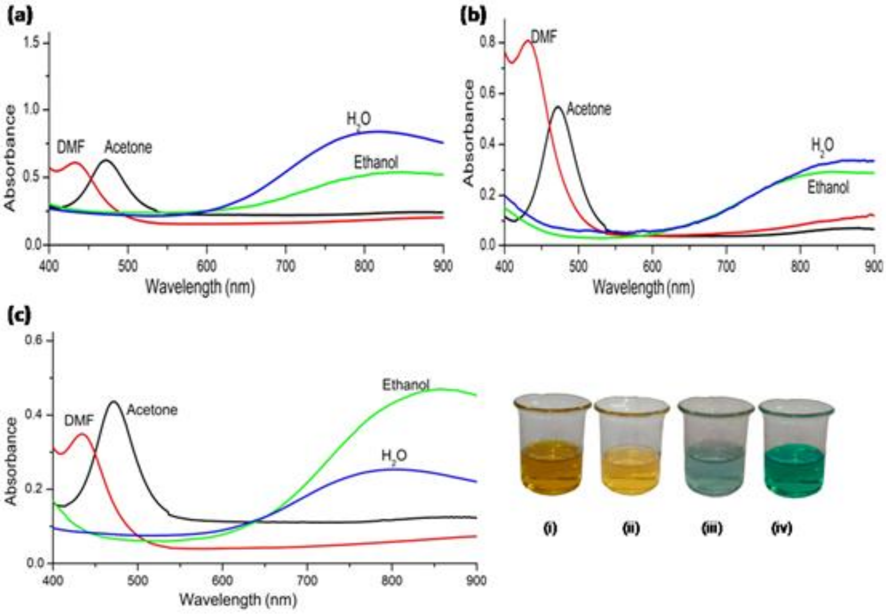

Figure IV.21 Absorption spectra of solids (a) **6**, (b) **7** and (c) **8** in different solvents. The image in the bottom right shows the color of the solids in solvents (i) DMF (ii) Acetone (iii) H_2O and (iv) Ethanol.

The UV-visible spectra of solids **6-8** exhibited similar patterns which are characteristic of $[CuCl_4]^{2-}$ species. Tetrachlorocuprates with tetrahedral symmetry exhibit ligand to metal charge transfer (LMCT) absorption bands in UV-visible region, usually ranging from 250-450 nm and weak d-d absorption bands are shifted into the near-IR region in the range 800-1400 nm [44]. LMCT absorption bands correspond to the symmetry allowed electronic transition from the ligand-localized molecular orbitals to the half-occupied d-orbital of the copper ion. The d-d absorption bands are due to symmetry forbidden electronic transition between the d-orbitals of the copper ion. In water and ethanol, a very broad d-d band was observed in the region near about 800-900 nm. The interaction of polar protic solvents with the solids results in solvation of Cu(II) ion and shows absorption maximum in the range 800-900 nm; being characteristic of copper(II) ion in a square planar structure. In DMF and acetone, bands were seen with maxima centered at

433 nm and 473 nm respectively which are the charge-transfer bands characteristic of $[CuCl_4]^{2-}$ species. Since $CuCl_4$ in DMF and acetone have no d-d transition bands below 900 nm, it can be inferred that solids retain their D_{2d} flattened tetrahedral structure in solutions of DMF and acetone. A similar observation has also been reported by Max Elleb *et.al*. [45]. Extensive hydrogen bonding interactions of solids with the solvent molecules also play a crucial role in shifting the absorption peaks.

IV.3.7.2 Investigation of vapochromism

All the solids were examined for their ability to act as vapochromic sensors and promising results were obtained. **6** and **8** and showed distinct visible color changes in presence of vapors of H_2O and NH_3 (Figure IV.22). The color change in **7** when exposed to the above vapors was not visible owing to its dark color. Vapochromic response was not observed with other volatile organic compounds like acetone, benzene, nitrobenzene, diethyl ether and phenol. **6** and **8** were found to be extremely sensitive to ammonia. They showed a change in color within 6 minutes of exposure to ammonia whereas a response time of 30 minutes was observed for water.

The solids when exposed to water showed green color and were hygroscopic. Further, the hydrated solids if left undisturbed under ambient environment for 3 days reverted back to the original state. However, the reversibility of color change occurred easily upon heating to 100°C for 12 minutes. On the other hand, **6** and **8** exposed to ammonia upon heating displayed interesting color variations. When heated at 100°C, the blue color changed to bright green. The green form when further exposed to ammonia changed to blue again which reversed to its green color upon heating. Therefore, the color change was found to be reversible. The green solid upon further heating turned black.

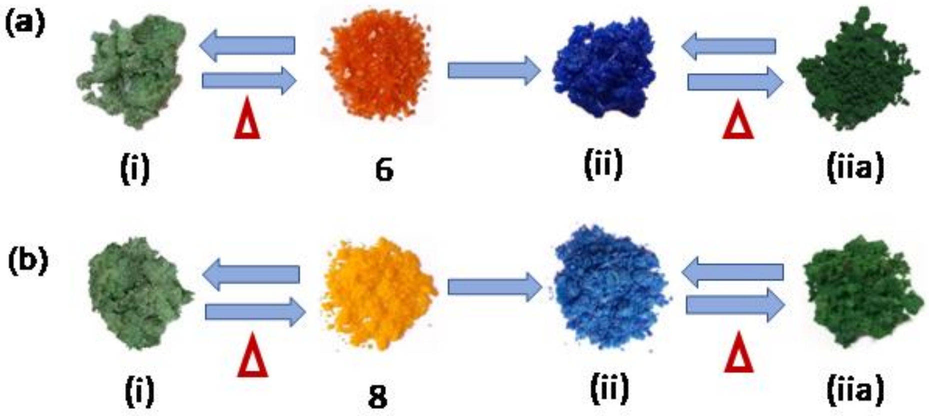

Figure IV.22 Vapochromic response of (a) **6** and (b) **8** to vapors of (i) H_2O and (ii) NH_3; (iia) shows the color change upon heating (ii).

Due to the hygroscopic nature of **6** exposed to ammonia, a detailed study of vapochromic phenomena was able to conduct only for **8** in the solid state using PXRD, UV-visible absorption spectroscopy and TGA. A comparison of PXRD pattern of the pure solid and solid **8** exposed to NH_3 vapors, showed a considerable shift in the peak positions (Figure IV.23). The alternate arrangement of tetrachlorocuprate anions and organic cations in the crystal packing apparently produces a porous structure as evident from the crystal void analysis (Figure IV.20). The void volume in solid **8** was calculated to be 218.11 Å^3 from the crystal void analysis. Incorporation of the vapors into the porous lattice plausibly perturbed the cation-anion stacking structure and caused changes in the PXRD patterns.

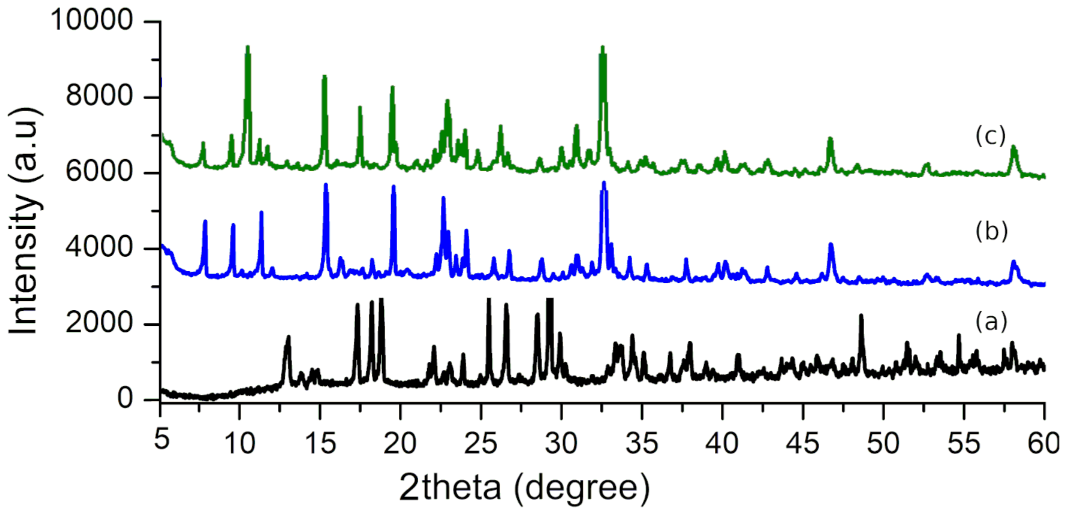

Figure IV.23 PXRD patterns of (a) **8**, (b) after exposing to NH_3 and (c) after heating.

The UV-visible absorption spectra of solid **8** exposed to NH_3 vapors also showed marked differences from the spectral pattern of the pure solid (Figure IV.24). Absorption bands of varying energies could be observed in addition to chloride-copper charge transfer bands which are due to changes in the ligand field around the metal, leading to significant changes in the d-d and/or LMCT absorption in solid **8** exposed to NH_3. The broad peak at around 650 nm can be attributed to d-d transition of Cu-ammonia complex, since peaks in the range 550-900 nm are general characteristics of $Cu(NH_3)_n{}^{2+}/Cu(NH_3)_n(H_2O)^{2+}{}_{6-n}$, n=0–4 species depending on the number of ammonia molecules involved in coordination [46]. Solid **8** exposed to NH_3 after heating (green form) also shows the absorption spectrum similar to the blue form, which indicated that there are no significant structural changes between the blue and the green forms.

The vapochromic response of **8** to NH_3vapours was further examined by TGA. Contrary to the TG curve of pure solid which shows weight loss at 100°C due to the loss of water molecule, solid **8** when exposed to ammonia showed initial weight loss at 50-70°C due to the loss of ammonia molecules (4%) incorporated in the crystal lattice. Subsequent weight loss could be attributed to the release of organic moieties and chloride ions. TGA curve of **8** exposed to NH_3 after heating was similar and also shows small weight loss at around 70°C plausibly due to adsorbed moisture (Figure IV.25).

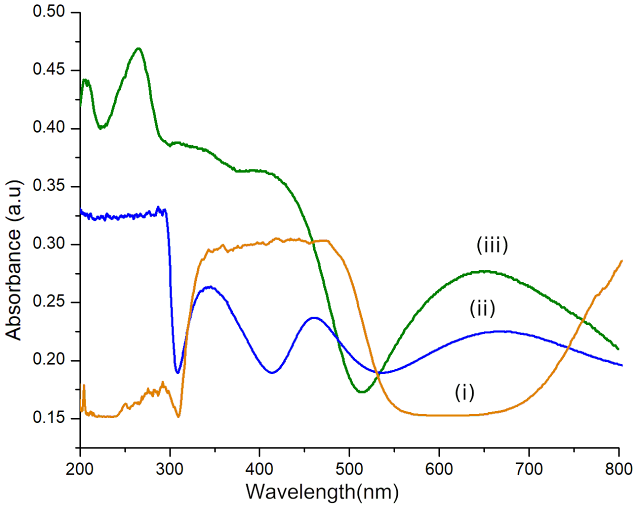

Figure IV.24 Solid state UV-Visible absorption spectra of (i) Solid **8**, (ii) **8** exposed to NH_3 and (iii) after heating.

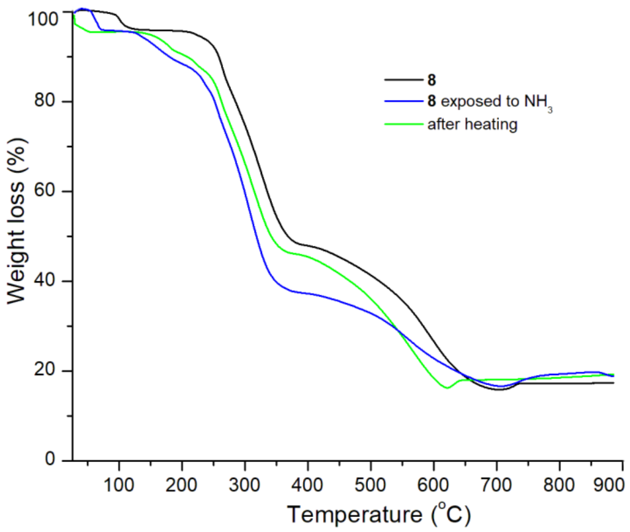

Figure IV.25 TGA curves of solid **8** exposed to NH_3vapors.

Based on the PXRD, TGA and UV-visible absorption spectra, the yellow-blue-green color variations exhibited by solid **8** when exposed to ammonia can be represented as shown in scheme IV.2.

$$\begin{tikzcd} {[(4\text{-Hampy})_2CuCl_4].H_2O} \arrow[r, "NH_3"] & {[(4\text{-Hampy})_2CuCl_4].H_2O.xNH_3} \arrow[dd, "\triangle"] \\ \text{Yellow} & \text{Blue} \\ & {[(4\text{-Hampy})_2CuCl_4].(1\text{-}y)H_2O.(x\text{-}z)NH_3 + yH_2O + zNH_3} \\ & \text{Green} \end{tikzcd}$$

Scheme IV.2 Structural changes in solid **8** when exposed to NH_3.

IV.3.7.3 Investigation of thermochromism

Among the three solids, **8** also showed thermochromism wherein it displayed a change in color from yellow to orange upon heating to 100°C due to the loss of the water of crystallization. This observation was confirmed using TGA-DTA analysis. The dehydrated form could easily reverse to the original yellow state upon cooling to room temperature (Figure IV.26).

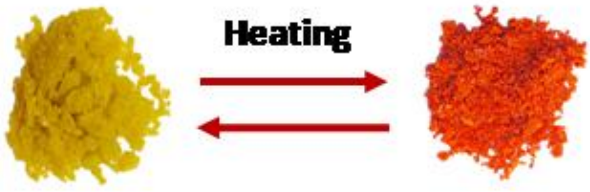

Figure IV.26 Thermochromism exhibited by **8**.

IV.4 Conclusions

In the present study, tetrachlorocuprates(II) of isomeric protonated aminopyridines were synthesized and characterized. Further the synthesized solids were examined for their ability to act as vapochromic sensors and they exhibited solvatochromism in the presence of selected solvents. **8** also exhibited reversible thermochromism. Chromotropism shown by these solids can be attributed to a synergy of various factors like changes in ligand field energy and supramolecular interactions such as hydrogen bonding. Tetrachlorocuprate(II) anions stabilized by protonated aminopyridines represent an interesting and significant class of chromogenic materials which may find applications in various fields like chemical sensors and detectors.

References

1. Golchoubian H, Mehrbanian D, Rezaee E, Xu ZX (2019) Transit Met Chem 44:671-680
2. Sone K, Fukuda Y (1987) Inorganic Thermochromism, Springer Berlin, Heidelberg
3. Liu JC, Liao WQ, Li PF, Tang YY, Chen XG, Song XJ, Zhang HY, Zhang Y, You YM, Xiong RG (2020) Angew Chem Int Ed 9:3495-3499
4. Bray KL, Drickamer HG (1990) J Phys Chem 94(5):2154-2159
5. Jaffe A, Lin Y, Mao WL, Karunadasa HI (2015) J Am Chem Soc 137(4):1673-1678
6. Dürr H, Bouas-Laurent H (2003) Photochromism: molecules and systems, Elsevier, Amsterdam
7. Riley MJ, Neill D, Bernhardt PV, Byriel KA, Kennard CHL (1998) Inorg Chem 37:3635-3639
8. Pan XW, Gang WV, Wang M, Chen HZ (2009) J Zhejiang Univ Sci A10:710-715
9. Li E, Jie K, Liu M, Sheng X, Zhua W, Huang F (2020) Chem Soc Rev 49:1517-1544
10. Hamaguchi T, Satomi N, Ando I (2018) Inorg Chim Acta 474:113-116
11. Golchoubian H, Ghorbanpour H, Rezaee E (2015) Inorg Chim Acta 442:30-36
12. Linert W, Fukuda Y, Camrad A (2001) Coord Chem Rev 218:113-152
13. Bares LA, Emerson K, Drumheller JE (1969) Inorg Chem 8:131-135
14. Steadman JP, Willett RD (1970) Inorg Chim Acta 4:367-371
15. Ferguson GL, Zaslow B (1971) Acta Crystallogr Sect B: Struct Sci Cryst Eng Mater 27:849-852
16. Anderson DN, Willett RD (1974) Inorg Chim Acta 8:167-175
17. Willet RD, Twamley B (2007) Acta Crystallogr E63:2591
18. Willett RD, Haugen JA, Lebsack J, Morrey J (1974) Inorg Chem 13(10):2510-2513
19. Harlow RL, Wells WJ, Watt GW, Simonsen SH (1974) Inorg Chem 13(9):2106-2111

20. Antolini L, Menabue L, Pellacani GC, Saladini M (1981) DaltonTrans 8:1753-1759
21. Bond MR, Johnson TJ, Willett RD (1988) Can J Chem 66:963-973
22. Battaglia LP, Corradi AB, Marcotrigiano G, Menabue L, Pellacani GC (1979) Inorg Chem18:148-152
23. Antolini L, Menabue L, Pellacani GC, Saladini M (1982) Inorg Chim Acta 58:193-200
24. Lahiry S, Sharma J, Sootha GD, Gupta HO (1978) Phys Stat Sol 46:153-162
25. Mostafa MF, Abdul-Kader MM, Arafat SS, Kandeel EM (1991) Phys Scr 43:627-629
26. Thomson RI, Rawson JM, Goeta A, Probert MR, Coome JA, Hoang TKA, Carpenter MA (2013) Mater Chem Phys 139:34-46
27. Fernández V, Doadrio JC, Granda SG, Pertierra P (1996) ActaCrystallogr Sect C: Cryst Struct Commun 52:1412-1415
28. Fernandez V, Torres MR, Tornero J (1997) Z Kristallogr NCS 212:377-378
29. Díaz I, Fernandez V, Belsky VK, Martinez JL (1999) Z Naturforsch B54:718-724
30. Haddad S, Willett RD (2001) Inorg Chem 40:2457-2460
31. Belsky VK, Fernandez V, Zavodnik VE, Diaz I, Martinez JL (2001) Crystallogr Rep 46(5):779-785
32. Bhattacharya R, Ray MS, Dey R, Righi L, Bocelli G, Ghosh A (2002) Polyhedron 21:2561-2565
33. Kelley A, Nalla S, Bond MR (2015) Acta Crystallogr Sect B: Struct Sci Cryst Eng Mater B71:48-60
34. Jaffe A, Karunadasa HI (2014) Inorg Chem 53(13):6494-6496
35. Mande HM, Ghalsasi PS, Navamoney A (2015) Polyhedron 91:141-149
36. Vishwakarma AK, Kumari R, Ghalsasi PS, Navamoney A (2017) J Mol Struct 1141:93-98

37. Kumar DK, Ballabh A, Jose DA, Dastidar P, Das A (2005) Cryst Growth Des 5(2):651-660
38. Halvorson KE, Patterson C, Willett RD (1990) Acta Cryst B46:508-519
39. Rietveld HM (1966) Acta Crystallogr 20:508-513
40. Spackman PR, Turner MJ, McKinnon JJ, Wolff SK, Grimwood DJ, Jayatilaka D, Spackman MA (2021) J Appl Cryst 54:1006-1011
41. Nakamoto K (1978) Infrared and Raman spectra of inorganic and coordination compounds, John Wiley & Sons, New York
42. Xiao F, Landee CP, Turnbull M, Wikaira JL (2019) Eur Chem Bull 8:239-243
43. Li L, Turnbull MM, Landee CP, Jornet J, Deumal M, Novoa J, Wikaira JL (2007) Inorg Chem 46:11254-11265
44. Willett RD, Liles OL Jr, Michelson C (1967) Inorg Chem 6(10):1885-1889
45. Elleb M, Meullemeestre J, Schwing-Weill MJ, Vierling F (1980) Inorg Chem 19:2699-2704
46. Trevani LN, Roberts JC, Tremaine PR (2001) J Solut Chem 30(7):585-622

Chapter V

Surfactant templated nanostructured phosphomolybdates

Summary

In this chapter, nanostructured phosphomolybdate solid templated by a cationic surfactant, cetyltrimethylammonium bromide (CTAB) was synthesized and characterized by PXRD, FTIR, FESEM and EDAX analysis. The thermal stability of the solid was established using TGA. Further, the potential of the synthesized solid in removing cationic and anionic dyes form aqueous solution was investigated and it was found that the solid had high adsorption capacity for removing cationic dyes. Langmuir and Freundlich isotherm models were applied to the experimental data to find the suitable model for describing the adsorption equilibrium. The adsorption kinetics were also evaluated using pseudo-first order, pseudo-second order and intra-particle diffusion models.

V.1 Introduction

Pollution is one of the major global concerns and has serious consequences on the environment, human health, and the planet as a whole. In particular, pollution due to dyes is a significant environmental issue that affects the air, water, and soil in several parts of the world [1]. Dyes are used in a variety of industries, including textiles, leather, printing and cosmetics, to produce bright and vibrant colors. However, the release of dye effluent from factories is often discharged directly into rivers and lakes, contaminating these water bodies and making them toxic to aquatic life. In addition, dyes can bind to organic matter and sediments, causing them to sink to the bottom of water bodies and suffocating plant and animal life. This not only affects the immediate area, but also has wider implications for the entire ecosystem, as the food chain is disrupted and toxic substances are spread through the water [2,3]. Therefore, it is important to prevent or minimize the release of harmful dyes to protect the balance and tranquilly of the environment, particularly of aquatic ecosystems.

Researchers from all over the world have made significant attempts to regulate water pollution, and a number of approaches have been suggested in literature. Some of these include coagulation, ion-exchange, photocatalysis, solvent extraction, chemical oxidation, adsorption, electrolysis, etc. [4-8]. Because of its convenience, ease of use, and simplicity of design, the adsorption process is preferred above other techniques currently available for controlling water pollution [9]. Adsorbents that are commonly used to treat dye contaminated water include zeolites [10], activated carbon [11], agro waste [12], clay [13], etc. However, these materials have poor selectivity and limited adsorption capacity. Hence, developing more suitable and efficient materials for removing dyes is vital. In this regard, surfactant templated polyoxometalate (POM) hybrid solids have been explored as novel adsorbents for removal of dye by a few researchers. For instance, Yao *et.al.* has reported a Keggin type POM *viz.* decamolybdodivanadophosphate ($H_5[PV_2Mo_{10}O_{40}]$) encapsulated by a cationic surfactant dimethyldioctadecylammonium bromide as an efficient adsorbent for removal of Reactive black 5 dye [14].

Therefore, in this chapter, an attempt was made to synthesize phosphomolybdate (a POM) solid templated by a cationic surfactant *viz.* cetyltrimethylammonium bromide (CTAB) and investigate its potential as an adsorbent for removing cationic and anionic dyes from aqueous solution. The effect of adsorbent dosage, contact time and initial dye concentration on the removal efficiency was studied. In addition, various isotherm and kinetic models were also investigated in order to better understand the adsorption behavior. The results are significant as most of the works on surfactant-POM hybrids is limited to structural studies and only a few examples of their potential use as catalytic materials, pH probes and electro/photochromic properties have been reported [15-17]. These materials also offer a way to investigate the self-assembly behaviour of phosphomolybdate (PMO) hybrid solids [18-22]. Surfactants can act as an ideal structure-directing agent for forming lamellar type PMOs via self-assembly approach [23,24]. In addition, the morphology and properties of surfactant-PMO solids can be tuned by varying the chain length, size and shape of the surfactant molecules resulting in amorphous or crystalline solids ranging from nano to micro dimensions [25-27].

V.2 Experimental

V.2.1 Synthesis of CTAB templated phosphomolybdates

The synthesis was carried out similar to the procedure reported by Thomas.*et.al.*[22]. Initially two different solutions were prepared. Solution A was prepared by dissolving $Na_2MoO_4{\cdot}2H_2O$ (0.30 g, 1.25 mmol) in 20 mL of water. Solution B was prepared by dissolving CTAB (0.08 g, 0.31 mmol) in 10 mL of water. Subsequently, solution A was added slowly to solution B with vigorous stirring, followed by adding 1M H_3PO_4

dropwise till the pH of the solution was ~1. Immediately, white precipitate was formed which gradually turned to yellow after stirring for 24 hours. Thereafter, it was left undisturbed for two days. Finally, a yellow-colored precipitate was obtained. It was washed with water and ethanol and dried in air. Scheme V.1 shows the experimental procedure for synthesis.

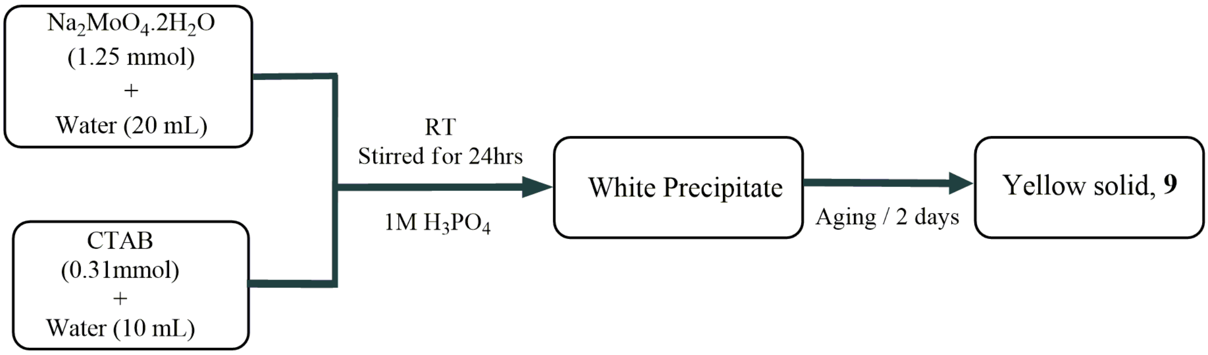

Scheme V.1 Synthetic procedure for preparing CTAB templated phosphomolybdates.

V.2.2 Preparation of dye stock solutions

A stock solution (50 ppm) of methylene blue (MB), malachite green (MG), methyl orange (MO) and eosin Y (EY) was prepared by dissolving 50mg of it in 1L of distilled water. The stock solution was diluted for further studies.

V.2.3 Dye removal studies

A series of batch adsorption experiments were conducted to determine the adsorption of dyes on the PMO solid, **9**. All the batch adsorption experiments were performed on a magnetic stirrer using 100 mL beaker containing 25mL each of dye solutions of pH 7.0±0.1. Experiments were performed at 27°C (300 K). All solution samples post adsorption were filtered through Whatman No:1 filter paper. The concentrations of dye in treated samples were determined by measuring the absorbance using UV-visible spectrophotometer (Shimadzu UV-1800).

The amount of dye adsorbed per unit mass of the adsorbent was evaluated by using the following equation,

$$Qt = \frac{C_0 - C_t}{M} \times V$$

where,

C_0 = Initial concentration of dye (mg/L)

C_t = Liquid phase concentration of dye at any time (mg/L)

V = Volume of dye took for adsorption, in ml

M = Weight of adsorbent dose, in g.

The percentage of dye removed was calculated by the following equation,

$$\% \text{ Removal} = \frac{(C_o - C_t)}{C_o} \times 100$$

V.2.4 Modeling of adsorption isotherms and its studies

In order to optimize the design of a sorption system to remove dyes from aqueous solutions, it is important to establish the most appropriate correlations for the equilibrium curves. The Langmuir and Freundlich isotherms are widely applied to adsorption processes.

(a) Langmuir isotherm

The most widely used isotherm equation for modeling of the adsorption data is the Langmuir equation, which is valid for monolayer sorption onto a surface with a finite number of identical sites and is given by following equation,

$$q_e = \frac{\mathrm{Qmax}\ b_L\ \mathrm{Ce}}{1+b_L\ \mathrm{Ce}}$$

For solid - liquid systems, the Langmuir isotherm is expressed in the linear form as [28]:

$$\frac{\mathrm{Ce}}{\mathrm{qe}} = \frac{1}{\mathrm{Qmax}\ \mathrm{bL}} + \frac{\mathrm{Ce}}{\mathrm{Qmax}}$$

where,

q_e = The amount of dye adsorbed per gram of the adsorbent at equilibrium

Q_{max} = monolayer adsorption capacity, (mg/g), signifies the solid phase concentration, corresponding to the complete coverage of available sorption site, can be evaluated from the slope of Langmuir isotherm plot (Ce/qe against Ce)

C_e = The equilibrium concentration of adsorbate (mg/L)

b_L = Langmuir Isotherm constant (L/g). This value corresponds to energy of sorption, calculated from the intercept of the linear plot of Langmuir isotherm.

The best-fit equilibrium model was determined based on the linear squared regression correlation coefficient R^2. The dimensionless separation factor R_L describes the type of isotherms and is defined by,

$$R_L = \frac{1}{1+\mathrm{bCo}}$$

where,

b is Langmuir constant

C_o is the adsorbate initial concentration.

The parameters indicate the shape of the isotherm accordingly, if, R_L value lies in between 1 to 0, then favorable adsorption indicated. If, R_L value greater than 1, unfavorable adsorption, while a value of 1 represents linear & unfavorable and 0 represents irreversible.

(b) Freundlich isotherm

The Freundlich isotherm model is derived by assuming a heterogeneous surface with a non-uniform distribution of heat of adsorption over the surface, the Freundlich model in non-linear & linear form can be expressed as [29],

$$q_e = \;= K_F\,(Ce)^{1/n}$$

$$\log q_e = \log K_F + \frac{1}{n}\log Ce$$

where,

K_F is the Freundlich characteristics constant and 1/n the heterogeneity factor of adsorption, obtained from intercept and slope of $\ln(q_e)$ vs $\ln(C_e)$ linear plot respectively.

K_F and n are the physical constants of Freundlich adsorption isotherm which indicate the adsorption capacity and adsorption intensity, respectively.

If n =1, then the partition between the two phases is independent of the concentration. 1/n <1 indicate normal adsorption, 1/n >1 indicate cooperative adsorption and 1/n =1 is the linear adsorption isotherm.

V.2.5 Adsorption Dynamics

Kinetics is of great significance to evaluate the performance of a given adsorbent and gain insight into the underlying mechanisms. Solute uptake rate determines the residence time required for completing the adsorption reaction and can be enumerated from kinetic analysis. The kinetics of sorption that defines the efficiency of sorption of Methylene Blue dye was checked by the pseudo-first order, pseudo-second order and intra-particle diffusion models.

(a) Pseudo-First Order Model

The pseudo-first order rate expression of Lagergren model is generally expressed as follows [30]:

$$\frac{dq}{dt} = k_1 (q_e - q)$$

where,

q_e and q are the amounts of adsorbed dye (mg/g) onto the adsorbent at equilibrium and at time t (min), respectively

k_1 is the rate constant of first-order adsorption.

The linear form of the above equation can be obtained as:

$$\log (q_e - q) = \log q_e - k_1 \left(\frac{t}{2.303} \right)$$

The plot of $\log(q_e\text{-}q)$ against t for the pseudo-first order equation gives a linear relationship and k_1 and q_e values can be determined from the slope and intercept of this equation, respectively.

(b) Pseudo-Second Order Model

The differential form of the pseudo-second order equation can be represented as [31]:

$$\frac{dqt}{dt} = K_2 (q_e - q_t)^2$$

where,

K_2 is the pseudo-second order rate constant (g/mg/min).

The linear form of the above equation can be obtained by integration of the equation for the boundary conditions $q_t = 0$ at t=0 and $q_t = q_t$ at t=t,

$$\frac{t}{q_t} = \frac{1}{K_2 qe^2} + \frac{t}{q_e}$$

A plot of $t/q_{t\ \mathrm{versus}}$ t gives a straight line with slope $1/q_e$ and intercepts $1/k_2 q_e$.

The initial Sorption rate, h (mg/g.min), at t ⟶0 is defined as:

$h = K_2 q_e^2$

(c) Intra-particle Diffusion Model

The intra-particle diffusion model was proposed by Weber and Morris to identify the diffusion mechanism of the adsorption process [32]. Intra-particle diffusion is a transport process involving movement of species from the bulk of the solution to the solid phase. A plot of the amount of sorbate adsorbed, q_t (mg/g) and the square root of the time, gives the rate constant (slope of the plot). It is calculated by using the intra-particle diffusion model [32] given as,

$$q_t = K_{diff}\, t^{1/2} + C$$

where,

q_t is the amount of dye adsorbed (mg/g) at time t.

C is the boundary layer thickness

K_{diff} is the intra-particle diffusion rate constant (mg/g/min)

The plot of the amount dye adsorbed, q_t versus $t^{1/2}$ will give a straight line with a slope of K_{diff} and an intercept of C.

V.3 Characterization

The synthesized CTAB templated PMO nanoparticles, **9** were characterized by techniques namely PXRD, FTIR and TGA as discussed under Section II.2.3 in chapter II. Field emission scanning electron microscopy studies (FESEM) and Energy dispersive X-ray analysis (EDAX) were carried out using Gemini SEM 300 (Carl Zeiss).

V.4 Results and Discussion

V.4.1 Characterization of CTAB templated PMO nanoparticles, 9

The PXRD pattern of **9** (Figure V.1a) showed broad *00l* reflections which indicated lamellar characteristics, with a d-spacing ~ 3.5 nm. FTIR of the synthesized PMO solid showed the presence of strong bands around 1068 cm^{-1} due to PO_4 groups, peaks around 881 and 613 cm^{-1} were attributed to Mo=O and Mo-O vibrations. Two absorption peaks at 2926 and 2850 cm^{-1} corresponded to the C-H stretching vibrations of methyl and methylene groups of CTAB. Peak at 1473 cm^{-1} were attributed to C-H bending vibrations of CTAB moiety as shown in Figure V.1b. The morphology and composition of the synthesized PMO solid was analyzed using FESEM and EDAX analysis. FESEM images indicated a spherical morphology with particle size varying from 78 to 167 nm (Figure V.2a). EDAX spectrum showed the peaks corresponding to carbon, nitrogen, phosphorus, molybdenum and oxygen (Figure V.2b). TGA showed weight loss in the temperature region 290-400°C due to the decomposition of CTAB moieties incorporated in the Mo-O-P framework. The amount of CTAB present in the sample was estimated to be ~ 30%. The second weight loss occurred after 400°C due to the decomposition of the phosphomolybdate anion and a residual mass of 55% was obtained at 800°C. On the basis of TGA and EDAX, the composition was found to be (CTAB)$PMoO_6$.

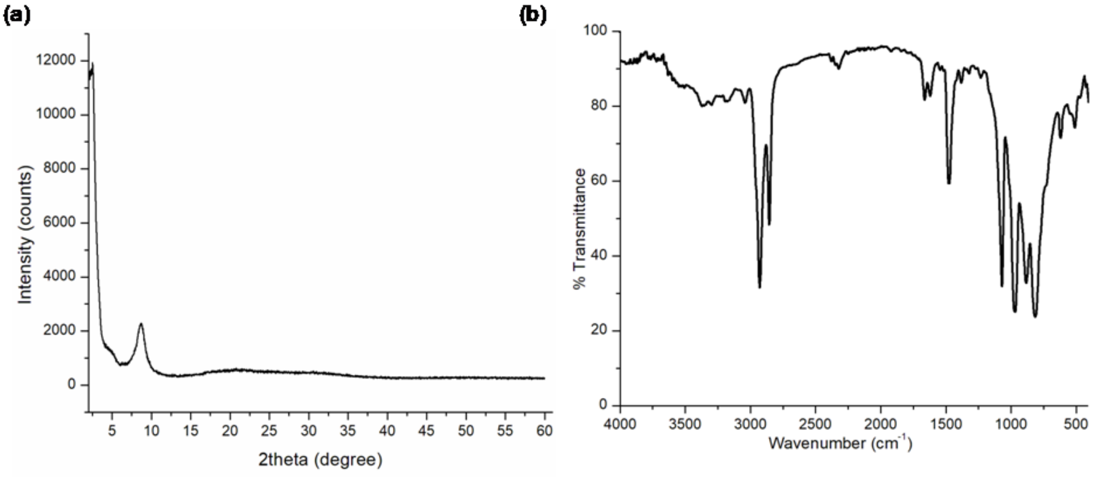

Figure V.1 (a) PXRD and (b) FTIR of solid **9**.

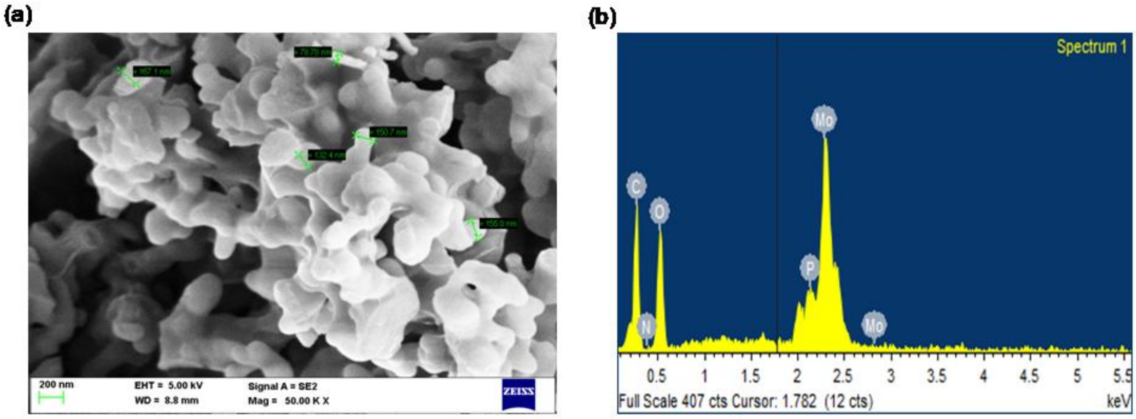

Figure V.2 (a) FESEM and (b) EDAX spectrum of solid **9**.

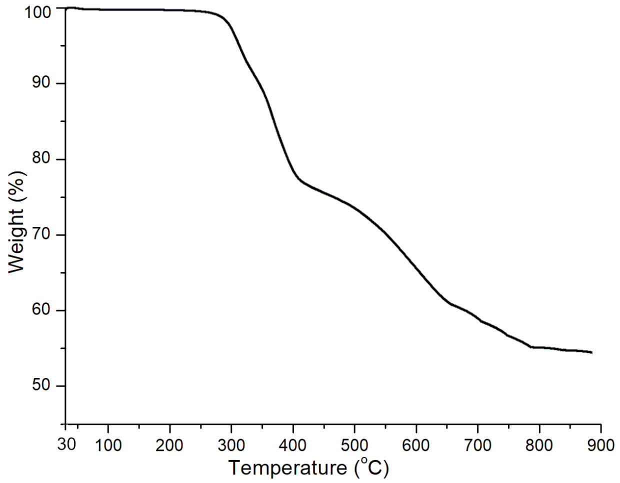

Figure V.3 TGA plot of solid **9**.

V.4.2 Dye removal studies

The dye adsorption behavior of **9** was investigated by using methylene blue (MB) as the model dye. It was observed that **9** could effectively remove MB from the aqueous solution as shown in Figure V.4. The effect of various parameters such as adsorbent dosage, contact time, initial dye concentration and reusability of **9** for the removal of MB was further investigated. The nature of dye was also examined by using other dyes.

V.4.2.1 Effect of adsorbent dosage

The effect of adsorbent dosage was studied by varying the amount of **9** from 0.02 to 0.1g for the removal of MB dye. 25 mL of 5 ppm MB solutions containing varying amounts of adsorbents were stirred for 20 minutes. From Figure V.5, it can be inferred that an increase in the amount of solid **9**, more dye moieties could be removed from dye contaminated water. The maximum removal efficiency was observed with a dosage of 0.1g of **9**. A further increase in the amount of **9** showed no significant increase in the dye removal.

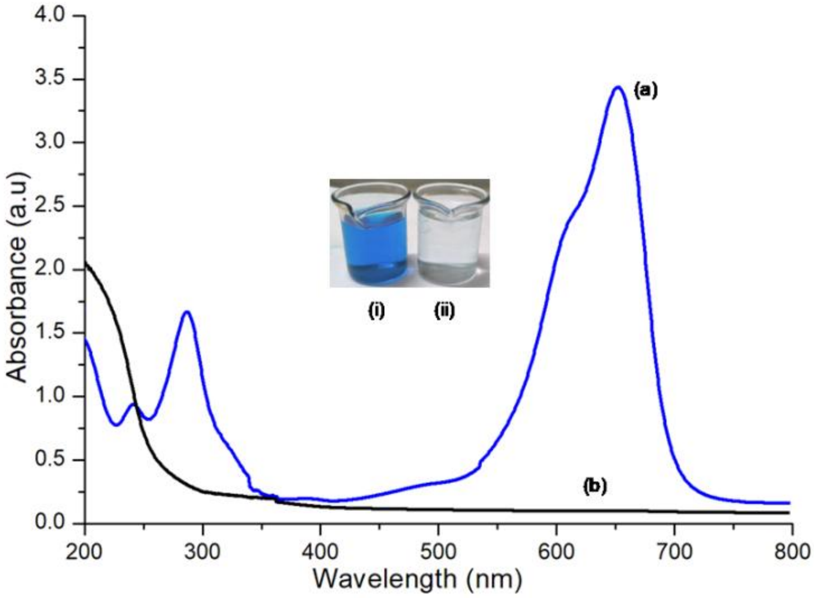

Figure V.4 UV-Visible spectra of (a) solution of 5ppm MB and (b) MB solution obtained after treatment with **9** for 1 hour. Figures in the inset represent (i) the original solution of MB and (ii) MB solution obtained after treatment with **9** for 1 hour.

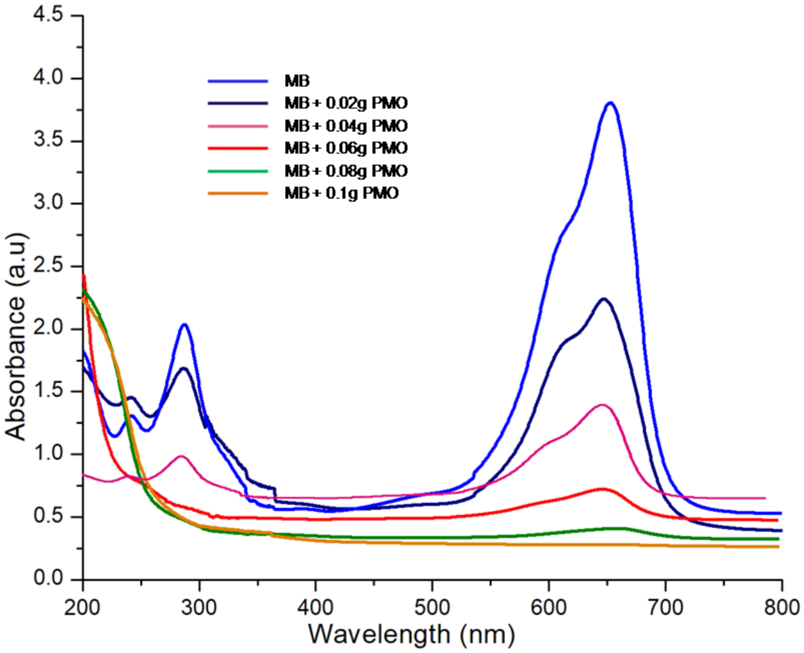

Figure V.5 UV-visible absorption spectra of MB (5 ppm, 25 mL) solution showing the effect of dose on dye removal upon stirring for 20 minutes.

V.4.2.2 Effect of contact time

The effect of contact time on the dye removal efficiency was also investigated using 25 mL of 5 ppm MB solution containing 0.1g of **9**. The solution was stirred and absorbance was measured at regular time intervals (10, 20, 30, 40, 50 and 60 minutes). Figure V.6 shows the effect of contact time with respect to MB removal efficiency. From the figure it can be observed that MB removal increased with increase in time and a maximum removal was achieved at 40 minutes of stirring. After 40 minutes, the efficiency of adsorption process did not change significantly, which could indicate the equilibrium adsorption of the MB dye. Therefore, the equilibrium time for the MB dye adsorption process was found to be 40 minutes.

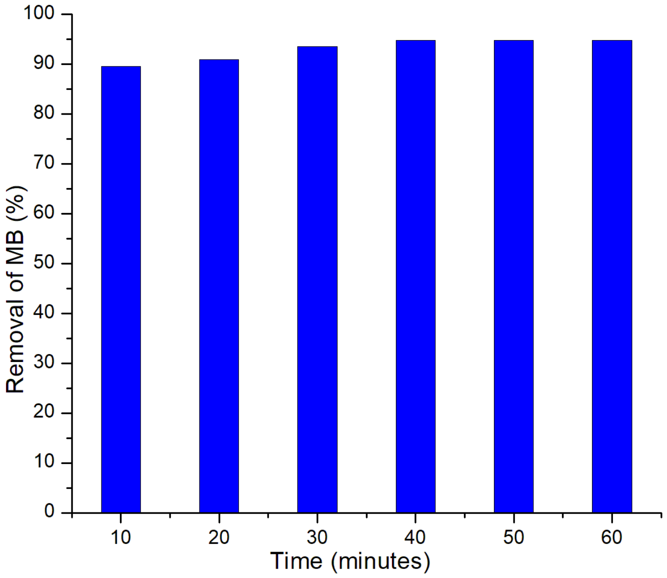

Figure V.6 Effect of contact time on MB dye removal by **9**.

V.4.2.2 Effect of initial dye concentration

The initial concentration of dye has a significant impact on the adsorption process since it provides the necessary driving force for mass transfer between the aqueous phase (aqueous solution containing dye) and the solid phase (adsorbent). Hence, the effect of initial concentration of MB on the adsorption process was studied by varying the concentration of MB. Figure V.7 shows the effect of the initial concentration of MB dye in the range of 3–8 ppm on the efficiency of dye removal at a PMO dosage of 0.1g and contact time of 40 minutes. It was observed that the percentage removal of dye sharply increased from 77% to 95% on increasing the initial dye concentration from 3ppm to 5 ppm. Further increase in the MB dye concentration caused a decrease in the adsorption efficiency as seen in Figure V.7. An increase in the removal efficiency at low concentrations of dye solution could be due to the greater interaction of dye molecules with the surface and active sites in the solid, **9**. However, a decrease in the dye removal efficiency at high dye concentrations could be attributed to the saturation of active sites in the solid, **9** at high concentrations of MB solution.

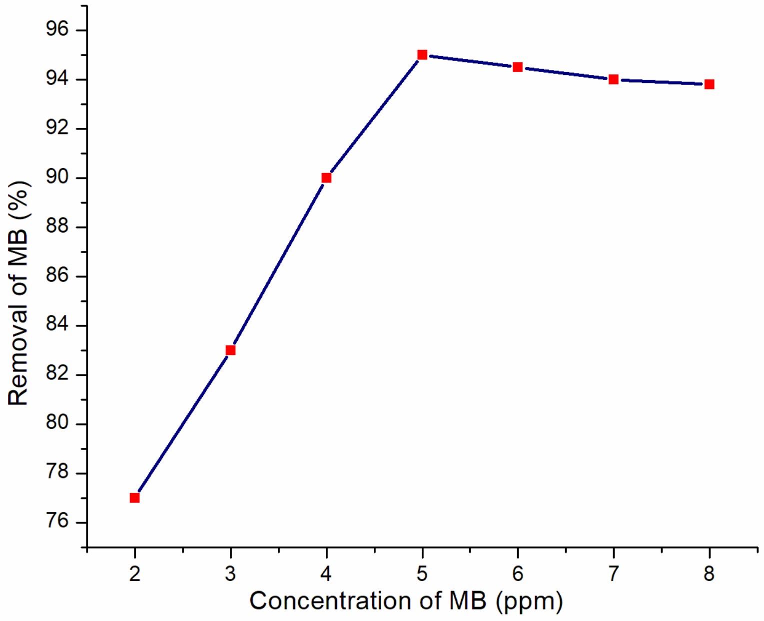

Figure V.7 Effect of initial concentration of MB on the adsorption process.

V.4.2.3 Effect of the nature of dye

Apart from MB dye, the effectiveness of **9** in removing other dyes viz; malachite green (MB), methyl orange (MO) and eosin Y (EY) was also examined for a clear insight of the adsorption mechanism. 0.1g of adsorbent was added to each of the dye solutions (25 mL, 5 ppm) and stirred for 40 minutes. The initial and final absorbance was measured using UV-visible spectrophotometer. Figure V.8 shows the absorption spectra of dyes before and after treating with **9**. It was observed that **9** could effectively remove malachite green (MG) similar to that of MB. On the other hand, the absorption spectra of anionic dyes viz; MO and EY after treating with **9** did not show any significant decrease in its intensity as observed in Figure V.8. Hence, it can be inferred that the synthesized solid, **9** was more effective in removing only the cationic dyes.

V.4.2.3 Reusability of CTAB-PMO solid

One of the crucial factors in the wastewater treatment process is the adsorbent's capacity to be reused and recovered. Solid **9** after treatment with the MB dye solution was filtered, washed with water and air dried. It was then retested for its adsorption efficiency in removing MB dye solution upto 10 cycles. Figure V.9 shows that there is no decrease in the percentage of removal of MB upto 6 consecutive cycles. However, a decrease in the percentage of removal of dye was observed in later cycles.

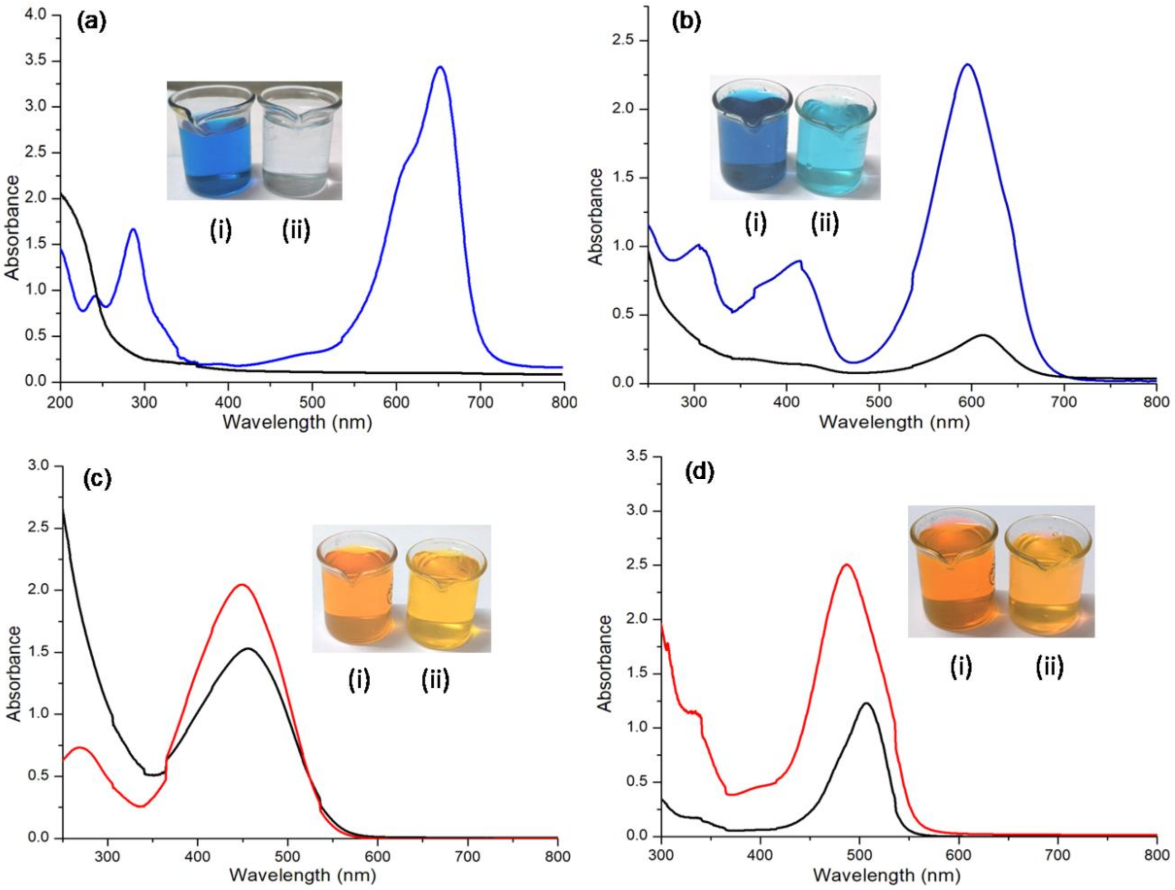

Figure V.8 UV-Visible spectra of 5ppm dye solutions (a) MB, (b) MG, (c) MO and (d) EY before (colored curve) and after (black curve) treating with 0.1g of **9**. Image in the inset represents (i) the original dye solution and (ii) dye solution obtained after treatment with **9** for 40 minutes.

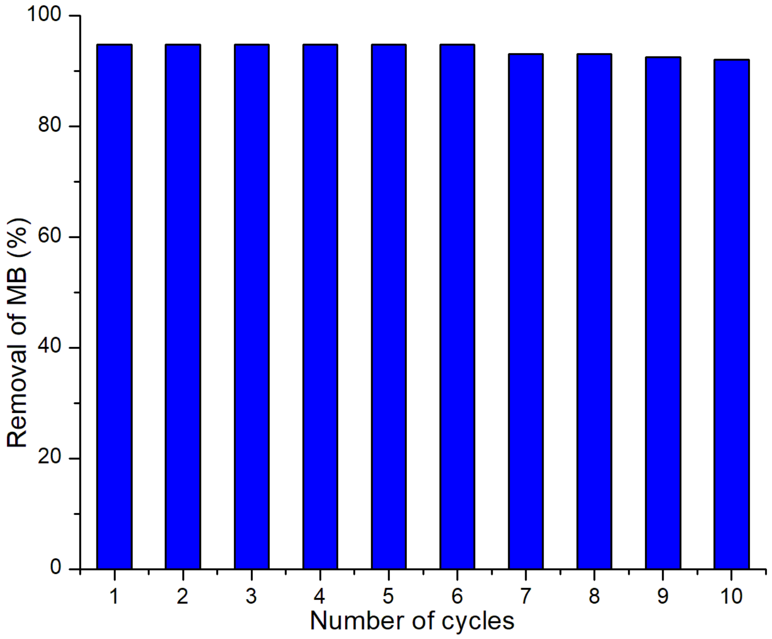

Figure V.9 Reusability of **9** on MB removal (25mL, 5 ppm MB solution with 0.1g **9**, stirred for 40 minutes).

V.4.3 Adsorption isotherms

Adsorption isotherms provide information on the amount of dye adsorbed onto the surface of the adsorbent, the adsorption capacity, multilayer or monolayer formation, and type of interaction in between the adsorbate and adsorbent. Therefore, in this study, Langmuir and Freundlich isotherms have been applied to evaluate the adsorption capacity of the CTAB-PMO solid.

V.4.3.1 Langmuir isotherm

Langmuir isotherm model predicts monolayer coverage of the adsorbate on the outer surface of the adsorbent [33]. The applicability of the Langmuir model was evaluated from the plot of C_e/q_e against equilibrium concentration, C_e for MB (Figure V.10). Q_{max} and Langmuir isotherm constant, b was evaluated from the slope and the intercept of the plot. Langmuir isotherm parameters obtained from the respective linear plot (Figure

V.10) and correlation coefficient are presented in Table V.1. The value of R^2 was only 0.703 which indicated that adsorption process does not follow Langmuir isotherm model and also the adsorption was not limited to monolayer coverage.

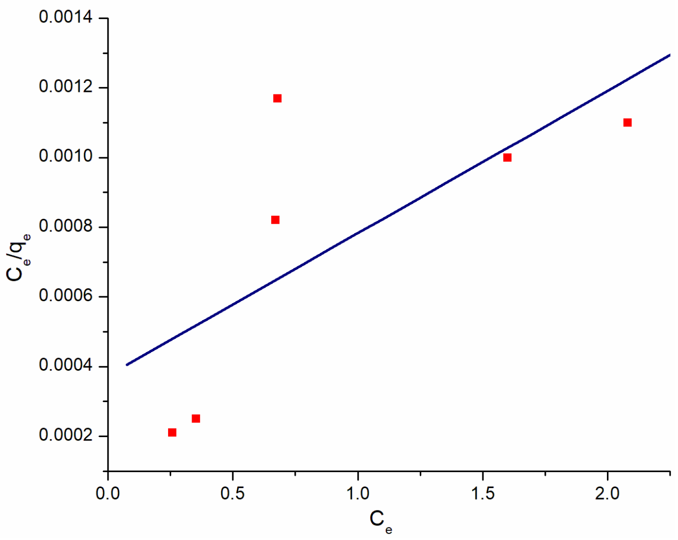

Figure V.10 Langmuir isotherm plot of dye adsorption on **9** at room temperature (adsorbent dosage = 0.1g, stirring time = 40 minutes).

Table V.1 Langmuir isotherm parameters of dye adsorption on **9**.

Q_{max} (mg/g)	R_L	Langmuir constant (b) (L/mg)	R^2
244.6	0.179	0.00914	0.703

V.4.3.2 Freundlich isotherm

The applicability of the Freundlich isotherm model was studied by plotting log q_e against log C_e which gave a straight line as shown in Figure V.11. The slope and the intercept of the plot gave the value of 1/n and K_f and are tabulated in Table V.2. Freundlich isotherm provided better regression analysis with $R^2 = 0.992$ (Table V.2) than Langmuir model ($R^2 = 0.703$). The value of n also indicated a heterogeneous nature of the surface. Therefore, it can be inferred that adsorption of MB onto surface of **9** corresponds to multilayered heterogeneous adsorption.

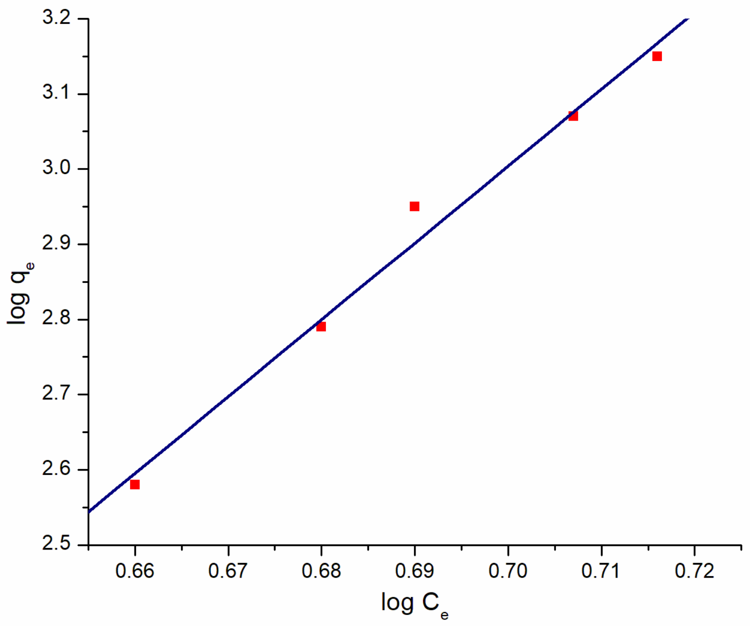

Figure V.11 Freundlich isotherm plot of dye adsorption on **9** at room temperature (adsorbent dosage = 0.1g, stirring time = 40 minutes).

Table V.2 Freundlich isotherm parameters of dye adsorption on **9**.

K_f	n	R^2
0.0071	0.097	0.992

V.4.4 Adsorption kinetics

The adsorption kinetics of MB removal was studied using the pseudo first-order, pseudo second-order and intra-particle diffusion models.

V.4.4.1 Pseudo first-order model

The values of ln $(q_e\text{-}q_t)$ were linearly correlated with t from which k_1 and predicted q_e can be calculated using the slope and intercept of the plot. Figure V.12 represents the pseudo-first order kinetic plot for MB adsorption by solid, **9**. The kinetic parameters obtained for the adsorption of MB on **9** have been listed in Table V.3.

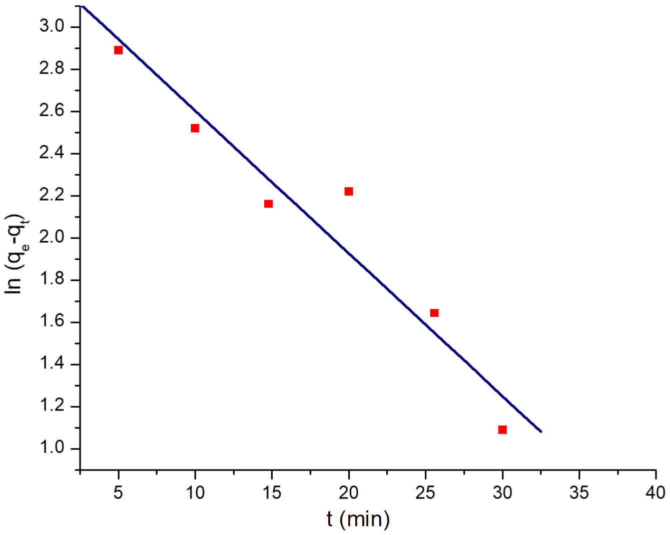

Figure V.12 The pseudo-first order kinetic model for MB adsorption by **9** (25 mL of 5 ppm MB, adsorbent dosage = 0.1g, stirring time = 40 minutes).

Table V.3 Kinetics constants and parameters determined using pseudo first-order model for the adsorption process.

K_1 (min^{-1})	q_e (graph) (mg/g)	q_e (exp) (mg/g)	R^2
0.0676	26.56	228	0.965

The value of the correlation coefficient, R^2 was 0.965 (Table V.3) and the calculated q_e value obtained from the graph (Figure V.12) was very low when compared with the experimental q_e value. Hence, it can be inferred that the MB adsorption by **9** did not adhere to the pseudo-first order kinetic model.

V.4.4.2 Pseudo second-order model

The pseudo second-order kinetics were studied by plotting t/q_t versus t which gave a straight line with slope 1/q_e and intercept 1/k_2q_e. Figure V.13 represents the pseudo second-order kinetic plot for MB adsorption by solid, **9**. The kinetic parameters obtained from the plot have been listed in Table V.4.

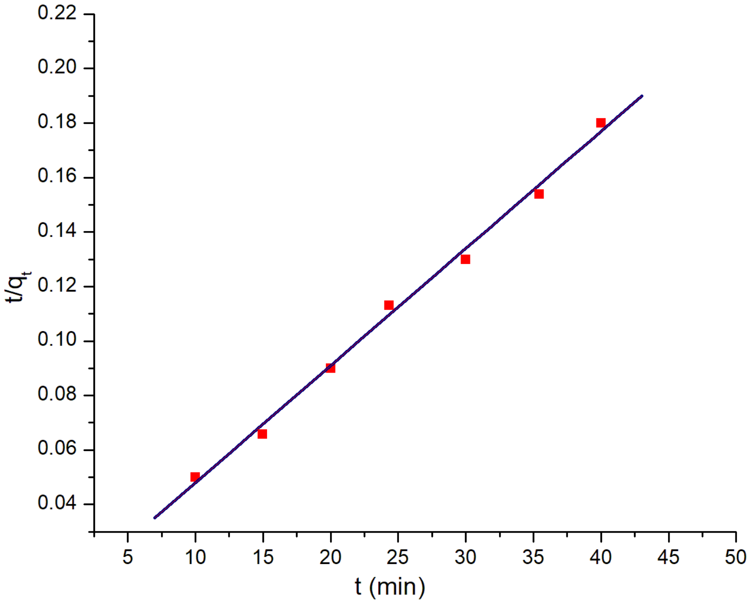

Figure V.13 The pseudo- second order kinetic model for MB adsorption by PMO solid (25 mL of 5 ppm MB and PMO dosage = 0.1g).

Table V.4 Kinetics constants and parameters determined using pseudo-second order model for the adsorption process.

K_2 (g/mg/min)	q_e (graph) (mg/g)	q_e (exp) (mg/g)	R^2
0.860	232	228	0.996

Table V.4 shows that the experimental and calculated q_e values were comparable. Moreover, the value of the correlation coefficient is nearly unity (R^2 = 0.99). Therefore, it can be concluded that kinetic mechanism of MB adsorption by **9** follows the pseudo-second-order model.

V.4.4.3 Intra-particle diffusion model

The applicability of the intra-particle diffusion model on the adsorption of MB by **9** was evaluated by plotting a graph between q_t and the square root of time ($t^{1/2}$) as shown in Figure V.14. K_{diff} (mg g^{-1} $min^{-1/2}$) is the rate constant of the intra-particle diffusion obtained from the slope and C (mg g^{-1}) is constant found from the intercept of the plot drawn between q_t and $t^{1/2}$. Table V.5 shows the values of kinetic constants and parameters determined using intra-particle diffusion plot.

Table V.5 Kinetics constants and parameters determined using intra-particle diffusion model for the adsorption process.

K_{diff} (mg g^{-1} $min^{-1/2}$)	C (mg g^{-1})	R^2
3.536	204.37	0.970

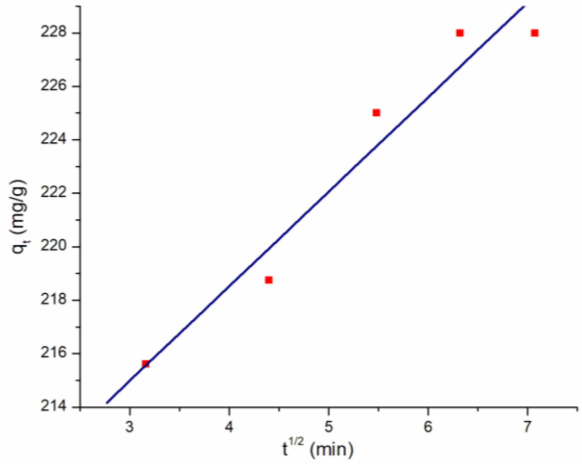

Figure V.14 The intra-particle diffusion model for MB adsorption by PMO solid (25 mL of 5 ppm MB and PMO dosage = 0.1g).

According to this model, the intra-particle diffusion is the rate-limiting step when the plot passes through the origin (as C equals to zero) [32]. As shown in Figure V.14, q_t versus $t^{1/2}$ resulted in a linear plot and regression analysis showed the value of correlation coefficient, $R^2 = 0.97$ (Table V.5). However, the plot did not pass through the origin indicating that the adsorption of MB onto **9** was not diffusion controlled.

V.4.5 Mechanism

Based on the experimental results, it seems that the fundamental mechanism of adsorption of dyes by solid **9** involves electrostatic interactions. Cationic dyes such as MB and MG could be strongly adsorbed onto the negatively charged surface of solid **9** via electrostatic attraction. A schematic representation of adsorption of MB by solid **9** is shown in figure V.15. However, repulsive electrostatic interactions become dominant between anionic dyes and solid **9**, which resulted in their poor adsorption.

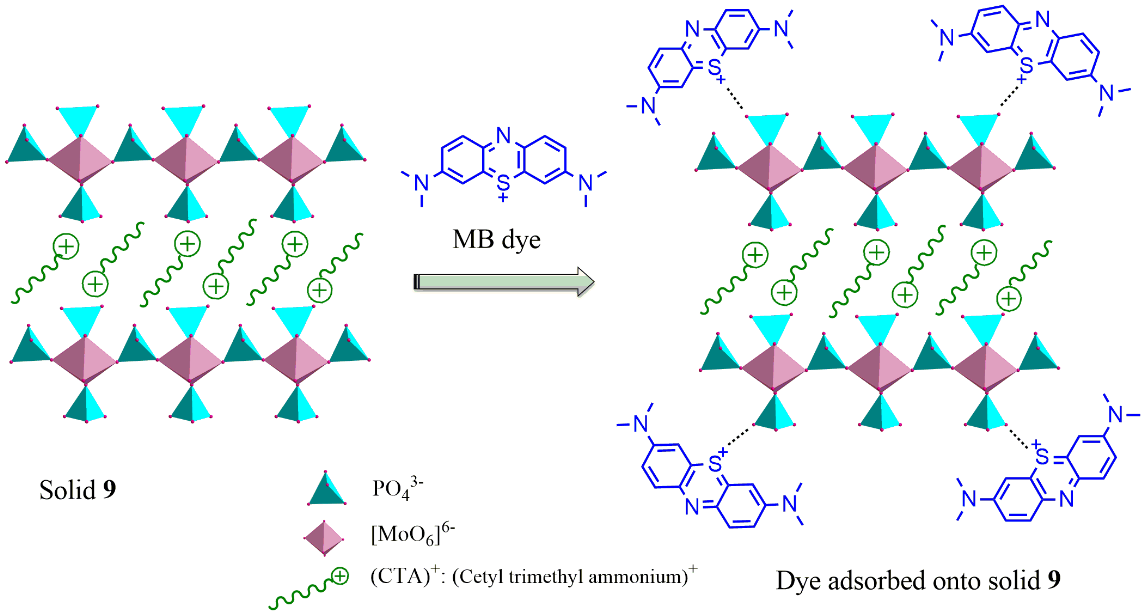

Figure V.15 Adsorption of MB onto the surface of solid **9** via electrostatic attraction.

V.5 Conclusion

Nanostructured phosphomolybdate solid templated by cationic surfactant, CTAB was synthesized under ambient conditions and characterized. The synthesized hybrid was investigated for its efficiency in removing cationic and anionic dyes from aqueous solution. The solid, **9** was found to be effective adsorbent in removing cationic dyes *viz*; methylene blue and malachite green. The maximum removal efficiency of 94.8 % was achieved on treating 25mL of 5ppm MB solution with 0.1g of **9** for 40 minutes. The solid **9** could be reused upto 6 cycles without any loss in adsorption efficiency. The equilibrium adsorption data was best modeled using the Freundlich isotherm and the pseudo second-order kinetic model provided the best correlation for the experimental data. CTAB templated PMO nanoparticles appear to be a promising novel adsorbent for selective removal of cationic dyes in effluent treatment process.

References

1. Parker A (1932) Nature 130:761-763

2. Huang Z, Li Y, Chen W, Shi J, Zhang N, Wang X, Li Z, Gao L, Zhang Y (2017) Mater Chem Phys 202:266-276

3. Malarvizhi R, Ho YS (2010) Desalination 264:97-101

4. Katheresan V, Kansedo J, Lau SY (2016) J Environ Chem Eng 6:4676-4697

5. Tian X, Hou L, Wang J, Xin X, Zhang H, Ma Y, Wang Y, Zhang L, Han Z (2018) Dalton Trans 47:15121-15130

6. Ali I, Peng C, Naz I, Lin D, Saroj D P, Ali M (2019) RSC Adv 9:3625-3646

7. Khan MI, Akhtar S, Zafar S, Shaheen A, Khan MA, Luque R, Rehman A (2015) Materials 8:4147-4161

8. Ahmad A, Setaper SHM, Chuo SC, Khatoon A, Wani WA, Kumar R, Rafatullah M (2015) RSC Adv 5:30801-30818

9. Erdemoglu S, Aksu SK, Sayilkan F, Izgi B, Asilturk M, Sayilkan H, Frimmel F, Gucer S (2008) J Hazard Mater 155:469-476

10. Wang S, Li H, Xu L (2006) J Colloid Interface Sci 295:71-78

11. Liu L, Lin Y, Liu Y, Zhu H, He Q (2013) J Chem Eng Data 58:2248-2253

12. Hameed BH, El-Khaiary MI (2008) J Hazard Mater 154:639-648

13. Kausar A, Iqbal M, Javed A, Aftab K, Nazli Z, Bhatti HN, Noureen S (2018) J Mol Liq 256:395-407

14. Yao L, Lua SK, Zhang L, Wang R, Dong ZL (2014) J. Hazard. Mater 280:428-435

15. Kaur J, Kozhevnikov IV (2004) Catal Commun 5:709-713

16. Li HL, Qi W, Li W, Sun H, Bu WF, Wu LX (2005) Adv Mater 17:2688-2692

17. Wang XL, Wang YH, Hu CW, Wang EB (2002) Mater Lett 56:305-311

18. Kurth DG, Lehmann P, Volkmer D, Coelfen H, Koop MJ, Muller A, Du Chesne A (2000) Chem Eur J 6:385-393

19. Kurth DG, Lehmann P, Volkmer D, Muller A, Schwahn D (2000) J Chem Soc Dalton Trans 21:3989-3998

20. Volkmer D, DuChesne A, Kurth DG, Schnablegger H, Lehmann P, Koop MJ, Muller A (2000) J Am Chem Soc122:1995-1998

21. Wu P, Volkmer D, Bredenkotter B, Kurth DG, Rabe JP (2008) Langmuir 24:2739-2745

22. Thomas J, Kannan KR, Ramanan A (2008) J Chem Sci 120(6):529-536

23. Huo Q, Margolese DI, Ciesla U, Demuth DG, Feng P, Gier TE, Sieger P, Firouzi A, Chmelka, BF, Schüth F, Stucky GD (1994) Chem Mater 6:1176-1191

24. Yamauchi Y, Kuroda K (2008) Chem Asian J 3:664-676

25. Bu W, Li W, Li H, Wu L, Tang AC (2004) J Colloid Interface Sci 274:200-203

26. Tang ZY, Liu SQ, Wang EK, Dong SJ, Wang EB (2000) Langmuir 16:5806-5813

27. Zhang G, Ke H, He T, Xiao D, Chen Z, Yang W, Yao J (2004) J Mater Res 19:496-500

28. Langmuir I (1918) J Am Chem Soc 40(9):1361-1403

29. Freundlich HMF (1906) Z Phys Chem 57A:385-470

30. Lagergren S (1898) K Sven Vetensk Handl 24(4):1-39

31. Ho YS, McKay G (1999) Process Biochem 34(5):451-465

32. Weber WJ, Morris JC (1963) J Sanit Eng Div Am Soc Civil Eng 89:31-60

Chapter VI

Synthesis and characterization of phosphomolybdate-polypyrrole composites

Summary

In this chapter, a novel binary composite of ammonium phosphomolybdate (APM) with a conducting polymer *viz*. Polypyrrole (Ppy), has been synthesized by chemical oxidative polymerization method using ammonium per sulphate (APS) as the oxidant. The formation of APM-Ppy composite was confirmed by FTIR and PXRD. The morphology and composition of the composite was established using FESEM and EDAX. The thermal stability of the composite was investigated using TG analysis. The effect of various parameters such as molar ratio of reactants, stirring time and temperature on the formation of the composite was also studied. Further, the potential of the synthesized composite to be used as an indicator in acid-base titrations was also investigated.

VI.1 Introduction

Composite materials have gained significant attention due to their unique properties and potential for various applications. These materials are composed of two or more different components, which result in the final product having properties that are superior to those of the individual components. Keggin type phosphomolybdates belong to a class of polyoxometalate solids having the general formula $[PMo_{12}O_{40}]^{n-}$ and they possess several unique properties [1-3]. Recently, a few composites of Keggin-type phosphomolybdates (PMOs) have been synthesized, and they seem to have potential uses as sensors, catalysts, and in energy storage applications [4-7]. Such PMOs with its strong oxidizing potential and inherent acidity can also serve as ideal candidates for the formation of polyoxomolybdate-polymer composites with polymers like acrylonitrile, vinyl alcohol, etc. [8-10]. A review of such binary composites of phosphomolybdates with polymers published in the past decade has been summarized in Table VI.1.

Among the various Keggin based polyoxometalates, ammonium phosphomolybdate, $\{NH_4\}_3[PMo_{12}O_{40}].xH_2O$ is a redox active inorganic cluster solid exhibiting wide range of applications such as ion-exchanger, in drug delivery systems, DNA synthesis, dielectric material and memory device fabrication [11-15]. This versatile ammonium phosphomolybdate (APM) solid when embedded into the polymer matrix can often result in improved properties of the composites formed. For example, a composite of APM with polyacrylonitrile was found to be an effective ion-exchange membrane for selective removal of cobalt, strontium and cesium from radioactive laundry waste water as reported by Park *et.al*. [16]. Similarly, conducting polymers such as polypyrrole, polythiophene, polyaniline, etc. can serve as ideal platforms to embed the redox-active PMOs which in turn can produce novel composite materials with interesting properties [17].

Table VI.1 A review of phosphomolybdate-polymer composites reported in the last decade.

S. No.	Keggin type and polymer	Synthetic method	Property/ Application	Ref.
1.	APM - Polyacrylonitrile	Chemical polymerization method using surfactant	Removal of Cs^+ by ion exchange Removal of cobalt, strontium and cesium from nuclear-waste water	[8] [16]
2.	$H_3PMo_{12}O_{40}$ - Poly vinyl alcohol	Layer by layer (LBL) assembly technique	Photochromic property	[10]
3.	$H_3PMo_{12}O_{40}$- Polyaniline	Chemical oxidative polymerization with APS	Electrocatalytic property	[18]
4.	$H_3PMo_{12}O_{40}$ - polyacrylamide	Direct mixing of solutions in deionized water	Photochromic property	[19]
5.	$H_3PMo_{12}O_{40}$- Chitosan	Direct mixing of the reactants with a cross linking agent	Improved mechanical properties	[20]
6.	$H_3PMo_{12}O_{40}$- Chitosan	By sonication method in presence of surfactant	Antimicrobial activity	[21]
7.	$H_3PMo_{12}O_{40}$- Polymethylmathacrylate	Prepared by electrospinning	Photocatalytic property	[22]
8.	$[PMo_{12}O_{40}]^{3-}$- polyamidoamine	LBL assembly method	Electrocatalytic property	[23]
9.	$[PMo_{12}O_{40}]^{3-}$- polypyrrole	Co-electrodeposition using chrono-amperometric technique	Humidity sensing	[24]

Therefore, in this chapter, synthesis of composite of APM with a conducting polymer *viz.* Polypyrrole (Ppy) via chemical oxidative polymerization method using Ammonium persulphate (APS) has been carried out and characterized. Further, the role of reaction parameters on the formation of composite was explored by varying the concentration of the reactants, temperature and stirring time. In addition, the potential of APM-Ppy composite to act as an indicator in acid-base titrations was also studied.

VI.2 Experimental

VI.2.1 Synthesis of APM/Polymer composite

The synthesis of composite based on APM and Ppy was carried out as follows:

To a stirring solution of 20 mL ammonium heptamolybdate, $(NH_4)_6Mo_7O_{24}.4H_2O$ (0.03 M, Merck, 99%) kept in a water bath, 10 mL of disodium hydrogen phosphate dihydrate, $Na_2HPO_4.2H_2O$ (0.2 N, Aldrich, 99%) in 8 mL conc. HNO_3 was added. 0.6 mL of pyrrole was dissolved in 10 mL of distilled water and was added in small aliquots along with 0.5g Ammonium persulphate (APS) simultaneously to the above stirring solution. The contents were stirred for 20 minutes and the resultant black powder was washed with water and filtered. The products thus obtained were dried in oven for 5 hours at 60°C.

The effect of various parameters such as molar ratio of reactants, stirring time, temperature, etc. on the formation of the composite was also investigated.

VI.2.2 Synthesis of APM

Synthesis of APM and Ppy were carried out independently inorder to compare the FTIR and PXRD patterns of composite with that of APM and polymer, thereby it could also confirm the formation of the composite.

APM was synthesized as per the procedure reported in literature by Joseph *et. al.*[12]. A solution containing 11.05 g of $(NH_4)_6Mo_7O_{24}.4H_2O$ with 15 mL of ammonia solution and 10 mL of distilled water was boiled and made upto 250 mL. 100 mL of the above solution was added to 40 mL of 0.067 M solution of $Na_2HPO_4.2H_2O$ and 20 mL of conc. HNO_3 and stirred for 10 minutes. The resultant solution was kept undisturbed for 18 hours. The canary yellow precipitate of APM thus obtained was washed with water, filtered and air dried.

VI.2.3 Synthesis of Polypyrrole

Ppy was synthesized via chemical oxidative polymerization of pyrrole using APS as the oxidant similar to the procedure reported in literature [25]. In a typical synthesis, 1.2 mL of pyrrole was dissolved in 20 mL of distilled water and kept in an ice bath. To the stirring solution, 0.5g APS dissolved in 10mL of distilled water was added and stirred for 4 hours. The black powder of Ppy formed was washed several times with ethanol and water, filtered and dried in oven for 6 hours at 100°C.

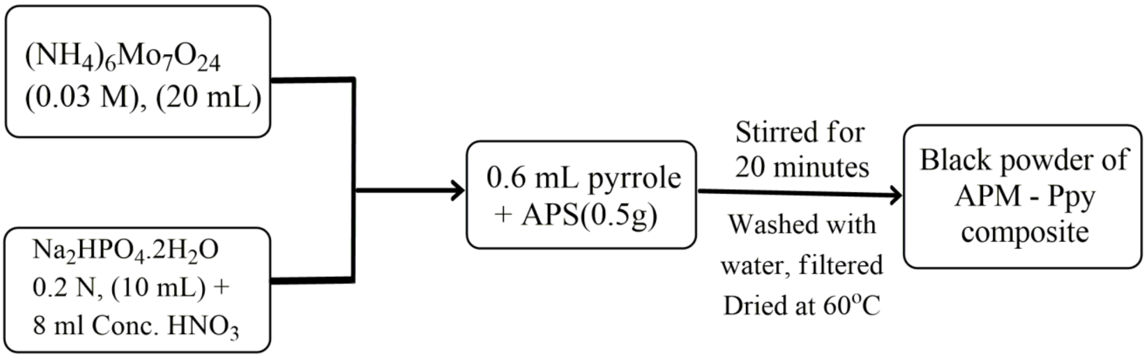

Scheme VI.1 Synthetic procedure for preparing APM-Ppy composite.

VI.3 Characterization

Synthesized APM-Ppy composite was characterized by techniques namely PXRD, FTIR and TGA as discussed under Section II.2.3 in Chapter II. The morphology and composition of the composite was established using FESEM and EDAX as discussed under Section V.2.3 in Chapter V.

VI.4 APM-Ppy composite as acid-base indicator

Conducting polymers such as polyaniline are well-known for their electrical and optical properties that can be varied via protonation or deprotonation of the amine nitrogen atoms. Similarly, Polypyrrole also changes color in acidic and basic solutions due to protonation and deprotonation respectively. Therefore, APM-Ppy composite was tested for its behaviour in various acidic and basic solutions and investigated for its potential to be used as indicator in acid-base titrations.

VI.4.1 Solubility test

0.003g of Ppy and APM-Ppy was weighed separately in five beakers (i)-(v). 20mL of distilled water, HCl (0.1N), Oxalic acid (0.1N), Na_2CO_3 (0.1N) and NaOH (0.1N) solution was added respectively and stirred for 5 minutes. The contents were filtered and color in the beakers (i)-(v) was noted under visible light. Both Ppy and APM-Ppy showed yellow and reddish-brown color in acidic and basic solutions respectively. The change in color from yellow to reddish-brown upon increasing pH from acidic to neutral to basic was evaluated using UV-Vis spectroscopy as well. Therefore, it was tested as acid-base indicators for various titrations.

VI.4.2 Acid-base Indicator test

Preparation of Indicator Solution

Since Ppy and APM-Ppy composite showed color changes in acidic, basic and neutral conditions, its ability to act as acid-base indicators was tested. 0.003 g of Ppy and APM-

Ppy were dissolved separately in 10 mL of DMF. The indicator solutions were shaken well until the entire compound was dissolved completely.

Titrations

The following titrations were performed in the presence of 0.5 mL of the indicator solution at room temperature:

(i) 20 mL 0.1 N of HCl versus 0.1N of NaOH

(ii) 20 mL 0.1 N of Oxalic acid versus 0.1 N of NaOH

(iii) 20 mL 0.1 N of HCl versus 0.1 N of Na_2CO_3

(iv) 20 mL 0.1 N of Oxalic acid versus 0.1 N of Na_2CO_3

In all titrations, 20 mL of base was pipetted into a conical flask and 0.5 mL of indicator solution was added. The solution was titrated against acid till the color changed from reddish-brown to yellow. The titration was repeated to get concordant results. The titrations were also carried out using standard indicators namely phenolphthalein or methyl orange to validate the accuracy of the end point.

VI.5 Results and Discussion

APM-Ppy composite was synthesized via chemical oxidative polymerization method using APS as the oxidant. The formation of the composite was confirmed by comparing the FTIR and PXRD patterns of APM, Polypyrrole and APM-Ppy composite.

VI.5.1 APM-Ppy composite structure and characterization

Figure VI.1a shows the PXRD patterns of APM, Ppy and APM-Ppy composite. The X-ray diffraction pattern of Ppy displayed a broad peak at around 2θ = 25°, which is the characteristic peak of amorphous Ppy [25]. PXRD pattern of APM showed well defined peaks corresponding to its crystalline nature and it matched well with JCPDS file no. 43-0315 indicating the formation of single-phasic cubic $\{NH_4\}_3[PMo_{12}O_{40}].xH_2O$ having lattice constant *a* = 11.67 Å. The PXRD pattern of the APM-Ppy composite exhibits a semi-crystalline behavior with well-defined peaks of APM along with broad peaks of Ppy, thus confirming the formation of APM-Ppy composite.

The FTIR spectrum of APM-Ppy composite showed peaks characteristics of APM and Ppy (Figure VI.1b). The bands in the region 1100-500 cm^{-1} were attributed to the characteristic peaks of Keggin type heteropoly anions [26]. The peaks at 1062, 963 and 880 cm^{-1} were assigned to γ_{as}(P-Oa), γ_{as}(Mo-Od) and γ_{as}(Mo-Ob-Mo) respectively [12]. The peak at 3234 cm^{-1} was assigned to the presence of N-H stretching vibrations of Ppy. The characteristic peaks at 1518 cm^{-1} and 1423 cm^{-1} correspond to the C=C stretching, whereas peaks at 1656 cm^{-1} and 1355.4 cm^{-1} represented C=N and C–N vibrations respectively [27].

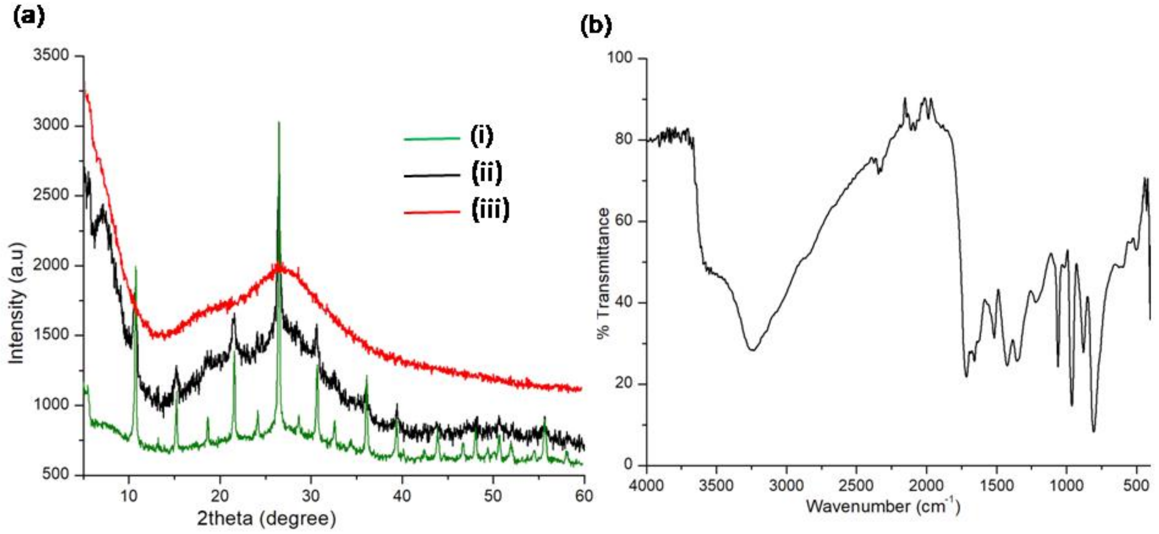

Figure VI.1 (a) PXRD of (i) APM (ii) APM-Ppy (iii) Polypyrrole and (b) FTIR of APM-Ppy composite.

FESEM image of the APM-Ppy composite indicated that the particles are having spherical morphology with particle size ranging from 50-140 nm (Figure VI.2a). EDAX spectrum showed the peaks of carbon, nitrogen, phosphorous, molybdenum and oxygen at 0.277(Ka1), 0.392(Ka1), 2.014(Ka1), 2.418(Lβ2) and 0.525(Ka1) respectively (Figure VI.2b). Scheme VI.2 shows the formation of APM-Ppy composite.

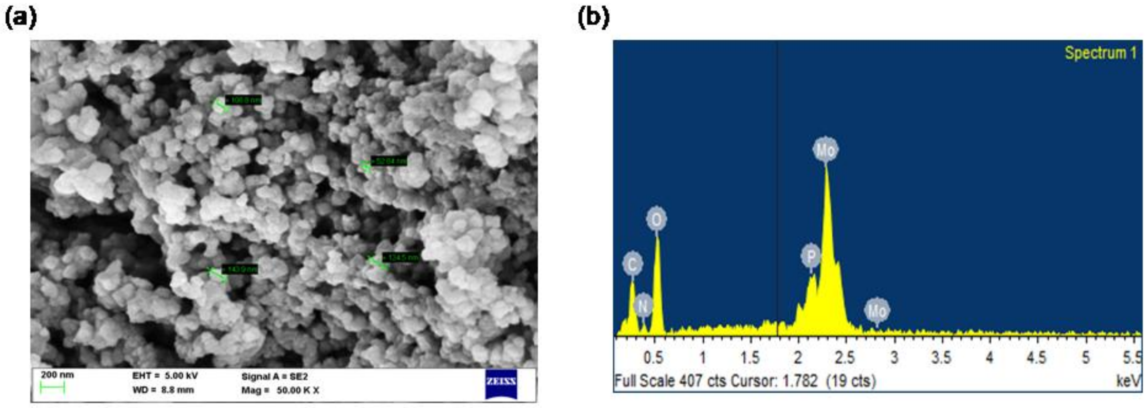

Figure VI.2 (a) FESEM image and (b) EDAX of APM-Ppy composite.

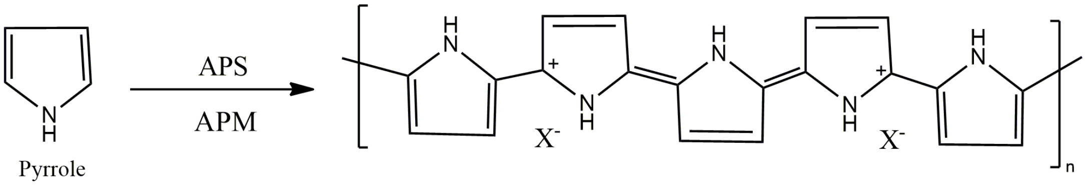

APS = $(NH_4)_2S_2O_8$

APM = $(NH_4)_3PMo_{12}O_{40}$

X = $\{PMo_{12}O_{40}\}$

APM-Ppy composite

Scheme VI.2 Formation of APM-Ppy composite via oxidative polymerization.

VI.5.2 Thermal analysis

The thermal stability of the synthesized composite was studied using thermogravimetric analysis in the temperature range from RT to 800°C. Figure VI.3 shows the TG curve of APM-Ppy composite. The weight loss occurred in three steps corresponding to loss of water molecules, Ppy moieties and finally formation of residual MoO_3 with simultaneous release of P_2O_5.

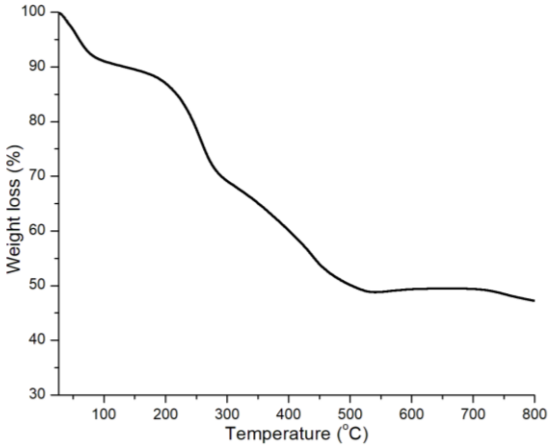

Figure VI.3 TG plot of APM-Ppy composite.

VI.5.3 Influence of reaction parameters on the formation of composite

The composition and morphology of composite materials are greatly influenced by reaction conditions such as molar ratio of the reactants, temperature, pH and stirring time. Therefore, the influence of reaction parameters viz. concentration of Ppy, stirring time and temperature on the formation of composite was studied.

VI.5.3.1 Effect of concentration of pyrrole

Different concentrations of pyrrole were used for preparing the APM-Ppy composite, keeping the concentrations of other reactants constant as per the procedure discussed under Section VI.2.1. It was observed that at lower concentrations of pyrrole (0.2 mL and 0.3 mL), phosphomolybdate solids were formed as indicated by the PXRD patterns in Figure VI.4. When the concentration was increased to (0.6 mL), APM-Ppy composite was formed. However, upon further increasing the concentration to 1.2 mL, pure Ppy was obtained which was confirmed from the PXRD pattern shown in Figure VI.4.

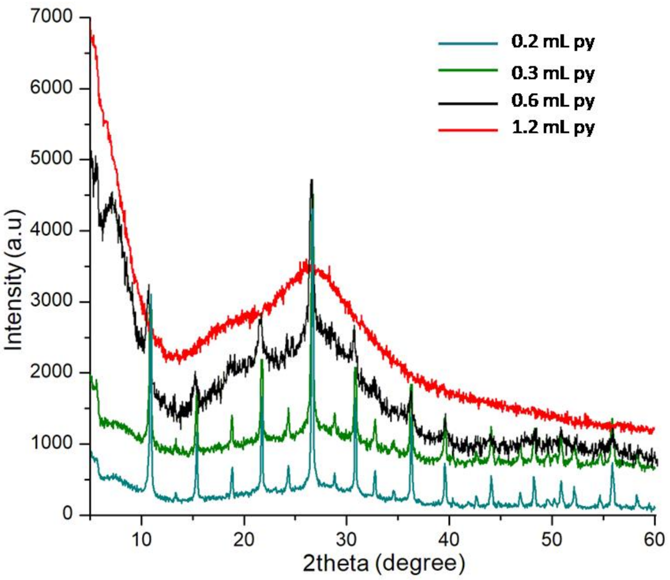

Figure VI.4 PXRD patterns of solids obtained at various concentrations of pyrrole.

VI.5.3.2 Effect of stirring time

The influence of stirring time on composite formation was also studied. At stirring times of 5 minutes and 10 minutes, APM was formed. The composite formation began on increasing the stirring time to 15 minutes and the optimum time required for forming APM-Ppy composite was found to be 20 minutes which was confirmed from the PXRD and FTIR spectra as shown in Figure VI.5

VI.5.3.3 Effect of temperature

Polymerization of pyrrole is usually carried out at lower temperatures as reported in literature [25]. Hence, during the synthesis of composite, the reactant mixture was kept in an ice bath for effective polymerization and formation of APM-Ppy composite. The synthesis was repeated at varying temperatures for studying the effect of temperature on the formation of composite. It was observed that composite formation easily took place at temperatures ranging from room temperature (RT) to as low as 3°C as indicated by Figure VI.6

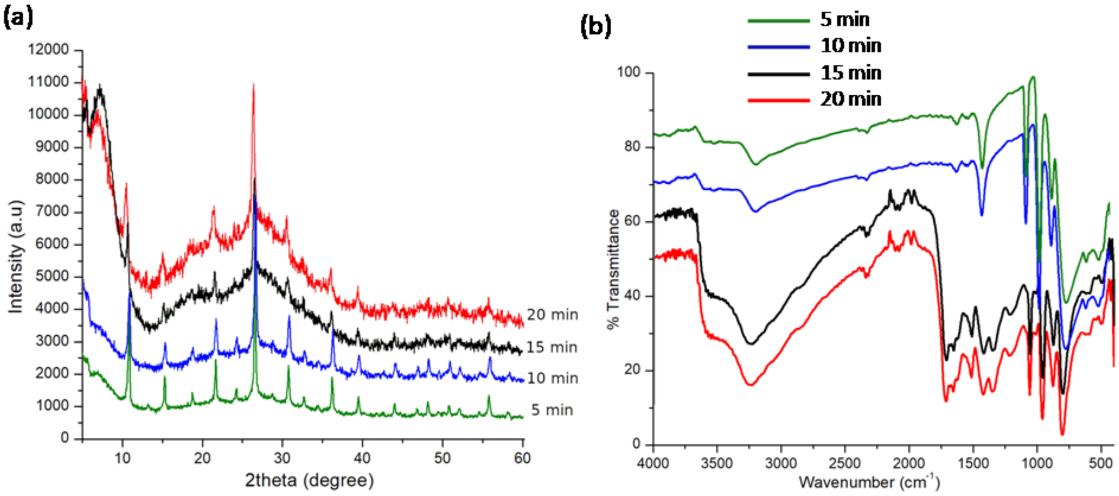

Figure VI.5 (a) PXRD and (b) FTIR patterns of solids obtained at different stirring time.

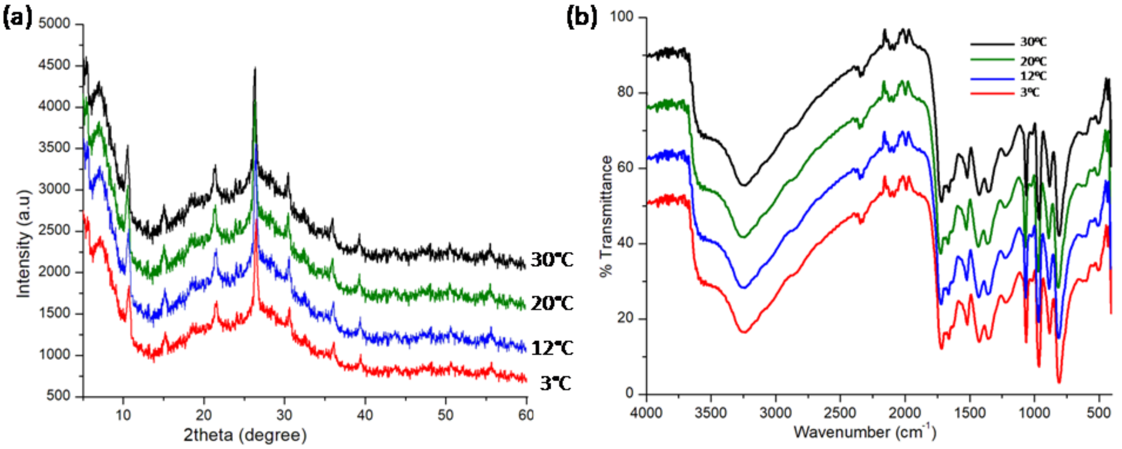

Figure VI.6 (a) PXRD and (b) FTIR patterns of solids obtained at different temperatures.

VI.5.4 Solubility test and color

The solubility of Ppy and APM-Ppy composite was tested in various solutions such as distilled water, 0.1N HCl, 0.1N oxalic acid, 0.1N NaOH and 0.1N Na_2CO_3. It was observed that Ppy was insoluble in water and acidic solutions but soluble in NaOH and Na_2CO_3. It displayed yellow color in neutral and acidic solutions whereas the color changed to reddish-brown in basic solutions (Figure VI.7a). A similar color variation was also displayed by APM-Ppy composite (Figure VI.7b), but the solubility of the composite in the solutions was more when compared to the polymer.

Table VI.2 Table summarizing results obtained from solubility test and color displayed by Ppy and APM-Ppy in various acid-base solutions.

Ppy	**Water**	**HCl**	**Oxalic acid**	**NaOH**	**Na_2CO_3**
Solubility	Insoluble	Insoluble	Insoluble	Soluble	Soluble
Color	Yellow	Yellow	Yellow	Reddish-brown	Reddish-brown
APM-Ppy					
Solubility	Partially soluble	Partially soluble	Partially soluble	Soluble	Soluble
Color	Yellow	Yellow	Yellow	Reddish-brown	Reddish-brown

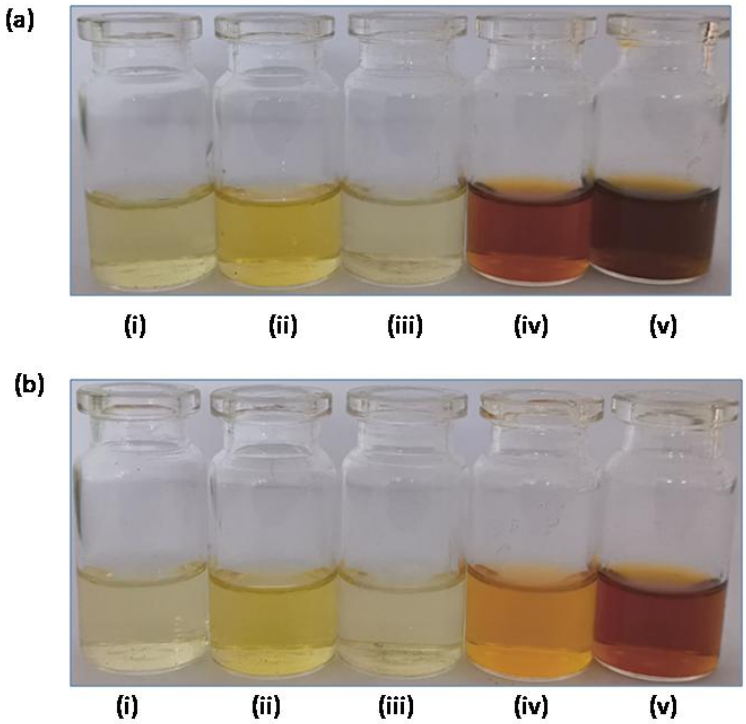

Figure VI.7 Color displayed by (a) Ppy and (b) APM-Ppy in (i) distilled water, (ii) HCl (0.1 N), (iii) Oxalic acid (0.1 N), (iv) Na_2CO_3 (0.1 N) and (v) NaOH (0.1 N).

VI.5.5 Acid-base Indicator test

Ppy and APM-Ppy composite had a stable color in acid, base and neutral solutions and showed reversible and sharp color changes when moving from acidic condition to the basic condition or vice versa. Hence, end point could be determined with high precision using both Ppy and APM-Ppy composite. The following tables include titration data of acid-base reactions that were used to evaluate the indicator property of Ppy and APM-Ppy. Figure VI.8 and VI.9 show the colors of solutions in acid and base conditions using Ppy and APM-Ppy indicator solutions respectively.

Titration I: 20 mL 0.1 N of HCl versus 0.1 N of NaOH

Indicator used	Volume of NaOH (mL)	Color in acid	Color in base
Phenolphthalein	19.4	Colorless	Pink
PPy	19.2	Yellow	Reddish-brown
APM-Ppy	19.1	Yellow	Reddish-brown

Titration II: 20 mL 0.1 N of Oxalic acid versus 0.1 N of NaOH

Indicator used	Volume of NaOH (mL)	Color in acid	Color in base
Phenolphthalein	19.8	Colorless	Pink
PPy	19.7	Yellow	Redddish-brown
APM-Ppy	19.7	Yellow	Redddish-brown

Titration III: 20 mL 0.1 N of HCl versus 0.1 N of Na_2CO_3

Indicator used	Volume of Na_2CO_3 (mL)	Color in acid	Color in base
Methyl orange	18.4	red	Yellow
PPy	18.2	Yellow	Redddish-brown
APM-PPy	18.1	Yellow	Redddish-brown

Titration IV: 20 mL 0.1 N of Oxalic acid versus 0.1 N of Na_2CO_3

Indicator used	Volume of Na_2CO_3 (mL)	Color in acid	Color in base
PPy	20.5	Yellow	Redddish-brown
APM-PPy	20.4	Yellow	Redddish-brown

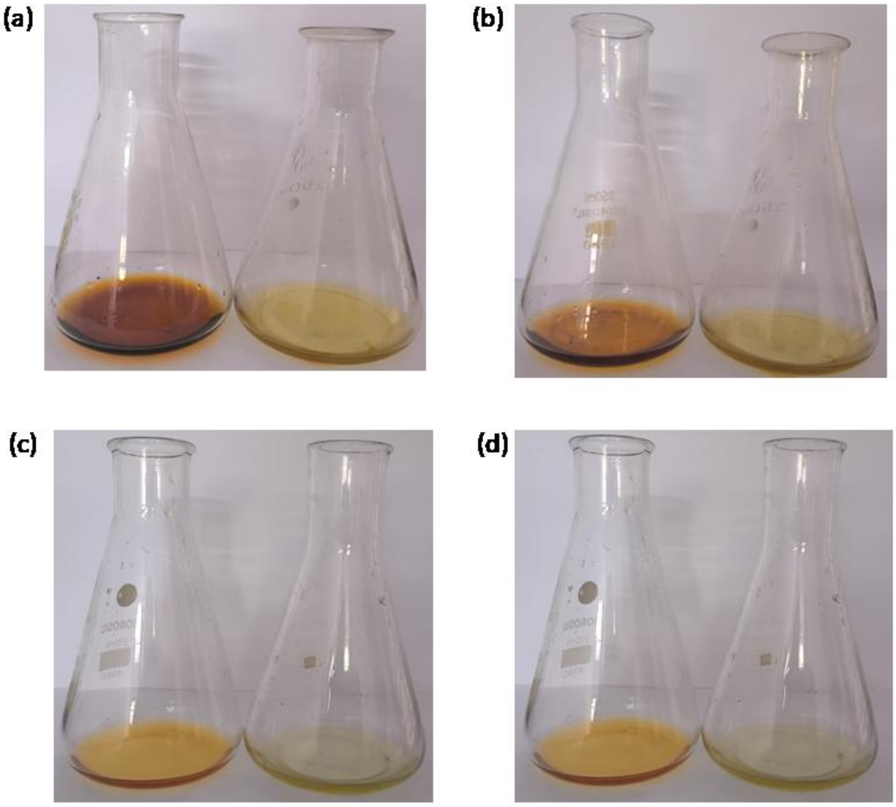

Figure VI.8 Colors of solution before and after end point in using Ppy indicator solution in (a) HCl versus NaOH (b) Oxalic acid versus NaOH (c) HCl versus Na_2CO_3 (d) Oxalic acid versus Na_2CO_3 titration.

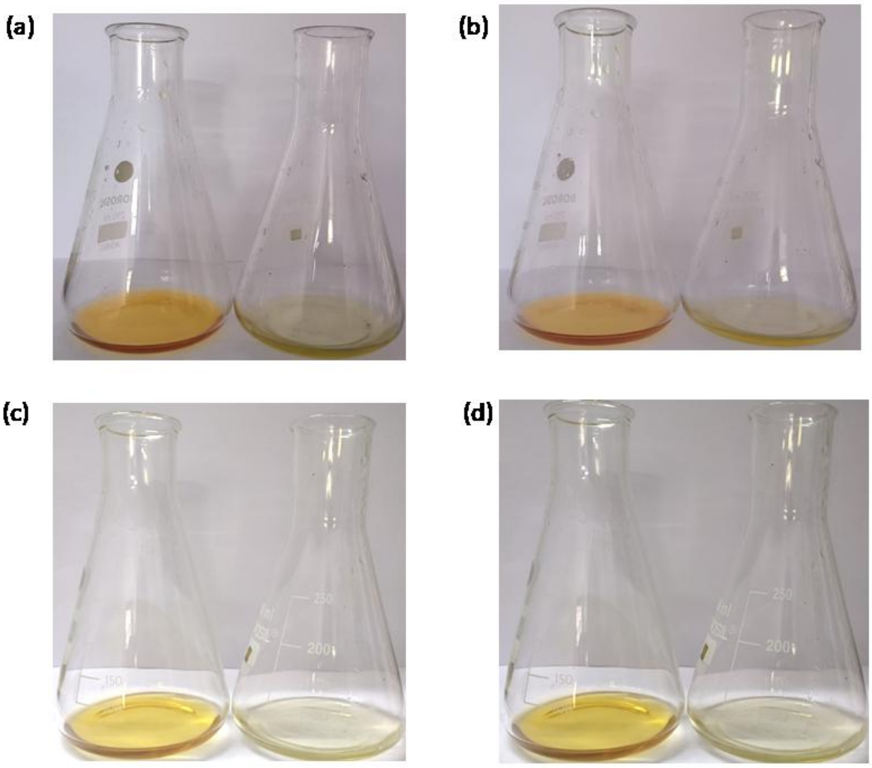

Figure VI.9 Colors of solution before and after end point in using APM-Ppy indicator solution in (a) HCl versus NaOH (b) Oxalic acid versus NaOH (c) HCl versus Na_2CO_3 (d) Oxalic acid versus Na_2CO_3 titration.

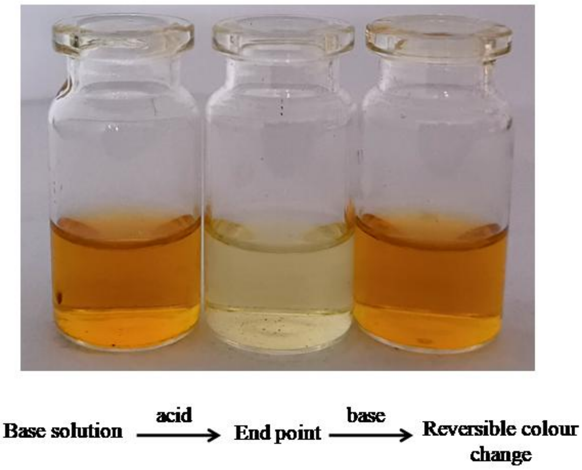

Figure VI.10 Reversible color change of solution indicating the utility of APM-Ppy indicator solution for double burette titration as well.

The change in color from yellow to reddish-brown upon increasing pH from acidic to neutral to basic was evaluated using UV-Vis spectroscopy as well for APM-Ppy composite. A shift in λ_{max} was observed upon change in pH as shown in Figure VI.11. The absorption peak of APM-Ppy composite showed a red shift in basic solutions due to the deprotonation of the pyrrole units. At lower pH solutions pyrrole moieties become protonated which causes a blue shift in the UV-visible spectra.

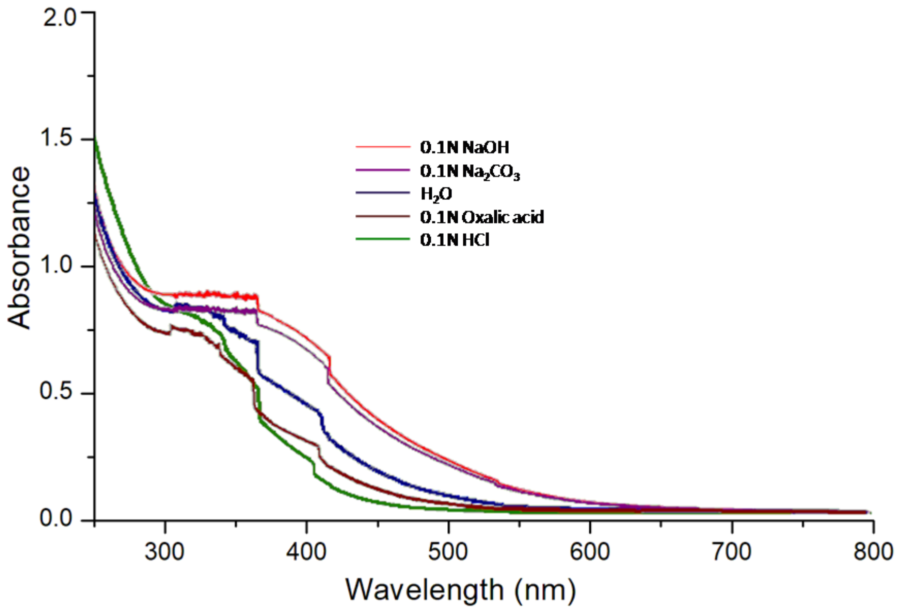

Figure VI.11 UV-visible spectra of APM-Ppy composite in acidic, neutral and basic solutions.

Table VI.3 λ_{max}values with varying pH.

Solution	pH	APM-Ppy,λ_{max}(nm)
Distilled water	7.0	412
0.1 N of HCl	1.5	409
0.1 N of Oxalic acid	3.1	410
0.1 N of NaOH	10.2	418
0.1 N of Na_2CO_3	8.3	417

From the above results it can be observed that the APM-Ppy composite retains the acid-base properties of Polypyrrole. Moreover, the composite is soluble in all solvents when compared to Polypyrrole and APM. This makes it an excellent medium as an indicator in acid-base titrations and also as a pH sensor.

VI.6 Conclusions

A novel composite of APM-Ppy was synthesized by chemical oxidative polymerization method using APS and characterized using FTIR, PXRD, FESEM and EDAX. The thermal stability of the composite was studied by thermogravimetric analysis. The influence of reaction parameters such as concentration of pyrrole, stirring time and temperature on composite formation was investigated. It was found that composite could be easily synthesized at temperatures ranging from RT to as low as 3°C, with 0.6mL pyrrole and 20 minutes stirring time. APM-Ppy composite was also found to be an excellent acid-base indicator in various titrations and can be used as a pH sensor.

References

1. Dias JA, Dias SCL, Caliman E, Bartis J, Francesconi L (2014) In: Girolami GS, Sattelberger AP (eds) Keggin Structure Polyoxometalates. Inorganic Syntheses: Volume 36, John Wiley & Sons, Inc
2. Xie F, Ren J, Liu W, Wang T, Yuan J, Jiang X, Zhang H (2018) J Clust Sci 29:1227-1232
3. Pathan S, Patel A (2014) Catal Sci Technol 4:648-656
4. Ghali M, Brahmi C, Benltifa M, Vaulot C, Airoudj A, Fioux P, Dumur F, Jégat SC, Savary MF, Jellali S, Bousselmi L, Lalevée J (2021) J Polym Sci 59:153-169
5. Xu J, Cao X, Xia J, Gong S, Wang Z, Lu L (2016) Anal Chim Acta 934:44-51
6. Lu L, Xie Y (2017) New J Chem 41:335-346
7. Song YF, Tsunashima R (2012) Chem Soc Rev 41:7384-7402
8. Ding D, Zhang Z, Chen R, Cai T (2016) J Hazard Mater 324:753-761
9. Park Y, Lee YC, Shin WS, Choi SJ (2010) Chem Eng J 162:685-695
10. Li ZJ, Zhao WJ, Shi Y, Ying ZP, Feng W, Bai L (2018) Compos Interfaces 25:809-821
11. Sinha AK, Sasmal AK, Pal A, Pal D, Pal T (2021) J Photochem Photobiol A: Chem 418:113427
12. Joseph J, Radhakrishnan RC, Johnson JK, Joy SP, Thomas J (2020) Mater Chem Phys 242:122488
13. Rhule JT, Hill CL, Judd DA, Schinazi RF (1998) Chem Rev 98:327-358
14. Muller WEG, Schroder HC, Wang X (2019) Chem Rev 119:12337-12374
15. Ghosh SK, Perla VK, Mallick K, Pal T (2020) Nanoscale Adv 2:5343-5351
16. Park Y, Lee YC, Shin WS, Choi SJ (2010) Chem Eng J 162:685-695
17. Herrmann S, Ritchie C, Streb C (2015) Dalton Trans 44:7092-7104

18. Papagianni GG, Stergiou DV, Armatas GS, Kanatzidis MG, Prodromidis MI (2012) Sens Actuators B 173:346-353
19. Chen J, Dong LL, Feng W, Liu SL, Liu J, Yang FL (2013) J Mol Struct 1049:414-418
20. Bhat AH, Bhat IUH, Khalil HPSA (2010) J Compos Mater 45:39-49
21. Matteis LD, Mitchell SG, Fuente JM (2014) J Mater Chem B2:7114-7117
22. Zhang ZM, Li TT, Liu C (2013) Appl Mech Mater 395:415-418
23. Li ZS, Lin S, Chen ZL, Shi YD, Huang XM (2012) J Colloid Interface Sci 368:413-419
24. Miao J, Chen Y, Li Y, Cheng J, Wu Q, Wei K, Cheng X, Chen R, Cheng C, Tang Z (2018) ACS Appl Nano Mater 1(2):564-571
25. Chaluvaraju BV, Sangappa KG, Murugendrappa MV (2015) Polym Sci A 57(4):467-472
26. Qi M, Yu K, Su Z, Wang C, Wang C, Zhou B, Zhu C (2013) Inorg Chim Acta 400:59-66
27. Tian B, Zerbi G (2009) J Chem Phys 92(6):3886-3891

Chapter VII

Summary and Conclusions

This thesis describes the synthesis and characterization of various organic-inorganic hybrid solids of polyoxometalates and transition metal complexes, based on Cobalt, Copper and Molybdenum and investigation of its properties. A brief summary of the work discussed in previous chapters and the general conclusions drawn from the research are outlined in this chapter.

Chapter I provides a brief review on organic-inorganic hybrid solids; its historical perspective and development. A detailed discussion on the structure, properties and applications of POM cluster based hybrids (Class A) and transition metal based hybrids (Class B) were presented. Various synthetic methods used for the preparation of hybrid solids were also discussed. Finally, the motivation for the present work was briefly outlined.

Chapter II describes the self-assembly of Anderson-Evans type POM cluster based hybrid solids, prepared via solvent evaporation method and pyrazole as the organic precursor. The synthesized solids were characterized by SCXRD, PXRD, FTIR and TGA. The synthesized Anderson clusters were found to be promising candidates for effective polymerization of pyrrole and for preparing polymer based composite materials.

One of the objectives of the work was to explore the nature of reaction conditions such as temperature, pH, nature of reacting molecular units and effect of solvent in the formation of various hybrid solids which in turn can affect the final properties. Hence, in *Chapter III*, an attempt was made to synthesize POM cluster hybrids with 2-aminopyrazine as the organic precursor. However, it resulted in the formation of a new complex of cobalt namely, $[Co(2\text{-H}\mathit{ampz})_2Cl_4]$ which was a pseudopolymorph of $[Co(2\text{-}\mathit{ampz})_4Cl_2]$. The synthesized Co(II) complexes were screened for their antibacterial activity against various bacterial strains. Molecular docking studies were also carried out using DNA gyrase as the protein target. The *in vitro* and *in silico* studies indicated that the complexes can cat as novel antimicrobial agents.

Chapter IV investigates the phenomenon of chromotropism in aminopyridine based tetrachlorocuprates, particularly, solvatochromism, vapochromism and thermochromism. Tetrachlorocuprate(II) anions stabilized by protonated aminopyridines was found to be a significant class of chromogenic materials which may find application as sensors and detectors.

Chapter V describes the synthesis and characterization of surfactant (CTAB) templated phosphomolybdate solid. The hybrid was investigated for its potential in removing cationic and anionic dyes from aqueous solutions and was found to be an effective adsorbent for removing cationic dyes. It could also be reused upto 6 cycles without any loss in its adsorption efficiency and hence it can serve as a novel adsorbent for selective removal of cationic dyes in effluent treatment process.

Chapter VI explores the synthesis and characterization of a novel composite based on ammonium phosphomolybdate and Polypyrrole. It was found that the new composite displayed interesting color variations in acidic, basic and neutral solutions and hence, can be used as a pH sensor and as an end point indicator in different acid-base titrations.

Chapter VIII

Recommendations for future works

"*Our imagination is the only limit to what we can hope to have in the future*."

\- *Charles F. Kettering*

This thesis has been mainly focused on the synthesis, characterization and properties of different types of organic-inorganic hybrid solids based on cobalt, copper and molybdenum. The work presented in this thesis opens up several new opportunities. A few of them are listed below.

- Most hybrid solids in this work were synthesized by solvent evaporation method at ambient conditions which was more time consuming. However, various other methods like hydrothermal, layer diffusion, sonication method, etc. can also be tried for the self-assembly of hybrid solids which may result in new materials with improved properties.
- In Chapter II it was found that Anderson-Evans type POM solids can be used for preparing pyrrole polymer composite materials. In continuation of this work, a different molybdenum source, APM was also tried for preparing polymer composites in chapter VI which showed potential as acid-base indicator to be used in titrations. There is more scope for further investigation of other properties and applications such as sensing of metal ions and biomolecules of such novel composites. Several POM hybrids are reported to be excellent photocatalysts in various reactions. Hence, the synthesized POM cluster hybrids and composites can also be explored for its photocatalytic activity.
- Research on hybrid compounds belonging to the class of transition metal complexes is extensive. In Chapter III, Co(II) complexes with 2-aminopyrazine were screened for its antibacterial activity, whereas in Chapter IV, Cu(II) complexes with isomeric aminopyridines were explored for the chromotropic

phenomena. Further studies (*in vitro* and *in vivo*) can be done to investigate the potential of the above metal complexes as antioxidant, antiviral and anticancer drugs. In addition, aminopyrazines and aminopyridines can also be combined with other transition metal ions to form new complexes with novel properties.

- In chapter V, CTAB templated PMO hybrids were found to be effective adsorbent for removing cationic dyes from aqueous solution. Such surfactant templated nanostructures provide scope for investigating other applications such as catalytic and chromogenic materials and also in biomedical field.

List of Publications

1. **Memsy C K**, Jisha Joseph, Glinta M J & Jency Thomas; Self-assembly of Hybrid Solids $\{Hpz\}_2[H_7CrMo_6O_{24}]\cdot 6H_2O$ and $[Co(2\text{-}Hampz)_2Cl_4]$ (*pz* = pyrazole, 2-*ampz* = 2-aminopyrazine) from Aqueous Solution. *Journal of Chemical Crystallography* (1st October, 2022). https://doi.org/10.1007/s10870-022-00964-y

List of Conference Presentations

1. *Investigation of chromptropism in aminopyridine based copper tetrahalides*- National Seminar on Recent Trends in Materials Science (NSRTMS – 2019), held on 5th & 6th December 2019, at Govt. College, Chittur, Palakkad.
2. *Influence of ligands and anion concentration on crystal engineering of Cobalt (II) based hybrid solids*- International Conference on Chemistry & Physics of Materials ICCPM December 2018, held at St. Thomas' College, Thrissur.

Awards

1. Best Poster Presentation Award in National Seminar on Recent Trends in Material Science (NSRTMS – 2019), held on 5th & 6th December 2019, at Govt. College, Chittur, Palakkad.